A Comparison of Imaging Methods using GPR for Landmine Detection

and

A Preliminary Investigation into the SEM for Identification of Buried Objects

A Thesis Presented

To the Faculty of Graduate Studies

By

Colin Gerald Gilmore

In Partial Fulfillment

of the Requirements for the Degree of

Masters of Science in Electrical Engineering

University of Manitoba

Winnipeg, Manitoba, Canada

December 2004

Abstract

Part I

Various image reconstruction algorithms used for subsurface targets are reviewed. It is shown how some approximate wavefield inversion techniques: Stripmap Synthetic Aperture Radar (SAR), Kirchhoff Migration (KM) and Frequency-Wavenumber (FK) migration are developed from various models for wavefield scattering. The similarities of these techniques are delineated both from a theoretical and practical perspective and it is shown that Stripmap SAR is, computationally, almost identical to FK migration. A plane wave interpretation of both Stripmap SAR and FK migration is used to show why they are so similar. The electromagnetic assumptions made in the image reconstruction algorithms are highlighted. In addition, it is shown that, theoretically, FK and KM are identical. Image reconstruction results for KM, Stripmap SAR and FK are shown for both synthetic and experimental Ground Penetrating Radar (GPR) data. Subjectively the reconstructed images show little difference, but computationally, Stripmap SAR (and therefore, FK migration) are much more efficient.

Part II

A preliminary investigation into the use of the Singularity Expansion Method (SEM) for use in identifying landmines is completed using a Finite-Difference Time-Domain code to simulate a simplified GPR system. The Total Least Squares Matrix Pencil Method (TLS-MPM) is used to determine the complex poles from an arbitrary late-time signal. Both dielectric and metallic targets buried in lossless and lossy half-spaces are considered. Complex poles (resonances) of targets change significantly when the objects are buried in an external medium, and perturbation formulae for Perfect Electric Conductor (PEC) and dielectric targets are highlighted and used. These perturbation formulae are developed for homogenous surrounding media, and their utilization for the half-space

(layered medium) GPR problem causes inaccuracies in their predictions. The results show that the decay rate (real part) of the complex poles is not suitable for identification in this problem, but that with further research, the resonant frequency (imaginary part) of the complex poles shows promise as an identification feature.

Keywords: GPR, Seismic Migration, Stripmap SAR, Landmines, Target Identification, SEM

Contributions

Part I

The main contribution of Part I is to show why Stripmap SAR and Frequency Wavenumber migration are computationally almost identical. Key to the comparison of both techniques is a plane wave interpretation of both. To the authors knowledge, an electromagnetics based plane wave interpretation for Stripmap SAR has not been completed previously. In addition, it is not well understood in the radar community that Kirchhoff Migration and FK migration are equivalent from a theoretical perspective, and this is also shown.

Part II

The contribution of Part II lies in the application of the perturbation formulae developed by Baum [30] and Hanson [32] for PEC and dielectric targets, respectively. The PEC formula has been used previously for UXO targets, but not for landmine targets. No published attempt of the use of the dielectric perturbation formula has been seen by the author.

Acknowledgements

The author would like to thank his research advisor Dr. Joe LoVetri for his encouragement, support, guidance, and extra effort in the preparation of this manuscript. This project would not have been possible without his continuous support.

Thanks to Ian Jeffrey and Hong Su for help in the implementation of the Stripmap SAR algorithm. Many thanks to Eduardo Corral and Daniel Flores for their aid in developing the experimental GPR system, and thanks to Michael Phelan for developing the sandbox testing environment.

Acronyms

BOR -Body of Revolution
CNR -Complex Natural Resonance
DFT -Discrete Fourier Transform
DIFT Discrete Inverse Fourier Transform
EM - Electromagnetics
FDTD - Finite Difference Time Domain
FFT - Fast Fourier Transform
FK - Frequency-Wavenumber ($\omega - k$)
FT - Fourier Transform
GPIB - General Purpose Instrumentation Bus
GPR - Ground Penetrating Radar
HS - Hyperbolic Summation
IFT - Inverse Fourier Transform
KM - Kirchhoff Migration
MPM - Matrix Pencil Method
PEC - Perfect Electric Conductor
SAR - Synthetic Aperture Radar
SEM - Singularity Expansion Method
SVD - Singular Value Decomposition
TLS - Total Least Squares
UN - United Nations
VNA - Vector Network Analyzer

Table of Contents

List of Figures

List of Tables

Chapter 1

Introduction and Motivation

In this chapter, the landmine problem is introduced, as are basic Ground Penetrating Radar (GPR) and inverse imaging concepts. The basic concept of synthetic aperture radar/ migration is introduced, as is the singularity expansion method.

1.1 Problem Discussion

The United Nations (UN) estimates that there are around 110 million buried landmines throughout the world. These cause the deaths of approximately 15,000 to 20,000 people each year. Most (80%) of these deaths are civilians. As they provide a cheap and effective tool of war, their use is extremely widespread: casualties were reported in 65 countries in 2002. [1]

The 'Ottawa Treaty', which banned the use, distribution and manufacture of landmines was signed by 122 countries in 1997, and has been ratified by over 40. However, the clearing of past landmines is still a large humanitarian issue, and the number of landmines cleared each year is outnumbered by the number of new landmines laid by a factor of 20 to 1 [1]. While the best way to deal with the global landmine problem is clearly to continue the efforts of the Ottawa Treaty and stop their use, the clearance of previously laid landmines remains a serious humanitarian issue.

In order to deem land as 'usable', 99.6% of landmines buried up to 10 cm deep must be removed. Current landmine systems, which include prodding, metal detection, and sniffer dogs are slow and dangerous. In the late 1990's there was a large amount of research that went into landmine detection and removal programs utilizing Ground Penetrating Radar (GPR). While many papers have been written (see, for example, the semi-

annual GPR conference [2]), no fast, easy-to-use and safe system has been developed. The purpose of this thesis is to advance the currently developed signal processing (imaging, detection and identification) methods to better the detection and removal of landmines.

1.2 The Inverse Problem in Electromagnetics

The two methods explored in this thesis are that of focusing images generated by GPR, termed migration of images, and that of applying the Singularity Expansion Method for target identification. Both of these methods are a subset of the GPR problem, and the GPR problem is a subset of what is known as the inverse problem.

We can contrast the inverse problem with the forward problem. The general physical

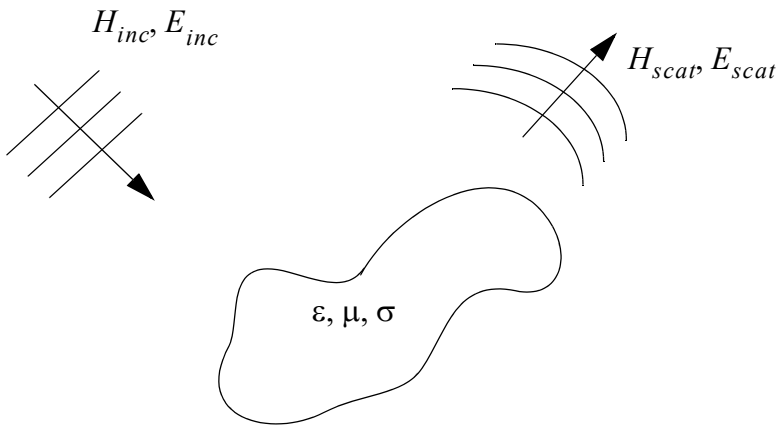

Figure 1.1: The Forward and Inverse Problem in Electromagnetics

set-up of an electromagnetic scattering problem is shown in Figure 1.1. In the forward problem, the incident field, H_{inc}, E_{inc} and the material parameters ε, μ, σ, are known and the scattered field is to be determined. In the inverse problem, we have knowledge of the incident field, H_{inc}, E_{inc} and some (always limited) knowledge of the scattered field, H_{scat}, E_{scat}, and we desire to infer some knowledge of the material parameters, ε, μ, σ. The uniqueness theorem (see Harrington [3]), tells us that, in the forward problem, the

scattered fields, H_{scat}, E_{scat}, are unique. However, the inverse problem is much more complicated. The general inverse problem is an extremely interesting and complex problem; as W.C. Chew [4] states: "The ability to infer information on an object without direct contact also expands man's sensory horizon. No doubt, it is a much sought after capability".

Two important questions for mathematicians concerning a problem are: 1) is there a solution and 2) if there is, is it unique? In inverse imaging, we are also concerned with the question 3) if there is a solution, is it stable? We define stable to mean that an arbitrarily small change in the input (measured scattered fields) will not cause an arbitrarily large change in the solution (material parameters). In GPR we have certainty that a solution exists because some physical media gave rise to the observed scattered fields. The inverse problem, with knowledge of the scattered fields at all points over all frequencies ($0 < \omega < \infty$), outside the object of interest, is unique for two dimensions [5]. This author has not seen a proof of uniqueness for three dimensions. The mathematical proof of the uniqueness has been claimed to be one of the greatest accomplishments of 20th century mathematics.[7]

However, in all practical situations, we deal with non-unique solutions because we cannot practically receive all frequencies at all points in space outside the object of interest. In addition, the problem can be shown to be unstable: an arbitrarily small change in the input can cause an arbitrarily large perturbation of the solution. Problems that are unstable and non-unique are called ill-posed problems [5].

Due to the ill-posed nature of the inverse problem, solution techniques often have to make simplifications and assumptions in order to be feasible. Typically, this means making assumptions about the material parameters beforehand. This can be an acceptable process, for example in GPR we often know or can find many parameters of the soil surrounding possible targets.

The GPR problem is a special case of the generalized inverse problem. Both parts of this thesis, the Synthetic Aperture Radar (SAR)/Seismic Migration section and the Singularity Expansion Method (SEM) section can be viewed as subsets of the inverse problem. The SAR/Migration algorithms fall under what can be termed inverse imaging. Inverse

imaging involves building some type of image of the target, while the general inverse problem may not (such as the utilization of the SEM).

1.3 Basic GPR Principles

The basic process of GPR is depicted in Figure 1.2. The GPR can either be bistatic, with both a transmit and receive antenna, or monostatic with a single transmit and receive antenna. The basic idea is to excite the ground and possible targets with electromagnetic energy, then attempt to infer properties of the ground and targets from scattering information obtained from the experiment.

One of the biggest problems in GPR is the large ground reflection that occurs. With

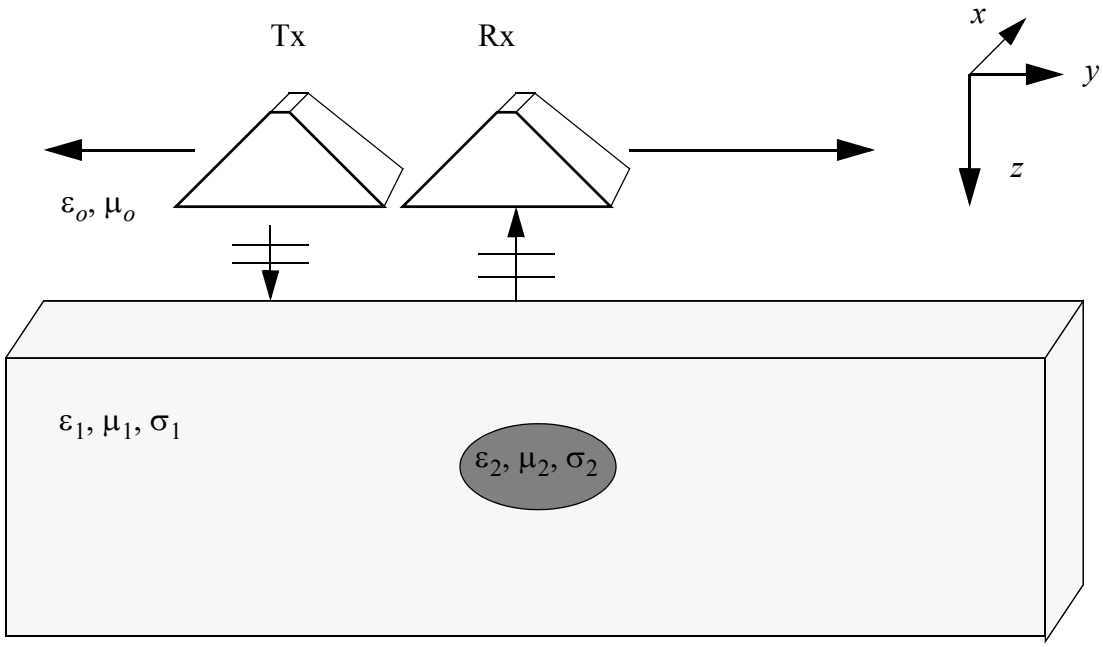

Figure 1.2: The Basic GPR System

a high dielectric contrast between the ground and air, this allows for a very small percentage of the transmitted energy pass the interface, reflect off the target, and pass the interface again to reach the receiving antenna.

In the GPR problem considered here, the antennas operate in free space, while the ground material properties are given by ε_1, μ_1 and σ_1, and the target's properties are

given by ε_2, μ_2 and σ_2. Typically, the antenna(s) are moved over the target in a straight line, which allows for some type of synthetic aperture processing.

1.4 Thesis Overview

Part I of this thesis is concerned with the investigation of image focusing techniques for use with GPR for landmine detection. Following this introduction, Chapter 2 introduces some electromagnetic concepts as well as some Fourier transform fundamentals. Chapter 3 describes Stripmap Synthetic Aperture Radar (SAR), which is followed by Chapter 4, a discussion of Seismic Migration techniques. Chapter 5 provides and discusses experimental and synthetic data as well as discussing theoretical comparisons of Stripmap SAR and the Seismic migration techniques. The work of part one is summarized in Gilmore, et. al. [8].

Part two of this thesis outlines a preliminary investigation of the use of the Singularity Expansion Method (SEM) for the identification of landmines. Chapter 6 introduces this section and reviews the relevant literature, and Chapter 7 gives an overview of the Singularity Expansion Method, the perturbation formulae for buried scatterers and also discusses the Matrix Pencil Method (MPM) as a method of determining the complex resonances of electromagnetic scatterers. Chapter 8 presents Finite-Difference Time-Domain (FDTD) generated results and tests the perturbation formulae. Finally, Chapter 8 concludes the thesis.

Part I

A Comparison of Seismic Migration and Stripmap SAR Imaging Methods for Ground Penetrating Radar for Landmine Detection

Chapter 2

Electromagnetic and Fourier Transform Concepts

In this chapter, important electromagnetic concepts are covered. In addition, the basic concepts of the Discrete Fourier Transform (DFT) in both the time/frequency and spatial/spatial frequency domains are highlighted.

2.1 Basic EM Concepts

All macroscopic electromagnetic (EM) phenomena are governed by Maxwell's Equations:

$$\nabla\times\boldsymbol{E}(\boldsymbol{r},t) = -\frac{\partial}{\partial t}\boldsymbol{B}(\boldsymbol{r},t), \tag{2.1}$$

$$\nabla\times\boldsymbol{H}(\boldsymbol{r},t) = \boldsymbol{J}(\boldsymbol{r},t)+\frac{\partial}{\partial t}\boldsymbol{D}(\boldsymbol{r},t), \tag{2.2}$$

$$\nabla\cdot\boldsymbol{B}(\boldsymbol{r},t) = 0, \tag{2.3}$$

$$\nabla\cdot\boldsymbol{D}(\boldsymbol{r},t) = \rho(\boldsymbol{r},t). \tag{2.4}$$

Where $\boldsymbol{E}$ is electric field intensity, $\boldsymbol{H}$ is magnetic field intensity, $\boldsymbol{D}$ is electric flux density, $\boldsymbol{B}$ is magnetic flux density, $\boldsymbol{J}$ is current density, and ρ is electric charge density. These equations imply the *equation of continuity*,

$$\nabla\cdot\boldsymbol{J}(\boldsymbol{r},t) = -\frac{\partial}{\partial t}\rho(\boldsymbol{r},t), \tag{2.5}$$

and in linear media, the field densities are related to the flux densities via the *constitutive relations:*

$$\boldsymbol{D} = \varepsilon\boldsymbol{E}, \tag{2.6}$$

$$\boldsymbol{B} = \mu\boldsymbol{H}, \tag{2.7}$$

$$\boldsymbol{J} = \sigma\boldsymbol{E}. \tag{2.8}$$

Where ε is the dielectric constant or electric permittivity, μ is the magnetic permeability, and σ is the conductivity of the medium. Together, the three parameters ε, μ and σ determine how a medium reacts to electromagnetic fields. In this document, all **bold** parameters in the equations are vectors.

If we assume a time-harmonic dependency ($e^{j\omega t}$), Maxwell's equations can be written in their time-harmonic form as:

$$\nabla\times\boldsymbol{E}(\boldsymbol{r},\omega) = -j\omega\boldsymbol{B}(\boldsymbol{r},\omega), \tag{2.9}$$

$$\nabla\times\boldsymbol{H}(\boldsymbol{r},\omega) = \boldsymbol{J}(\boldsymbol{r},\omega)+j\omega\boldsymbol{D}(\boldsymbol{r},\omega), \tag{2.10}$$

$$\nabla\cdot\boldsymbol{B}(\boldsymbol{r},\omega) = 0, \tag{2.11}$$

$$\nabla\cdot\boldsymbol{D}(\boldsymbol{r},\omega) = \rho(\boldsymbol{r},\omega), \tag{2.12}$$

with the equation of continuity becoming

$$\nabla\cdot\boldsymbol{J}(\boldsymbol{r},\omega) = -j\omega\rho(\boldsymbol{r},\omega). \tag{2.13}$$

While not shown here, integral formulations of Maxwells equations can also be derived.

If we define the *admittivity* [3] of the medium as

$$\hat{y} = \sigma + j\omega\varepsilon \tag{2.14}$$

and the *impedivity* of a medium as:

$$\hat{z} = j\omega\mu \tag{2.15}$$

then we can define the *wavenumber* as

$$k = \sqrt{-\hat{z}\hat{y}}. \tag{2.16}$$

In lossless media, the wavenumber is purely imaginary, while in lossy media has a wavenumber with a real component.

2.1.1 The Wave Equation

Consider a source free $\boldsymbol{J}(\boldsymbol{r},t) = 0$ (impressed current), $\rho(\boldsymbol{r},t) = 0$), linear, homogenous and isotropic region of space. We can then write the frequency-domain Maxwell's Equations (2.9) and (2.10) as:

$$\nabla\times\boldsymbol{E} = -\hat{z}\boldsymbol{H} \tag{2.17}$$

$$\nabla\times\boldsymbol{H} = \hat{y}\boldsymbol{E}. \tag{2.18}$$

By taking the curl of the first equation, and making a substitution of the second, we can arrive at the equation

$$\nabla\times\nabla\times\boldsymbol{E} - k^2\boldsymbol{E} = 0. \tag{2.19}$$

This is known as the *complex vector wave equation*. The magnetic field also follows the same equation:

$$\nabla\times\nabla\times\boldsymbol{H} - k^2\boldsymbol{H} = 0. \tag{2.20}$$

If we utilize the definition of the Laplacian operator

$$\nabla^2\boldsymbol{A} = \nabla(\nabla\cdot\boldsymbol{A}) - \nabla\times\nabla\times\boldsymbol{A} \tag{2.21}$$

and the fact that the divergence of both $\boldsymbol{E}$ and $\boldsymbol{H}$ are zero, we can arrive at the *vector wave equations*:

$$\nabla^2\boldsymbol{E} + k^2\boldsymbol{E} = 0, \tag{2.22}$$

$$\nabla^2\boldsymbol{H} + k^2\boldsymbol{H} = 0. \tag{2.23}$$

A very important result which is used in this thesis is that each rectangular component of both $\boldsymbol{E}$ and $\boldsymbol{H}$ satisfy the *complex scalar wave equation* or *Helmholtz equation:*

$$\nabla^2\psi + k^2\psi = 0. \tag{2.24}$$

Here, ψ can be replaced by any of the components E_x, E_y, E_z or H_x, H_y, H_z.

We can also write the wave equation in the time domain for a source free region as:

$$\nabla^2\psi - \mu\varepsilon\frac{\partial^2\psi}{\partial t^2} - \mu\sigma\frac{\partial\psi}{\partial t} = 0. \tag{2.25}$$

where μ, ε and σ are the material parameters in the medium.

2.1.2 Seismics and Electromagnetics

If we assume that the earth can be treated as an acoustic medium we may also apply *lossless* ($\sigma = 0$) wave equation in both the time and frequency-domain for source free regions (Zhdanov [5] and Oristaglio et. al. [7]). The difference is that ψ would represent the wave pressure, a scalar quantity, and the term $1/(\mu\varepsilon)$ is replaced with v, the velocity of sound in the medium.

2.2 The General Plane Wave

In general, the most elementary type of plane wave can be represented by the function (Stratton pg 363) [9]:

$$\psi = e^{-jkh + j\omega t}, \tag{2.26}$$

where h represents a length away from the origin, and can be written as:

$$h = \boldsymbol{n} \cdot \boldsymbol{R} = n_x x + n_y y + n_z z, \tag{2.27}$$

where $\boldsymbol{n} = n_x \hat{a}_x + n_y \hat{a}_y + n_z \hat{a}_z$ is the unit normal in the direction of wave travel. We can define the *vector wavenumber* as

$$k\boldsymbol{n} = kn_x \hat{a}_x + kn_y \hat{a}_y + kn_z \hat{a}_z = k_x \hat{a}_x + k_y \hat{a}_y + k_z \hat{a}_z, \tag{2.28}$$

so that the elementary wave function can be written as

$$\psi = e^{-j\boldsymbol{k} \cdot \boldsymbol{R} + j\omega t}. \tag{2.29}$$

We can also write ψ in phasor form as

$$\underline{\psi} = e^{-j\boldsymbol{k} \cdot \boldsymbol{R}} \tag{2.30}$$

Where we have denoted the phasor term with an underscore, used here for clarity, but omitted later. When the non-phasor form of the wave function is introduced into the time-domain scalar wave equation (2.25), we can arrive at the separation equation:

$$k_x^2 + k_y^2 + k_z^2 = \mu\varepsilon\omega^2 - j\mu\sigma\omega = k^2. \tag{2.31}$$

Thus, if any three of k_x, k_y, k_z and ω are determined, the fourth is given by the separation equation, (2.31).

In two-dimensional problems (with space variables y and z), equation (2.31) becomes

$$k_y^2 + k_z^2 = k^2. \tag{2.32}$$

2.3 Green's Functions and the Kirchhoff Integral Equation

2.3.1 Green's Functions

The basic ideas of Green's functions are presented here utilizing only a one-dimensional problem (in time) for simplicity. Green's functions used in electromagnetics require four-dimensions. More in-depth discussion of Green's functions in electromagnetics is given in Morse and Feshbach [13] and D.S. Jones [14]. The aim here is to aid the reader in understanding the use of Green's functions in the Kirchhoff integral equation. The derivation presented here is based on Adomain [12] and many specific details (such as initial conditions of the operator equation and boundary values) are sacrificed to keep the derivation clear.

If we consider an operator equation:

$$Lu(t) = f(t) \tag{2.33}$$

where L is a differential operator, f is called the forcing term and u is the unknown solution to the operator equation. In addition to L being a differential operator, we also require it to be a linear operator with an inverse. Utilizing the existence of the inverse we may write:

$$u(t) = L^{-1}f(t). \tag{2.34}$$

Utilizing the fact that L is linear, and is a differential operator, we can write the solution as an integral type:

$$u(t) = L^{-1}f(t) = \int G(t, \tau)f(\tau)d\tau. \tag{2.35}$$

This equation tells us that if we can find the unknown function $G(\tau, t)$, which we call the *Green's function*, we can then find $u(t)$.

To provide a method of finding the Green's function, we apply the operator L to (2.35)

$$Lu(t) = L\int G(t, \tau)f(\tau)d\tau. \tag{2.36}$$

Utilizing (2.33) and the linearity of L, we can write

$$f(t) = \int LG(t, \tau) f(\tau) d\tau . \tag{2.37}$$

The only way for this equation to hold is if

$$LG(t, \tau) = \delta(t - \tau) . \tag{2.38}$$

Thus, the Green's function is the solution of the operator equation when the forcing term is the dirac delta function $\delta(t - \tau)$. It is important to note that the boundary conditions (and therefore the physical media) will play a part in the solution of the Green's function. We can view this process as finding the solution to the operator equation from a point source, then completing a weighted summing in (2.36), with the weighting function equal to the forcing function $f(t)$.

For clarity, we have considered functions that only depend upon the variable t. In electromagnetics, however, we must consider quantities that vary with both space and time. We therefore write the Green's function in the form:

$$G(\boldsymbol{r}, t | \boldsymbol{r}', t') \tag{2.39}$$

which we can write as the solution to the operator equation L at location $\boldsymbol{r}$ and time t from a point source located at $\boldsymbol{r}'$ and time t' '. The rest of the terms in the above derivation can be similarly modified.

2.3.2 The Kirchhoff Integral Formula

The Kirchhoff integral formula is an integral solution of the scalar wave equation (2.24). A derivation of the solution can be found in D.S. Jones [14]. The formula is presented here without proof, and the associated boundary conditions for the surface S' are discussed in section 4.3. The Kirchhoff integral solution to the scalar wave equation for a source-free medium is

$$\psi(\boldsymbol{r}, t) = -\int_{t'} \oint_{S'} \psi(\boldsymbol{r}', t) \frac{\partial}{\partial n'} G(\boldsymbol{r}, t | \boldsymbol{r}', t') - G(\boldsymbol{r}, t | \boldsymbol{r}', t') \frac{\partial}{\partial n'} \psi(\boldsymbol{r}', t') dS' dt' . \tag{2.40}$$

Where $\psi(\boldsymbol{r}, t)$ is the scalar field solution we are attempting to solve for, S' is the surface of the volume in which we are attempting to find a solution, n' is the outward normal to S', and $\psi(\boldsymbol{r}', t)$ represents the measurements of this scalar field.

2.4 The Continous Fourier Transform

In this thesis, the continous forward Fourier Transform (FT) of a signal $f(u)$ is defined as

$$F(k_u) \equiv \frac{1}{\sqrt{2\pi}} \int_{-\infty}^{\infty} f(u) e^{-jk_u u} du \ , \tag{2.41}$$

and the inverse fourier transform (IFT) is defined as

$$f(u) = \frac{1}{\sqrt{2\pi}} \int_{-\infty}^{\infty} F(k_u) e^{jk_u u} dk_u \ . \tag{2.42}$$

where k_u is the Fourier-domain variable. If the variable u represents time then $k_u = \omega$, the usual frequency-domain Fourier variable. For a spatial variable such as x, we use $u = x$ and $k_u = k_x$. An equivalent transform can be defined with a positive in the exponential term for the forward transform, and a negative in the exponential term for the reverse transform. Both versions of the transform will be used later in this thesis.

In general, we use upper-case letters for the Fourier domain signals, and lower-case letters for non-fourier domain signals.

The continous FT has been thoroughly studied elsewhere and the reader is referred to any standard textbook such as [10].

2.5 The Discrete Fourier Transform

The Discrete Fourier Transform (DFT) is an approximation of the continous fourier transform in a discrete form. If we imagine that we have a discrete u-domain signal of N total samples with a sampling period of Δu. Then instead of

$$F(k_u) \equiv \frac{1}{\sqrt{2\pi}} \int_{0}^{N\Delta u} f(u) e^{-jk_u u} du \tag{2.43}$$

we then have

$$F(k_u) = \frac{1}{\sqrt{2\pi}} \sum_{n=0}^{N-1} f(n\Delta u) e^{-jk_u n\Delta u} \Delta u . \tag{2.44}$$

Note that k_u is still a continous variable. We now sample it at a set of discrete points $k_u^m = 2\pi m/((N-1))\Delta u)$ where $m = 0, 1, \ldots, N-1$ and multiply the transform by $\sqrt{2\pi}/(\Delta u)$. k_u is sampled over a set of points from $-k_{umax}$ to k_{umax}. The effects of this constant scaling term can be cancelled by appropriately defining the inverse transform.

We then define the DFT as

$$F(k_u^m) = \sum_{n=0}^{N-1} f(n\Delta u) e^{-j2\pi m \frac{n}{N}} \tag{2.45}$$

The Inverse DFT (IFDT) can be defined as

$$f(n\Delta u) = \frac{1}{N} \sum_{m=0}^{N-1} F(k_u^m) e^{j2\pi m \frac{n}{N}} . \tag{2.46}$$

For a thorough description of the DFT, see Proakis and Manolakis [11].

2.5.1 Calculating DFT Parameters

The imaging algorithms of part I of this thesis rely heavily on both forward and inverse DFT or collected data. It is important to understand the relations between both Fourier domains and this next section highlights the relations between them.

Consider a sampled signal in the u domain, sampled N times from $u = 0$ to $u = U_{max}$. Here, we assume that N is always an odd number. N being even will cause a slight modification of these formulae. The separation between samples is Δu. If we take the DFT of this signal, we get an N point signal in the frequency domain, which goes from $-k_{u_{max}}$ to $k_{u_{max}}$ (if N is even, this does not hold). In this discussion, we take the select the normalized angular frequency to be from $-\pi$ to π (this is in contrast to the previous

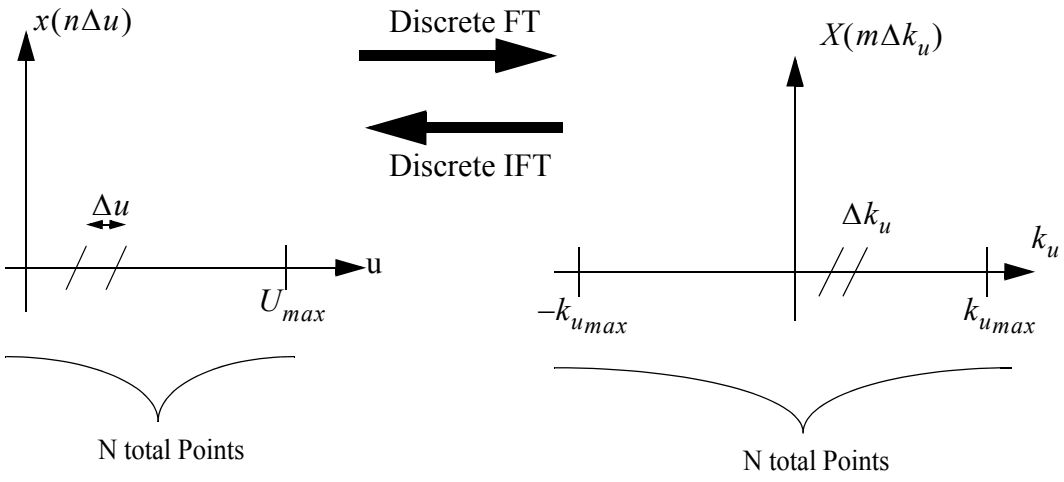

Figure 2.1:The Time Domain Discrete Fourier Transform

set of equations, where we selected a range of 0 to 2π). The separation between samples in the frequency domain is Δk_u. This is graphically represented in Figure 2.1.

Starting with the fact that N sampled points contain $N-1$ intervals:

$$U_{max} = (N-1)\Delta u \text{ and } 2k_{u_{max}} = (N-1)\Delta k_u. \tag{2.47}$$

Using the fact that the sample frequency, F_{sample} is

$$F_{sample} = \frac{1}{\Delta u} \tag{2.48}$$

The Nyquist sampling theorem states that

$$k_{u_{max}} = \frac{2\pi F_{sample}}{2} = \frac{\pi}{\Delta u}. \tag{2.49}$$

Now that we have an equation for relating $k_{u_{max}}$ and Δu, we can find Δk_u and U_{max}, using (2.47). Doing this:

$$\Delta k_u = \frac{2k_{u_{max}}}{(N-1)} = \frac{2\pi}{(N-1)\Delta u} = \frac{2\pi}{U_{max}} \text{ and} \tag{2.50}$$

$$U_{max} = (N-1)\Delta u = \frac{\pi(N-1)}{k_{u_{max}}} = \frac{2\pi}{\Delta k_u}. \tag{2.51}$$

Using this set of equations ((2.50) and (2.51)) and the accompanying figure, we can relate all the desired quantities to each other, for both the discrete fourier transform as well as the discrete inverse fourier transform. To apply a time/frequency domain analysis we simply replace u with t and k_u with ω.

2.5.2 Implementation of DFT and IDFT utilizing a SFCW Radar

When implementing the DFT and DIFT in the practical case of Stepped Frequency Continous Wave (SFCW) radar, we are confronted with the problem of finite bandwidth data. That is, we only collect data from ω_{start} to ω_{stop}. In order for (2.50) and (2.51) to apply, we must have the full bandwidth data. To accomplish this we zero pad the data back to $\omega = 0$, and then construct the negative frequencies from the complex conjugate of this zero-padded data. This step does add processing time to the algorithm. The zero-padding procedure is shown graphically in.Figure 2.2

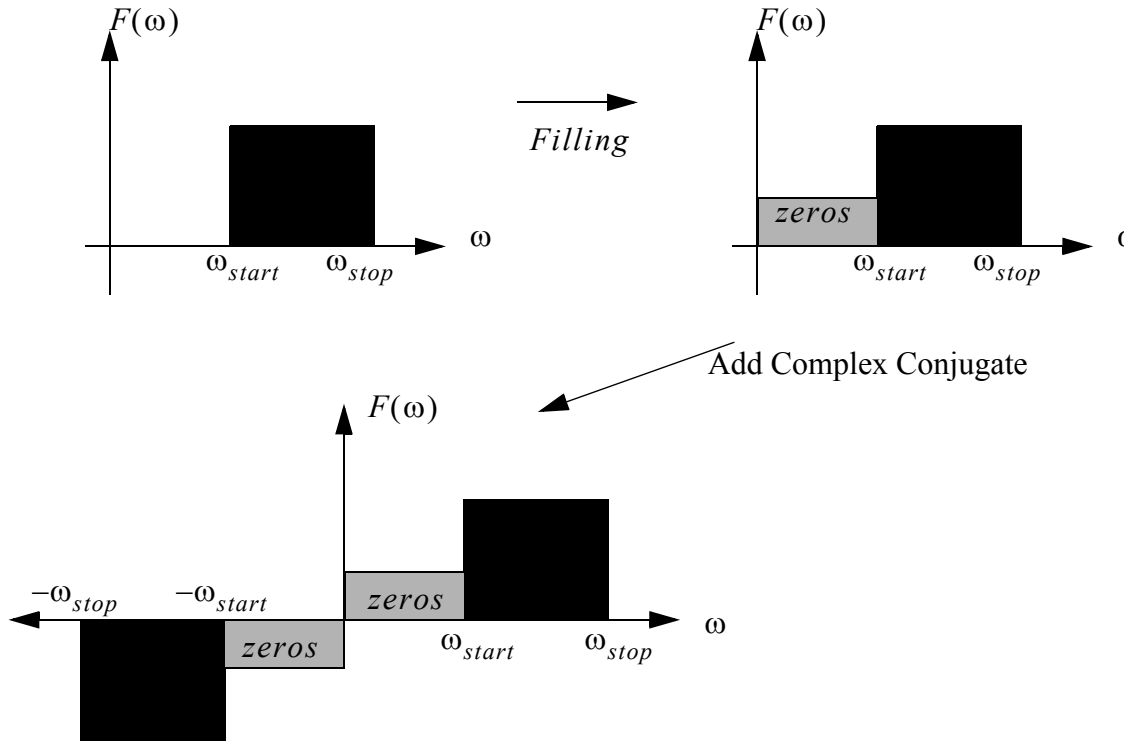

Figure 2.2: Zero Padding of SFCW Radar Data

Chapter 3

Stripmap Synthetic Aperture Radar

In this chapter, we begin with one-dimensional range imaging and show why focusing of these images is desirable. We then present the basic Stripmap Synthetic Aperture Radar (SAR) algorithm, and then give a description of the electromagnetic assumptions used in the Stripmap SAR algorithm.

The concept of Synthetic Aperture Radar (SAR) arose from the radar community when considering the problem of collecting a large amount of data from an aeroplane. The term synthetic aperture is based on the concept of simulating a significantly larger antenna aperture through signal processing, rather than constructing a very large antenna. The advantages of this can be illustrated as follows.

The cross-range, or lateral resolution (L_r) of a radar can be approximated by the equation (Soumekh [6])

$$L_r = \frac{R\lambda}{D}, \tag{3.1}$$

where λ is the operating wavelength, D is the diameter of the antenna, and R is the distance from the target to the antenna. If an antenna has a diameter of $D = 1$ meter, an operating wavelength of $\lambda = 1$ meter, and a target at the range of $R = 50$ meters, then the lateral resolution is 50 meters. If, however, we move our radar along a line, creating an imaginary or effective aperture larger than the physical aperture (diameter) of the antenna, we can improve the cross range resolution significantly. For example, if we moved our radar 200 meters, the effective diameter (aperture) would become $D_{eff} = 200$ and the lateral resolution would become 0.25 meters.

The Stripmap SAR algorithm can be contrasted with what we call *conventional* SAR, where the focusing is completed by convolving the received radar data with the

inverse of the point target response. The so-called conventional SAR can be shown equivalent to the Hyperbolic Summation (HS) algorithm of geophysics (for the HS algorithm, see section 4.2) [15]. The HS method has long ago been replaced by more sophisticated methods, and Stripmap SAR is one of these more advanced methods. As such, conventional SAR will not be covered in this thesis.

The algorithm is presented here as it is seen in the literature [6]; it seems that the background of the authors for the main references in Stripmap SAR do not lie in electromagnetics, rather in signal processing. The standard presentation of the algorithm is devoid of any references to electromagnetics, and the purpose of the last section of this chapter is to delineate a list of electromagnetic assumptions left implicit in the Stripmap SAR algorithm. The three most important assumptions are that we ignore interactions within and between targets (we model only point scatterers), we assume a scalar wave field (i.e. the vectorial character of EM fields is ignored) and we assume that we know the material parameters of the external medium. This discussion facilitates the later comparison of this algorithm with seismic imaging techniques of chapter 4.

The Stripmap SAR algorithm is used extensively in modern radar systems, for example the E-3 AWACS (Airborne Warning and Control System) aeroplanes, NASA space shuttles and satellite borne radars all implement some variation of this algorithm [6].

3.1 Basic GPR Imaging Terminology

3.1.1 A-scans

When dealing with GPR images, we can define several different types of ‘scans’. The so-called A-scan, which is also known as a range profile, is the result of a single pulse (or sweep of frequencies) of a radar. For this type of example, we can imagine an antenna transmitting a pulse, then plotting the magnitude of the voltage received at the received antenna. Knowing the speed of light in the medium of interest, we could plot the return on

a spatial axis. A graphical example of the A-scan, with two targets, is shown in Figure 3.1. The A-scan shown might be a return that we would expect from a GPR with the larger peak being the ground reflection and the smaller peak being a possible target.

3.1.2 B-scans, Range and Cross-Range

A B-scan is simply a succession of stacked A-scans. Here, we can imagine that we take a series of A-scans over a single line (we move the antennas along the y axis). At a set distance, Δy, we perform an A-scan. The best way to display this resulting image is in

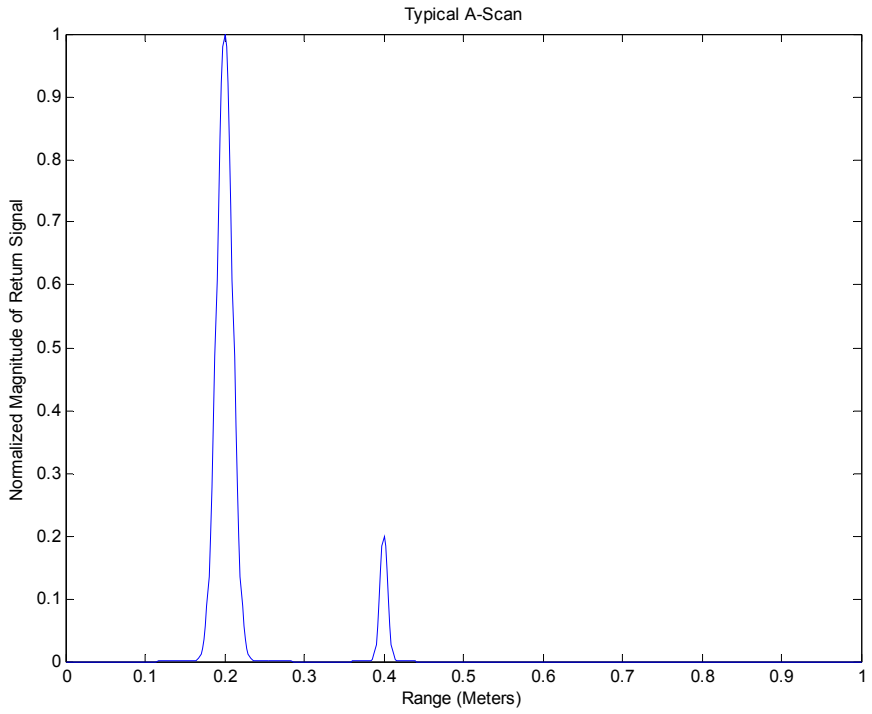

Figure 3.1: Example of A-Scan

a 2-D plot, with areas of increasing intensity representing scattering objects. An example

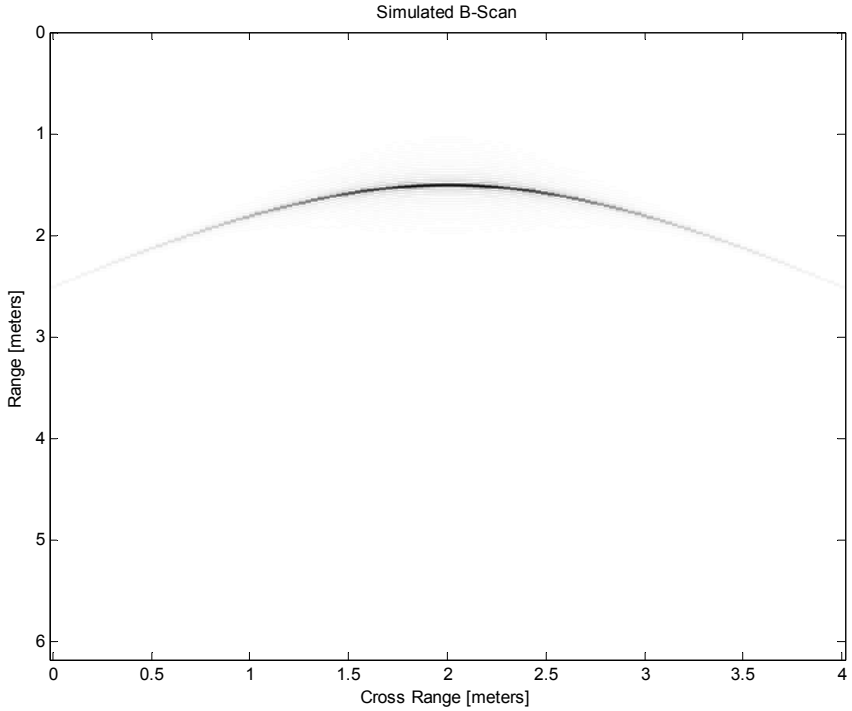

Figure 3.2: Example of B-Scan

of B-scan is shown in Figure 3.2. This figure does not directly relate to Figure 3.1, but is a B-scan from a single point target.

The *range* is defined as the distance away from the antenna, the *cross-range* is the distance that the antenna has moved (in Figure 1.2, it would be the distance moved in the y direction). This B-scan gives the response expected from a point target at location $(y, z) = (2, 1.5)$). The reasons behind the hyperbolic shape of this B-scan will be explored more thoroughly in 3.2.2.

3.1.3 C-scans

C-scans are defined as a series of stacked B-scans. Due to the fact that our experimental data collection can, at this time, only be done on a single plane, C-scans will not be used in this thesis.

3.2 One Dimensional Range Profiling

To understand the imaging algorithms in this thesis, it is important to first understand basic 1-D imaging. We show here how a single A-scan or range profile can be constructed. Consider the problem shown in Figure 3.3. This is the case of a 1-D plane wave impinging on a point target located at a distance D from the transmitter. We model the expected return signal $S(\omega)$, as:

$$S(k) = \rho A e^{-j2\frac{\omega}{c}D} \tag{3.2}$$

where A is the amplitude of the illuminating plane wave, ρ is a frequency independent measure of the reflectivity of the reflecting plane, D is the distance from the transmitter to the conducting sheet, and c is the speed of light in the surrounding medium.

We now take the IFT of the signal $S(\omega)$, and the resulting time-domain signal is

$$s(t) = \frac{\rho A}{\sqrt{2\pi}}\delta\left(t - 2\frac{D}{c}\right). \tag{3.3}$$

This equation is a dirac delta function with a scaling term and we note that only phase information is used.

To then map this data into the spatial domain, we simply scale the time axis using the equation

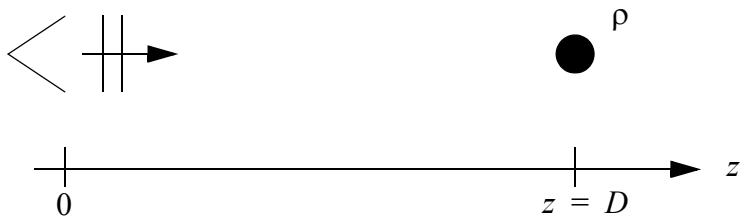

Figure 3.3: A 1-D Plane Wave Illuminating a Perfectly Conducting Half Space

$$z = c\frac{t}{2}. \tag{3.4}$$

Thus, equation (3.4) would become

$$s(z) = \frac{\rho A}{\sqrt{2\pi}}\delta\left(\frac{2z}{c} - \frac{2D}{c}\right) = \frac{\rho A}{\sqrt{2\pi}}\delta\left(\frac{2}{c}(z - D)\right) \tag{3.5}$$

which is equivalent to

$$s(z) = \frac{\rho A}{\sqrt{2\pi}}\delta(z - D). \tag{3.6}$$

Which is a scaled dirac delta function at the point D, which represents the physical distance from the antenna. Using this transformation, we can switch from the time to distance axis and vice versa.

3.2.1 Single Point Target from Two Locations

We now consider performing a range profile of a single target from multiple antenna positions. The problem setup is shown in Figure 3.4. Here, we imagine that we complete a

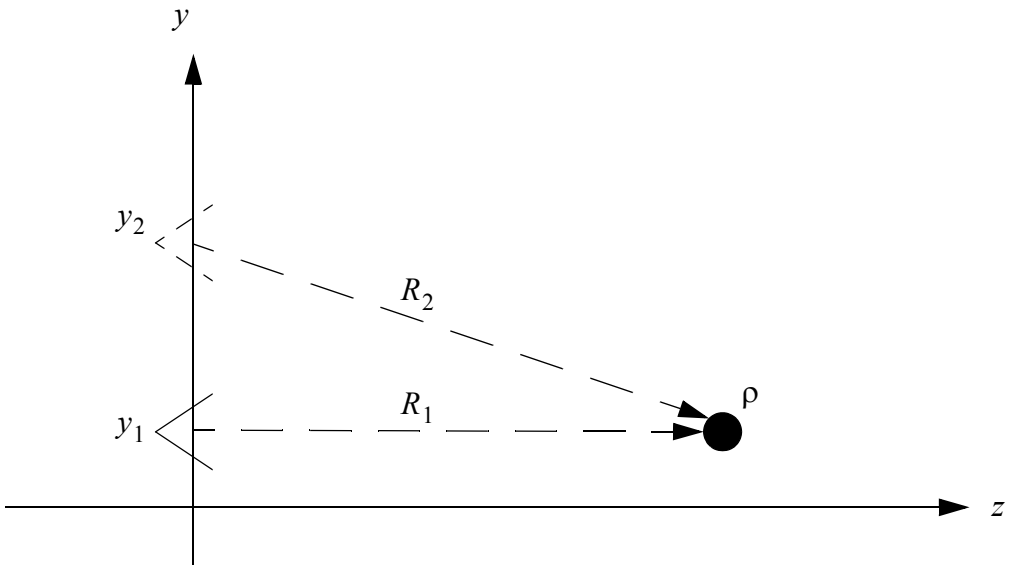

Figure 3.4: Range Imaging of Single Point Target from Two Locations

range profile with the antenna at position y_1, then complete another range profile with the antenna at position y_2.

The received signals from each range profile, $S_1(k)$ and $S_2(k)$ are modelled as

$$S_1(k) = \rho A e^{j2kR_1} \text{ and } S_2(k) = \rho A e^{j2kR_2}, \tag{3.7}$$

which in the time domain become

$$s_1(t) = \frac{\rho A}{\sqrt{2\pi}}\delta\left(t - \frac{2R_1}{c}\right) \text{ and } s_2(t) = \frac{\rho A}{\sqrt{2\pi}}\delta\left(t - \frac{2R_2}{c}\right). \tag{3.8}$$

If we then map the time domain into the spatial domain z, we arrive at:

$$s_1(z) = \frac{\rho A}{\sqrt{2\pi}}\delta(z - R_1) \text{ and } s_2(t) = \frac{\rho A}{\sqrt{2\pi}}\delta(z - R_2). \tag{3.9}$$

These two signals are shown in Figure 3.5.

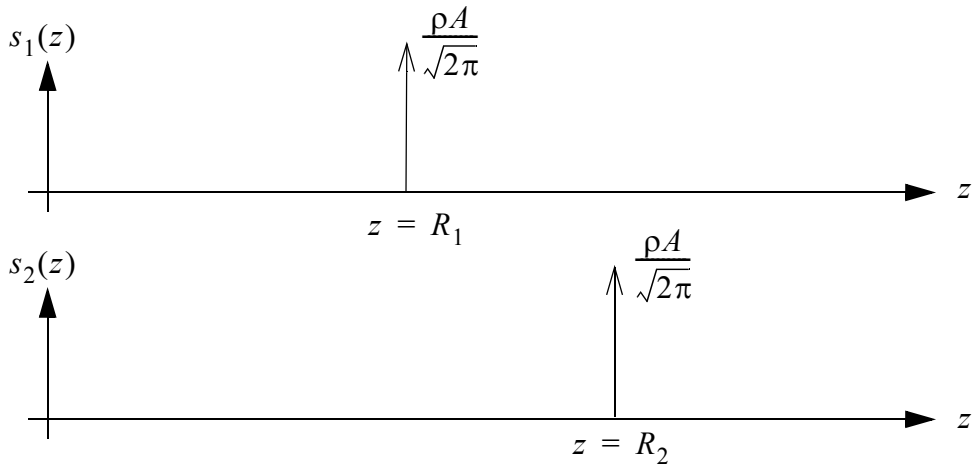

Figure 3.5: Range Profiles of a Single Target from Two Positions

Thus, performing a standard range profile on a target results in a Dirac delta function located on the z axis at R, the distance between the antenna and target.

3.2.2 Target Hyperbolas and B-scans

We now consider the case of a single point target where we are moving our antenna along a path defined by $z = 0$, as shown in Figure 3.6. The distance between antenna and

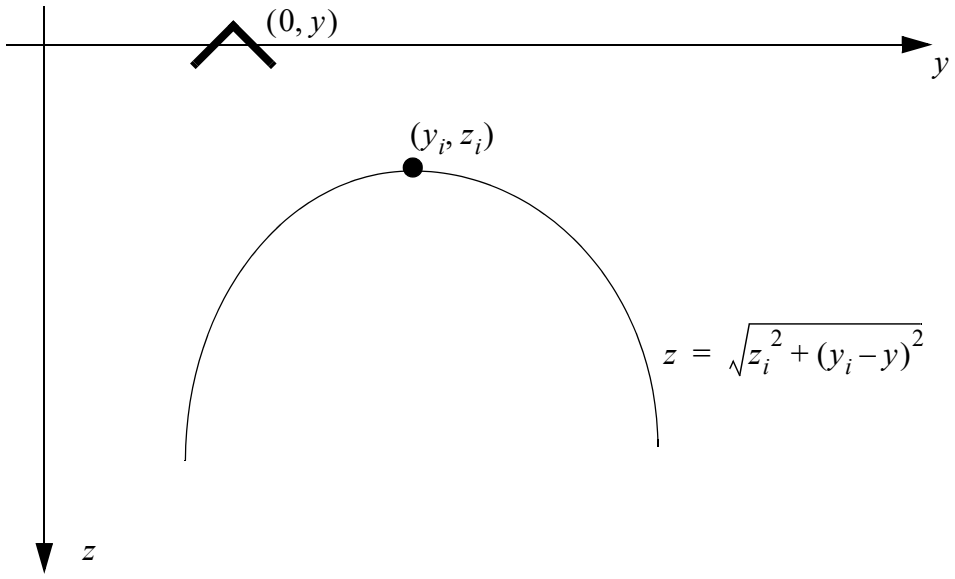

Figure 3.6: Graphical Representation of How Target Hyperbola Occurs

target, R_i as

$$R_i = \sqrt{z_i^2 + (y_i - y)^2}. \tag{3.10}$$

When we perform a range profile of this target at the distance R_i, we get a Dirac delta function at $z = R_i$. We can then create an image by stacking all these range profiles together, resulting in a B-scan. Thus in our image,

$$z = R_i = \sqrt{z_i^2 + (y_i - y)^2}. \tag{3.11}$$

This describes a half-hyperbola in the $z \geq 0$ plane:

$$z^2 - (y - y_i)^2 = z_i^2. \tag{3.12}$$

The hyperbola phenomena seen here gives rise to SAR focusing algorithms, as point targets become obscured with hyperbolae. To a certain extent, we can consider SAR (and seismic migration techniques) a process of focusing these hyperbolae back to point targets.

3.3 The Stripmap SAR Algorithm

The Stripmap SAR derivation (Soumekh [6]) begins by considering n point targets located in a 2 dimensional space with the ith target having coordinates (y_i, z_i) and some measure of the targets reflectivity, ρ_i. The general setup is shown in Figure 3.7.

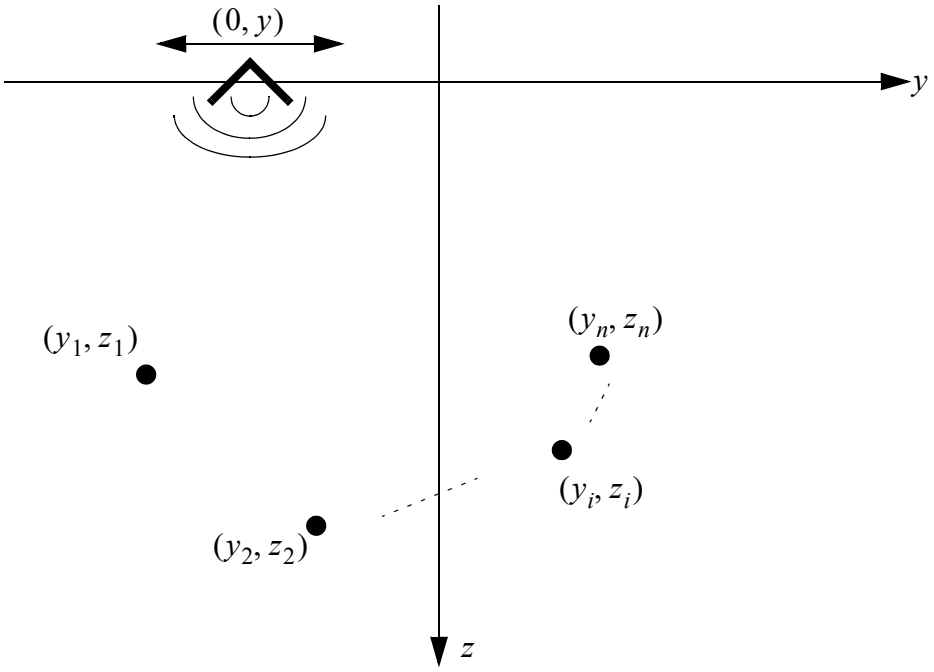

Figure 3.7:Stripmap SAR Setup

We assume that the radar emits a pulse $p(t)$ at all points on the y axis. In the practical situation we will clearly not have this (the radar will emit a pulse at a set of evenly spaced points on the y axis), however, for the derivation, we assume a continuous variable. Assuming a lossless media, we then model the received signal $s(y, t)$ as:

$$s(y, t) = \sum_{i=1}^{n} \rho_i p\left(t - \frac{2\sqrt{z_i^2 + (y_i - y)^2}}{c_m}\right) \tag{3.13}$$

where c_m is the speed of light in the surrounding medium, and as is usual in this derivation, we have neglected the attenuation term associated with each point. This is justified by the much greater importance of the phase terms. The initial modeling equation has bur-

ied in it many assumptions about the system. To maintain the flow of the derivation, these details are dealt with in section 3.4.

If the Fourier Transform, in the time domain, is taken of equation (3.13), we get

$$S(y, \omega) = \left(\frac{1}{2\pi}\right)^{\frac{1}{2}} P(\omega) \sum_{i=1}^{n} \rho_i e^{-j2k\sqrt{z_i^2 + (y_i - y)^2}}, \tag{3.14}$$

where $k = \omega / c_m$ is the wavenumber for lossless media and $P(\omega)$ is the FT of the transmitted pulse. Here, and for the rest of this derivation, we have utilized a '-' sign in the forward fourier transform for all variables.

The next step is to take the FT in the spatial domain, k_y. To solve the resulting integral, we make use of the *method of stationary phase* [16], and arrive at:

$$S(k_y, \omega) = \left(\frac{1}{2\pi}\right) P(\omega) \sum_{i=1}^{n} \rho_i e^{-j\sqrt{4k^2 - k_y^2} z_i - jk_y y_i}. \tag{3.15}$$

Here, we have neglected another amplitude term $e^{-j(\pi/4)} / (\sqrt{4k^2 - k_y^2})$, which results from the use of the method of stationary phase. It is important to note that the phase term in (3.15) is linear in both y_i and z_i.

We now change flow in this derivation and consider how we would define the 'ideal' image for these point targets. A reasonable 'ideal' image would be:

$$g_o(y, z) = \sum_{i=1}^{n} \rho_i \delta(y - y_i, z - z_i), \tag{3.16}$$

where $\delta(y - y_i, z - z_i)$ is the usual two dimensional Dirac delta function. The spatial FT of this image in both the y and z directions is:

$$G_o(k_y, k_z) = \left(\frac{1}{2\pi}\right) \sum_{i=1}^{n} \rho_i e^{-jk_y y_i - jk_z z_i}. \tag{3.17}$$

If we compare equations (3.17) and (3.15), we can identify

$$G_o(k_y, k_z) = \frac{S(k_y, \omega)}{P(\omega)}, \tag{3.18}$$

where we make use of the so-called spatial frequency mapping equation:

$$k_z = \sqrt{4k^2 - k_y^2} = \sqrt{\frac{4\omega^2}{c_m^2} - k_y^2}. \tag{3.19}$$

By taking the spatial IFT of (3.18), we can construct the imaging equation as

$$F_{SAR}(y, z) = \frac{1}{2\pi} \int_{-\infty}^{\infty} \int_{-\infty}^{\infty} \frac{S(k_y, k_z)}{P(\omega)} e^{j(k_y y + k_z z)} dk_y dk_z \tag{3.20}$$

where $S(k_y, k_z)$ is $S(k_y, \omega)$ after we have utilized the spatial frequency mapping equation (3.19).

In summary, what this derivation shows is that to build the focused image, we take our collected data, $s(y, t)$, take the FT in both the ω and k_y directions, divide by the FT of the pulse $P(\omega)$, then take the IFT in the k_y and k_z directions. We also require a $1/(2\pi)$ scaling term to make this equation a true FT, but this factor is unimportant for imaging purposes. In the case of SFCW radar, $P(\omega) = 1$ over all frequencies of interest, and we collect data in the $S(y, \omega)$ domain and therefore we can begin our image construction at equation (3.14).

3.3.1 The Interpolation Problem in Stripmap SAR

While the above derivation was done with continous variables, in practical situations we have only discrete variables. Specifically, the radar will collect a set of evenly spaced discrete points in the t domain which leads to a set of evenly spaced points in the ω domain, when utilizing the efficient Fast Fourier Transform (FFT). We also collect data at a set of evenly spaced discrete points in the y domain (i.e. $y = n\Delta y$) and this leads to a set of evenly spaced discrete values of k_y.

In order to evaluate the imaging equation, (3.20), we require that our data lies in the k_y and k_z domain. To shift the data in the (k_y, ω) to the (k_y, k_z) domain we utilize the spatial frequency mapping equation (3.19). Due to its non-linearity, (3.19) takes what was evenly spaced points in the ω domain and creates a set of unevenly spaced points in the k_z domain. Efficient evaluation of (3.20) using the FFT requires evenly spaced points in both the k_z and k_y domains. In order to achieve the evenly spaced points in the k_z domain, interpolation is required.

While at first this problem may seem trivial, improper consideration of the interpolation problem will result in non or poorly focused images. In addition, this interpolation step ends up being the slowest part of the Stripmap SAR algorithm. In order to avoid confusion in the basic understanding of the Stripmap SAR algorithm, a detailed exposition of the interpolation process is given in Appendix A.

3.3.2 Graphical Representation of The Stripmap SAR Algorithm

A graphical representation of the Stripmap SAR algorithm for at the 2-D problem is presented in Figure 3.8.

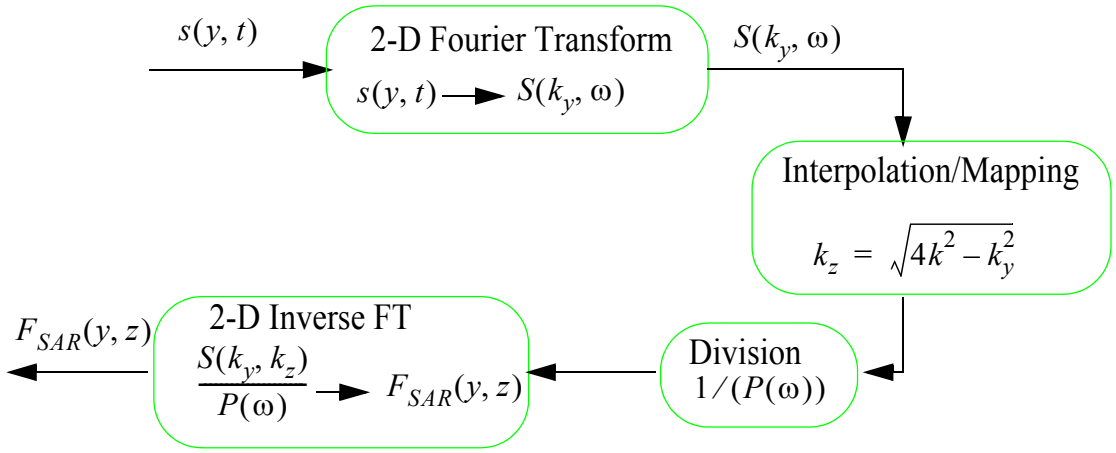

Figure 3.8: Graphical Representation of the 2-D Stripmap SAR Algorithm

3.4 Electromagnetic Assumptions in Stripmap SAR

In the Stripmap SAR derivation just presented no electromagnetic considerations were made. In this section, we will provide a list of electromagnetic assumptions that are made in the algorithm which we hope will provide an alternate way of seeing the Stripmap SAR algorithm. To the author's knowledge, this has not been published previously. We begin by considering equation (3.13), which provides the initial model for the Stripmap SAR algorithm.

The most important electromagnetic assumption made in (3.13) is that we model our scatterers as isotropic point scatterers only. This is equivalent to ignoring all interactions

both between, and within scatterers, which might be called a first-order scattering approximation. The justification given in the literature [6] for the point target approach to the derivation of the Stripmap SAR algorithm is that larger targets can be made up of a summation of these point targets. This assumption may not be valid, but for practical situations seems to work reasonably well (i.e. it does provide focused images).

Secondly, we assume that we have knowledge of the speed of light in the surrounding medium, which is equivalent to knowing the material parameter ε of the medium. Most practical media have $\mu = \mu_o$. We also assume a lossless medium (conductivity is zero).

In addition, we ignore the $1/R$ decay associated with EM fields. In other words, only phase information is used in this modelling equation.

We can also notice that equation (3.13) does not make any reference to the vectorial character of EM fields. That is, it assumes a scalar wavefield. We can interpret this as an assumption that the radar system radiates and receives only one of the 6 (rectangular) scalar components of the full vector wavefield. This assumption is identical to the one made when we apply seismic imaging techniques to the EM problem, and in practical situations this approximation does work (i.e. the algorithm provides focused images) because antennas usually radiate and receive only one vector component of the EM field.

3.4.1 The Vector Wavenumber in Stripmap SAR

In this section, we take a closer look at the spatial frequency mapping equation, equation (3.19). From section 2.2, we know that in the two dimensional problem considered in the Stripmap SAR derivation, the vector wavenumber should satisfy the equation:

$$k_y^2 + k_z^2 = k^2 = \frac{\omega}{c_m^2}^2 . \tag{3.21}$$

However, from (3.19), we see that we have the entirely unsatisfying result that

$$k_y^2 + k_z^2 = \frac{4\omega^2}{c_m^2} . \tag{3.22}$$

After an analysis of the Stripmap SAR derivation procedure, we can note that this discrepancy occurs because we have to take into account both the forward and return time of the EM wave. The problem can be solved by applying the exploding source model.

3.4.2 The Exploding Source Model

In order to finish the EM interpretation of Stripmap SAR and to later compare Stripmap SAR and the seismic based Frequency-Wavenumber migration (which is covered in chapter 4), we first must apply a sum of plane waves explanation of Stripmap SAR. To accomplish this, we first apply the exploding source model to Stripmap SAR.

The exploding source model was first introduced by Claerbout [20]. It is fundamental to the solution of wave equation based migration techniques discussed in chapter 4. In the exploding source model it is assumed that the scattered field originates from sources located at the scatters. At time $t = 0$ these sources 'explode' and send travelling waves to the detectors at the surface. To adapt to this new model, we must replace the velocity of propagation in the medium, c_m, with half its original value:

$$v_m = \frac{c_m}{2}. \tag{3.23}$$

We can then show that equation (3.13) is equivalent to each point source radiating a plane wave in all directions, with a varying amplitude term. This is explored in the next section.

3.4.3 A Plane Wave Interpretation of Stripmap SAR Algorithm

Consider the phasor form of a general scalar plane wave in the frequency domain:

$$\underline{\Psi} = e^{-j\boldsymbol{k}\cdot\boldsymbol{R}} = e^{-jk\boldsymbol{n}\cdot\boldsymbol{R}}, \tag{3.24}$$

where $k = \omega / v_m$ (i.e. we are using the exploding source model), and $\boldsymbol{n}$ is the unit normal in the direction of travel of the plane wave,. In this consideration, we have centered our coordinate system on the point scatterer, and the antenna located at the point (y_b, z_b). The

problem setup is shown in Figure 3.9. We now assume that the wave emitted from the

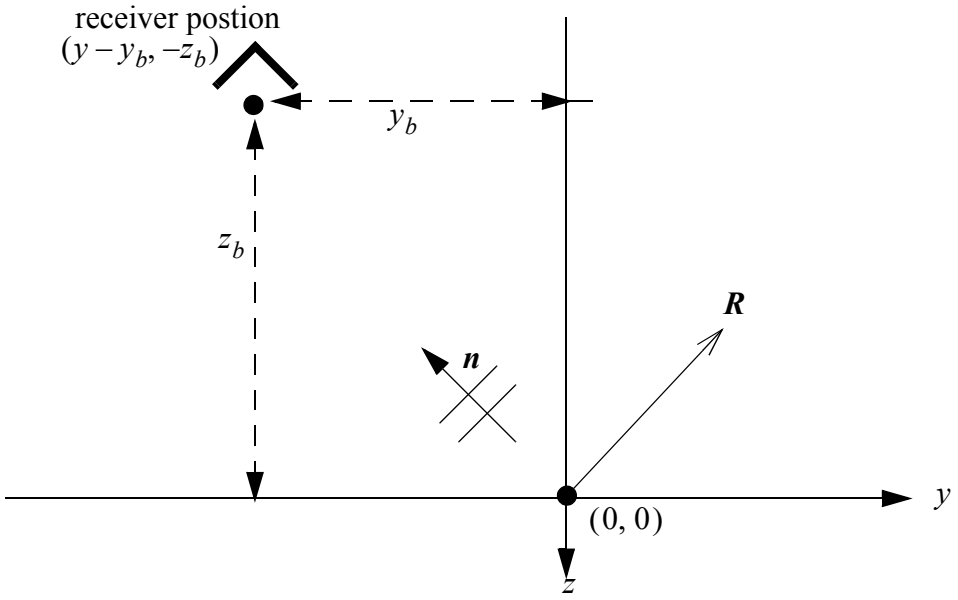

Figure 3.9: Plane Wave Interpretation of Stripmap SAR

point source (via the exploding source model) to be a plane wave by the time it reaches the antenna. We can describe the unit normal of this wave, $\boldsymbol{n}$, as:

$$\boldsymbol{n} = \frac{(y-y_b)\hat{a}_y - z_b\hat{a}_z}{\sqrt{z_b^2 + (y-y_b)^2}}. \tag{3.25}$$

Thus vector wavenumber is given by $\boldsymbol{k} = k\boldsymbol{n}$. The scalar wave is received at the point

$$\boldsymbol{R} = (y-y_b)\hat{a}_y - z_b\hat{a}_z. \tag{3.26}$$

We can then write the received signal $S(\omega, y)$ as

$$S(\omega, y) = L(\omega, y)e^{-jk\frac{(y-y_b)\hat{a}_y - z_b\hat{a}_z}{\sqrt{z_b^2+(y-y_b)^2}} \bullet (y-y_b)\hat{a}_y - z_b\hat{a}_z} = L(\omega, y)e^{-jk\sqrt{z_b^2+(y-y_b)^2}}, \tag{3.27}$$

where $L(\omega, y) = \rho P(\omega)$ takes into account the pulse shape and the reflectivity. If we note that $k = \omega / v_m = 2\omega / c$, and that $\sqrt{z_b^2 + (y-y_b)^2}$ is simply the distance from the scatterer to the antenna, we can see that equation (3.13), the initial modelling equation for stripmap SAR, can be considered as a sum of scalar plane waves emanating from each

point target at half the actual medium velocity. To reiterate, (3.13) makes the approximation that the receiver is in the far field (i.e. the signal is a plane wave) and considers only phase differences in the received signal.

Chapter 4
Seismic Migration

This chapter begins by describing seismic migration techniques. It begins with the basic geometric method of Hyperbolic Summation, then introduces the wave field migration algorithms of Kirchhoff Migration and Frequency Wavenumber Migration. The exploding source model is required for the wave field techniques, and is described in section 4.1.

Migration is the term used by geophysicists to describe the process of focusing the basic B-scan images to more closely resemble the physical target dimensions. These images arise from a seismic system similar to a GPR, but radiating sound waves instead of electromagnetic waves. Early seismic algorithms, such as Hyperbolic Summation, were based on a geometric approach and paid little attention to the physics of seismic wave propagation. More advanced techniques of migration based on the scalar wave equation were introduced in the late 1970's and early 1980's. A good overview of the more advanced techniques is given in Berkhout [19].

The same three basic assumptions made in the Stripmap SAR algorithm are made for seismic algorithms. Once again, migration techniques model point scatterers only. Interactions inside, and between targets are ignored. We again assume a lossless ground and knowledge of the ground constitutive parameters (i.e. we assume knowledge of the velocity of propagation in the medium). The third assumption that only one EM field component is radiated and received is implicit in the application of seismic algorithms to an EM problem, as seismic algorithms are based on the scalar wave equation.

The migration methods in this chapter are presented in 3 dimensions, but all are easily modified to two dimensional problems. Much of this series of derivations is based on Scheers [18].

4.1 The Exploding Source Model

The wave equation based seismic algorithms of Kirchhoff Migration and Frequency-Wavenumber migration require the application of the exploding source model, discussed previously in section 3.4.2. Essentially, we replace the actual medium velocity with half its true value ($v_m = c_m/2$).

Under the exploding source model, wavefield migration consists of two basic concepts:

1. Backward extrapolation of the received signal to the exploding sources.
2. Defining the image as the backward extrapolated wave field at time $t = 0$.

In other words, migration consists of back propagating the received wave front to the instant the targets 'explode'. The image is then the scalar field at the instant before it begins to propagate.

The geometry of the exploding source model is shown in Figure 4.1. Here, we again

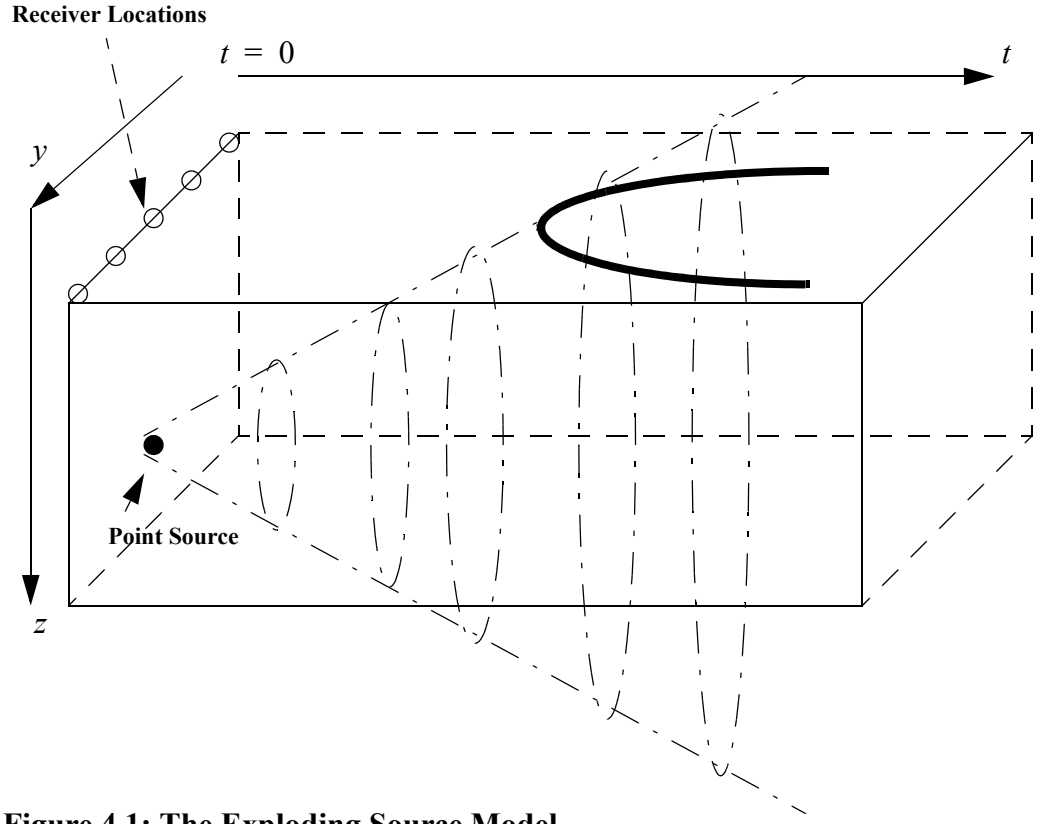

Figure 4.1: The Exploding Source Model

see the target hyperbolas seen in SAR imaging. The receiver locations are physically located on the plane $z = 0$, and record the data over the entire y-t plane. We also assume a constant velocity throughout the entire medium surrounding the point target. Viewed through this diagram, seismic migration is an attempt to take the data received in the y-t plane and extrapolate it back to the y-z plane.

Here, we may note that we make the same three assumptions used in Stripmap SAR. For point targets to 'explode' in this fashion, we require no interactions between point targets. We again assume knowledge of the velocity in the surrounding medium, and the assumption about having only scalar wave fields is inherent to seismics.

4.2 Hyperbolic Summation

Hyperbolic Summation (HS), also known as diffraction summation, is a simple geometric approach to seismic migration. It is presented here because it provides a good introduction to seismic migration and helps one to understand the more complicated Kirchhoff Migration algorithm.

The HS algorithm starts with the assumption that *every point* in the desired image has been created by a diffraction hyperbola, as shown in Figure 4.1. To migrate each point in the image, (x, y, z), we sum the recorded data (which is the scalar wavefield at the location $z = 0$) along the calculated hyperbola. The shape of the hyperbola to sum over will depend upon the depth of the point to be migrated, and the medium velocity. If there was a point scatterer located at (x, y, z), the amplitudes of the hyperbolae towards a large value. If there is no point scatterer (i.e. a noise source), the data will sum towards a much smaller value.

If we imagine that we have collected (have knowledge of) the scalar field, ψ on the $z = 0$ plane at a set of discrete points, or $\psi(x_i, y_j, z = 0, t)$ where $i = 1, 2 \ldots I$ and $k = 1, 2 \ldots K$. The migrated image can then be expressed as:

$$F_{HS}(x, y, z) = \sum_{i=1}^{I} \sum_{k=1}^{K} \psi\left(x_i, y_k, z = 0, t = \frac{2R_{i,k}}{c_m}\right) \tag{4.1}$$

where $R_{i,j}$ is the distance between the measuring position $(x_i, y_j, z = 0)$ and the point to be migrated (x, y, z), and c_m is the velocity of light in the medium.

As we are concerned with 2-D images in this thesis, we write the Hyperbolic Summation algorithm as:

$$F_{HS}(y, z) = \sum_{k=1}^{I} \psi\left(y_k, z = 0, t = \frac{2R_k}{c_m}\right) \tag{4.2}$$

One advantage of this method is that we can select a sub-region to migrate (by selectively picking our (x, y, z) points). However, it does not take the physics of wave propagation into account, and has been superseded by more advanced methods. As such, no images focused by this method are presented.

4.3 Kirchhoff Migration

Kirchhoff Migration (KM), which is also known as reverse-time wave equation migration or wave field extrapolation, is based on an integral solution of the scalar wave equation:

$$\nabla^2\psi(\boldsymbol{r}, t) - \frac{1}{v_m^{\,2}}\frac{\partial^2}{\partial t^2}\psi(\boldsymbol{r}, t) = 0\,. \tag{4.3}$$

As per the exploding source model, $v_m = c_m/2$. The boundary conditions on the scalar wave equation specify ψ on the local ground surface (our collected data), and also specify that $\psi(\boldsymbol{r}, t) \to 0$ as $\boldsymbol{r} \to \infty$ The diagram associated with this problem is shown in Figure

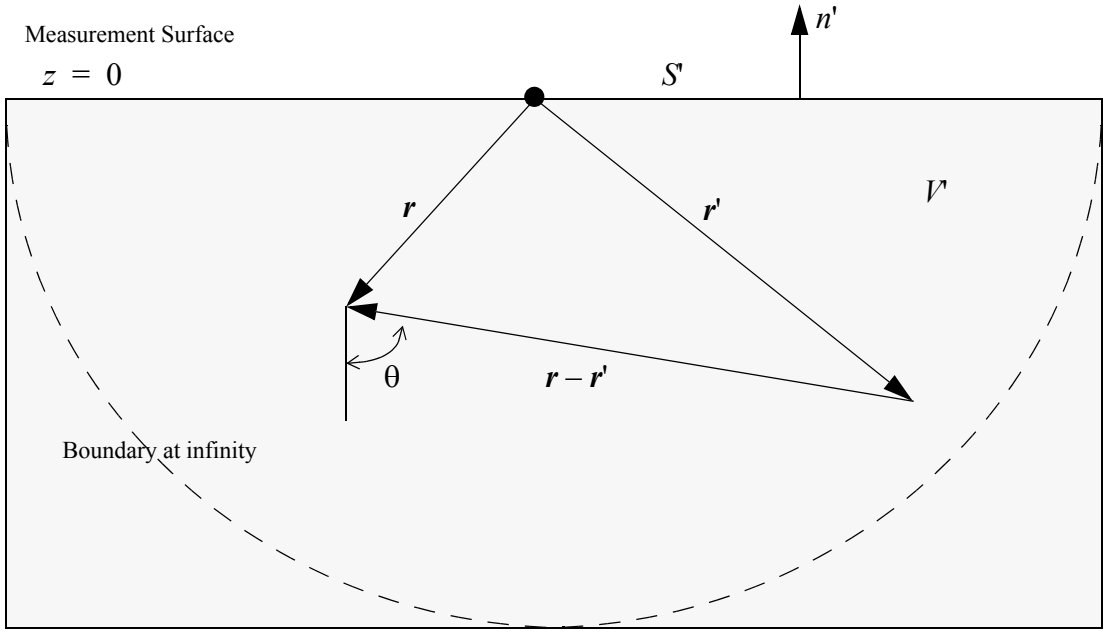

Figure 4.2: Kirchhoff Migration Coordinate System

4.2. In this diagram, we have the associated quantities:

- $\boldsymbol{r}$ is the location of the observer
- t is the time of the observer
- $\boldsymbol{r}'$ is the location of the point source over which we integrate

- t' is the time of the source point
- S' is the surface containing all the sources, consisting of the data plane and the infinite hemispheric half-space in $z < 0$.
- n' is the outward normal to S'
- $\psi(\boldsymbol{r}, t)$ is the scalar wave field at location $\boldsymbol{r}$ and time t
- $\psi(\boldsymbol{r}', t')$ is the scalar wave field that results from a source at point $\boldsymbol{r}'$ and time t'.

The Green's Function is chosen to satisfy the same wave equation, but with Dirichlet Conditions on the ground surface ($G = 0$ on S'). Using the image principle, our Green's function is:

$$G(\boldsymbol{r}, t|\boldsymbol{r}', t') = g(x, y, z, t|x', y', z', t') - g(x, y, z, t|x', y', -z', t') \tag{4.4}$$

where $g(\boldsymbol{r}, t|r', t')$ is the basic free space Green's function:

$$g(\boldsymbol{r}, t|r', t') = \frac{1}{4\pi}\frac{\delta(t - t' + |\boldsymbol{r} - \boldsymbol{r}'|/v)}{|\boldsymbol{r} - \boldsymbol{r}'|}. \tag{4.5}$$

With this Green's Function we now write the Kirchhoff Integral (equation (2.40)) [13] as

$$\psi(\boldsymbol{r}, t) = -\int_{t'}\oint_{S'}\psi(\boldsymbol{r}', t)\frac{\partial}{\partial n'}G(\boldsymbol{r}, t|\boldsymbol{r}', t') - G(\boldsymbol{r}, t|\boldsymbol{r}', t')\frac{\partial}{\partial n'}\psi(\boldsymbol{r}', t')dS'dt'. \tag{4.6}$$

Our choice of G specified that, on S',

$$G(\boldsymbol{r}, t|\boldsymbol{r}', t') = 0 \tag{4.7}$$

and we note that

$$\frac{\partial}{\partial n'}G(\boldsymbol{r}, t|\boldsymbol{r}', t') = 2\frac{\partial}{\partial n'}g(\boldsymbol{r}, t|r', t'). \tag{4.8}$$

From these, we can write the scalar wave field as

$$\psi(\boldsymbol{r}, t) = -2\int_{t'}\oint_{S}\psi(\boldsymbol{r}', t')\frac{\partial}{\partial z'}g(\boldsymbol{r}, t|r', t')dS'dt' \quad , \tag{4.9}$$

where $n' = -z'$ on the ground surface. This integral is known as the Rayleigh integral [5]. Taking into account the following identity for the Green's function:

$$\frac{\partial}{\partial z'}g(\boldsymbol{r}, t|r', t') = -\frac{\partial}{\partial z}g(\boldsymbol{r}, t|r', t'), \tag{4.10}$$

the scalar wave field can be written as

$$\psi(\boldsymbol{r}, t) = -2\frac{\partial}{\partial z}\int_{t'}\oint_{S}\psi(\boldsymbol{r}', t')(g(\boldsymbol{r}, t|r', t'))dS'dt'. \tag{4.11}$$

This equation gives us a solution for the scalar wavefield for all times at any location. What it tells us is that, in order to find the scalar wavefield at all locations for all time, we take our collected data on the $z = 0$ plane, $\psi(\boldsymbol{r}', t')$, take the derivative (in the z direction) of the free space Green's function, then integrate over both time and the $z = 0$ surface.

Different practical implementations of Kirchhoff Migration will vary depending on the approximation used for the derivative of the free space Green's function, $\frac{\partial}{\partial z} g(\boldsymbol{r}, t | r', t')$.

For the first order approximation, we can write (utilizing the Taylor expansion):

$$\frac{\partial g}{\partial z} = \frac{1}{4\pi} \frac{1}{|\boldsymbol{r} - \boldsymbol{r}'|} \frac{\partial}{\partial z} \delta(t - t' + |\boldsymbol{r} - \boldsymbol{r}'| / v_m) + O\left(\frac{1}{|\boldsymbol{r} - \boldsymbol{r}'|^2} \right), \tag{4.12}$$

then, utilizing the identity

$$\frac{\partial}{\partial z} F(G(z)) = F'(G(z)) \frac{dG}{dz}, \tag{4.13}$$

we can write

$$\frac{\partial}{\partial z} \delta(t - t' + |\boldsymbol{r} - \boldsymbol{r}'| / v_m) = \delta'(t - t' + |\boldsymbol{r} - \boldsymbol{r}'| / v_m) \frac{1}{4\pi v_m} \frac{\partial}{\partial z} |\boldsymbol{r} - \boldsymbol{r}'| \tag{4.14}$$

and

$$\frac{\partial}{\partial t'} \delta(t - t' + |\boldsymbol{r} - \boldsymbol{r}'| / v_m) = \delta'(t - t' + |\boldsymbol{r} - \boldsymbol{r}'| / v_m)(-1). \tag{4.15}$$

Thus,

$$\frac{\partial g}{\partial z} = \frac{-1}{4\pi v_m |\boldsymbol{r} - \boldsymbol{r}'|} \frac{\partial}{\partial t'} \delta(t - t' + |\boldsymbol{r} - \boldsymbol{r}'| / v_m) \frac{d|\boldsymbol{r} - \boldsymbol{r}'|}{dz} + O\left(\frac{1}{|\boldsymbol{r} - \boldsymbol{r}'^2|} \right). \tag{4.16}$$

In some literature (Yilmaz [21]) the second order term $O(1/|\boldsymbol{r} - \boldsymbol{r}'|^2)$ is taken into account In this thesis only the first order approximation is utilized.

The $d|\boldsymbol{r} - \boldsymbol{r}'|/dz$ term can be re-written as

$$\frac{d|\boldsymbol{r} - \boldsymbol{r}'|}{dz} = \frac{z - z'}{|\boldsymbol{r} - \boldsymbol{r}'|} = \cos(\theta), \tag{4.17}$$

where we have shown the angle θ in Figure 4.2. Placing the approximation for g into (4.11) we arrive at:

$$\psi(\boldsymbol{r}, t) \approx \frac{1}{2\pi v_m} \int_{t'} \oint_{S'} \psi(\boldsymbol{r}', t') \frac{\partial}{\partial t'} \delta(t - t' + |\boldsymbol{r} - \boldsymbol{r}'| / v_m) \frac{\cos(\theta)}{|\boldsymbol{r} - \boldsymbol{r}'|} dS' dt' \ , \tag{4.18}$$

then utilizing the sifting property of the Dirac delta function:

$$\psi(\boldsymbol{r}, t) \approx \frac{1}{2\pi v_m} \oint_{S'} \frac{\partial}{\partial t'} \psi(\boldsymbol{r}', t + |\boldsymbol{r} - \boldsymbol{r}'| / v_m) \frac{\cos(\theta)}{|\boldsymbol{r} - \boldsymbol{r}'|} dS' \ . \tag{4.19}$$

Finally, the image is the wave field at time $t = 0$, so we may write

$$F_{KM}(x, y, z) = \frac{1}{2\pi v_m} \oint_{S'} \frac{\partial}{\partial t'} \psi(x', y', z' = 0, |\boldsymbol{r} - \boldsymbol{r}'| / v_m) \frac{\cos(\theta)}{|\boldsymbol{r} - \boldsymbol{r}'|} dS' \ . \tag{4.20}$$

The $|\boldsymbol{r} - \boldsymbol{r}'| / v_m$ term, once taken into the discrete domain, is exactly the same as the $2R_{j,k} / c_m$ term in Hyperbolic summation. Thus, KM consists in summing over theoretical hyperbolae (in time) in exactly the same manner as HS. However, there are three differences observed with these equations. The first is that we take into account the spreading losses of spherical waves in the $1 / |\boldsymbol{r} - \boldsymbol{r}'|$ term. Next is the $\cos(\theta)$ term, and the third is that we first take the derivative, in the time domain, of the received data. This means that we must calculate the time derivative of each A-scan before we perform the hyperbolic summation. In the frequency domain, this involves a simple multiplication of the data by $j\omega$.

All experimental data collected in this thesis was collected along a single line at discrete points y_k, $k = 1, 2, \ldots K$. The imaging equation for KM in this 2-D case becomes:

$$F_{KM}(y, z) = \frac{1}{2\pi v_m} \sum_{i=1}^{I} \frac{\partial}{\partial t'} \psi(y'_i, z' = 0, |\boldsymbol{r} - \boldsymbol{r}'| / v_m) \frac{\cos(\theta)}{|\boldsymbol{r} - \boldsymbol{r}'|} \ . \tag{4.21}$$

where $\boldsymbol{r}$ and $\boldsymbol{r}'$ are now in two dimensions.

In addition to our knowledge of the scalar wave field being discrete in y, our knowledge of the scalar wave field is discrete in time as well. Almost invariably the time $t = |\boldsymbol{r} - \boldsymbol{r}'| / v_m$ will not fall on an exact discrete time-domain data point. Thus, interpolation of some type is required for the implementation of this method. In this thesis, we have used simple nearest-neighbour interpolation to select the time-domain data point.

A graphical representation of the implementation of the algorithm is given in Figure 4.3.

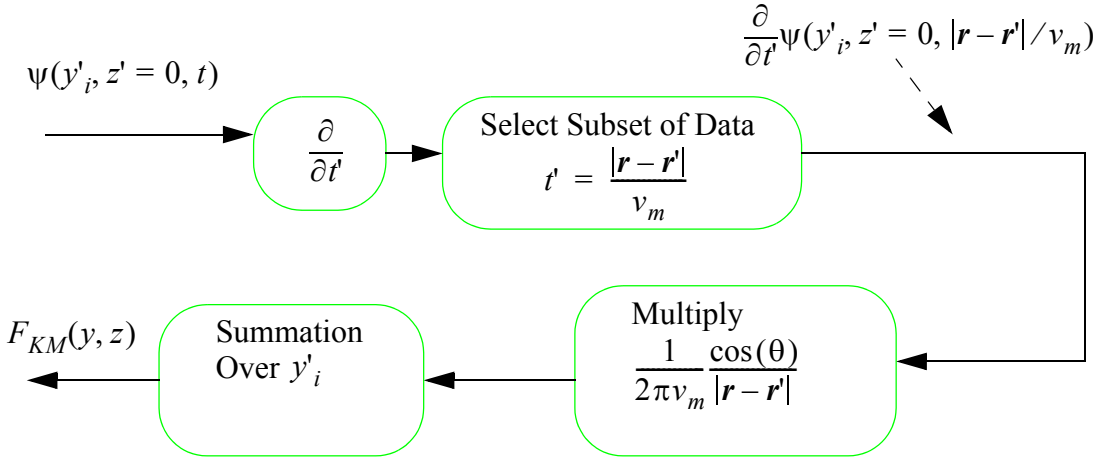

Figure 4.3: Graphical Representation of 2-D KM

4.4 Frequency-Wavenumber Migration

Frequency-Wavenumber (F-K), or Stolt Migration, was first developed by R.H. Stolt in 1979 [22]. It is also based on the exploding source model and the scalar wave equation. The final result closely resembles the final form of the Stripmap SAR algorithm. A thorough comparison of these two algorithms is completed in section 5.1.2. Also important is that F-K migration is theoretically identical to KM (see section 5.1.1). The F-K migration algorithm is presented in a sum of plane waves format.

F-K migration begins by considering a general plane wave of the form shown in (2.29). This plane wave obeys the time-domain scalar wave equation for lossless media:

$$\nabla^2\psi - \frac{1}{v_m{}^2}\frac{\partial^2\psi}{\partial t^2} = 0, \tag{4.22}$$

and the rectangular components of the vector wavenumber obey the separation equation,

$$k_x^2 + k_y^2 + k_z^2 = k^2 = \omega^2/v_m^2. \tag{4.23}$$

Accordingly, if we select any three of the components k_x, k_y, k_z or ω the fourth becomes fixed.

It has been shown (Stratton [9], p.363) that we can represent an arbitrary wave function $\psi(x, y, z, t)$ as a sum of plane waves:

$$\psi(x, y, z, t) = \left(\frac{1}{2\pi}\right)^{\frac{3}{2}} \int_{-\infty}^{\infty}\int_{-\infty}^{\infty}\int_{-\infty}^{\infty} P(k_x, k_y, \omega) e^{-j(k_x x + k_y y + k_z z) + j\omega t} dk_x dk_y d\omega , \qquad (4.24)$$

where $P(k_x, k_y, \omega)$ is an amplitude function of any three of the Fourier variables.

In GPR, we measure the field on the $z = 0$ plane: $\psi(x, y, 0, t) = p(x, y, t)$ and therefore we have

$$p(x, y, t) = \left(\frac{1}{2\pi}\right)^{\frac{3}{2}} \int_{-\infty}^{\infty}\int_{-\infty}^{\infty}\int_{-\infty}^{\infty} P(k_x, k_y, \omega) e^{-j(k_x x + k_y y) + j\omega t} dk_x dk_y d\omega . \qquad (4.25)$$

Noting that this is a FT (with a positive sign in the forward FT for spatial variables and a negative sign for time), we can determine the unknown amplitude function as

$$P(k_x, k_y, \omega) = \left(\frac{1}{2\pi}\right)^{\frac{3}{2}} \int_{-\infty}^{\infty}\int_{-\infty}^{\infty}\int_{-\infty}^{\infty} p(x, y, t) e^{j(k_x x + k_y y) - j\omega t} dx dy dt \ . \qquad (4.26)$$

Thus, $P(k_x, k_y, \omega)$ is simply the FT of the collected data, $p(x, y, t)$ in the k_x, k_y and ω domains.

Utilizing the basic concepts of the exploding source model, the image is $\psi(x, y, z, 0)$ and,

$$F_{FK}(x, y, z) = \psi(x, y, z, 0) = \left(\frac{1}{2\pi}\right)^{\frac{3}{2}} \int_{-\infty}^{\infty}\int_{-\infty}^{\infty}\int_{-\infty}^{\infty} P(k_x, k_y, \omega) e^{j(k_x x + k_y y + k_z z)} dk_x dk_y d\omega . \qquad (4.27)$$

Where we have placed a positive sign in the exponentail because the integrals are from $-\infty$ to ∞. This facilitates later comparisons to Stripmap SAR imaging.

This equation describes a focused image, however it is not in the convenient form of an IFT at this time. In order to eventually utilize the efficiency of the FFT algorithm, we make a change of variables from ω to k_z.

Noting from equation (4.23):

$$\omega = v_m \sqrt{k_x^2 + k_y^2 + k_z^2}, \tag{4.28}$$

then

$$\frac{d\omega}{dk_z} = \frac{v_m k_z}{\sqrt{k_x^2 + k_y^2 + k_z^2}}, \tag{4.29}$$

so

$$d\omega = \frac{k_z v_m^2}{\omega} dk_z. \tag{4.30}$$

The modified F-K imaging equation then becomes

$$F_{FK}(x, y, z) = \left(\frac{1}{2\pi}\right)^{\frac{3}{2}} \int_{-\infty}^{\infty} \int_{-\infty}^{\infty} \int_{-\infty}^{\infty} \frac{v_m^2 k_z}{\omega} P_o(k_x, k_y, k_z) e^{j(k_x x + k_y y + k_z z)} dk_x dk_y dk_z. \tag{4.31}$$

Where $P_o(k_x, k_y, k_z)$ is $P(k_x, k_y, \omega)$ mapped from the ω domain to the k_z domain. In this form our final image is represented as a FT, which when the imaging equation is formulated in discrete space and time allows us to utilize the efficient FFT. The final form of the F-K migration algorithm shows us that to obtain a focused image, we take the 3-D FT of the collected data in the k_x, k_y and k_z domains (i.e. $P_o(k_x, k_y, k_z)$) scaled by the Jacobian of the transformation from ω to k_z, $v_m^2 k_z / \omega$.

This equation can be re-derived for two spatial dimensions. In two dimensions (y, z), the separation equation (4.23) becomes

$$k_y^2 + k_z^2 = \frac{\omega^2}{v_m^2}, \tag{4.32}$$

and the final imaging equation becomes

$$F_{FK}(y, z) = \left(\frac{1}{2\pi}\right) \int_{-\infty}^{\infty} \int_{-\infty}^{\infty} \frac{v_m^2 k_z}{\omega} P_o(k_y, k_z) e^{j(k_y y + k_z z)} dk_y dk_z. \tag{4.33}$$

Written in this form, we can more closely see the resemblance of F-K migration to Stripmap SAR. In fact, the only difference in the final imaging equations is the Jacobian term, $v_m^2 k_z / \omega$. The nature of these similarities is described fully in 5.1.2.

When F-K migration is taken into the discrete domain, the switch from ω to k_z creates exactly the same interpolation problem as in Stripmap SAR. Again, we collect data at a set of evenly spaced discrete points in the y-k_y domains, and a set of evenly spaced discrete points in the t-ω domains. When we map the data from the from the ω domain to the k_z we utilize the equation:

$$k_z = \sqrt{\frac{\omega^2}{v_m^2} - k_y^2}, \tag{4.34}$$

which, when we consider that $v_m = c_m/2$, becomes

$$k_z = \sqrt{\frac{4\omega^2}{c_m^2} - k_y^2}. \tag{4.35}$$

This mapping equation is equivalent to equation (3.19), the mapping equation from Stripmap SAR imaging. Again, the interpolation problem is further described in Appendix A

A graphical representation of the 2-D F-K algorithm is given in Figure 4.4.

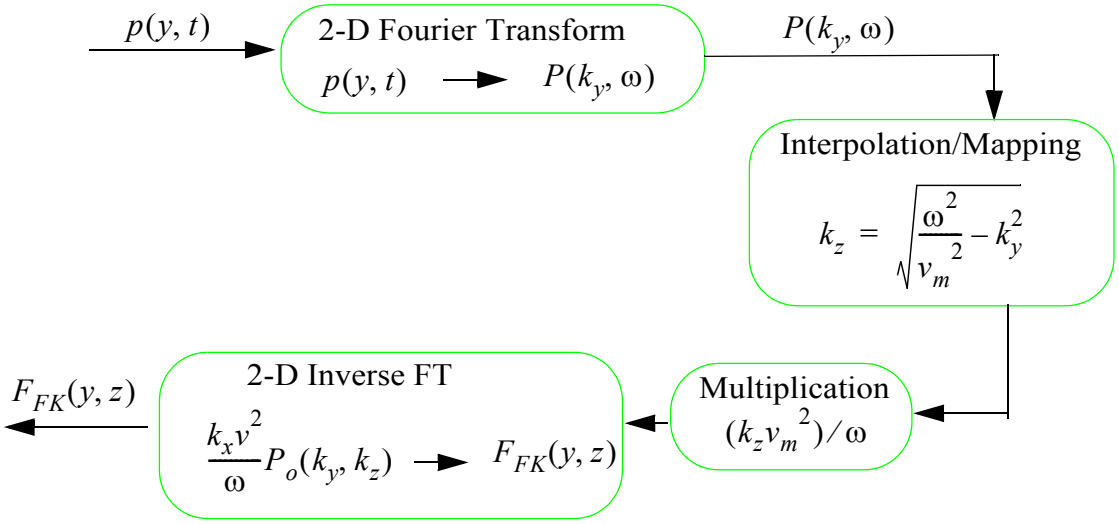

Figure 4.4: Graphical Representation of the 2-D Frequency- Wavenumber Migration

Chapter 5

Comparison of Imaging Techniques

In this Chapter, we first prove that KM and F-K migration are theoretically equivalent. We also show why the final equations for Stripmap SAR and F-K migration are so similar, utilizing the sum of plane waves interpretation of both techniques. The practical implementation of the algorithms is also shown. Next, we give a brief discussion of the experimental set-up used to collect the experimental data, and then give results for both synthetic and experimental data.

The main contribution of Part I of this thesis lies in this section. The Stripmap SAR and Seismic migration are often treated as distinct in the literature; for example the major textbooks used for references for Stripmap SAR (Soumekh [6]) and Seismic Migration (Zhdanov [5]), do not make any mention of the other techniques, despite the similarities. These similarities are discussed in section 5.1.2. In addition, it is not well understood within the EM community that Kirchhoff and Frequency-Wavenumber migration are equivalent (e.g. Scheers [18]).

5.1 Theoretical Comparisons of Different Focusing Algorithms

5.1.1 The Equivalence of Kirchhoff Migration and Frequency-Wavenumber Migration

While the basic imaging equations of KM (equation (4.11)) and F-K migration (equation (4.31)) look dissimilar, they both derive from the scalar wave equation (4.3) with velocity v_m. It should come as no surprise that they are equivalent from a theoretical

perspective. There are, of course, differences in implementation and in the nature of the approximation of the derivative of the Green's Function in KM.

To show the equivalence of KM and F-K migration, we must first write the KM solution for the scalar wave field (equation (4.11)) in the frequency domain. In the frequency domain, (4.11) becomes (Zhdanov [5])

$$\Psi(\boldsymbol{r}, \omega) = -2\frac{\partial}{\partial z}\oint_{S'}\Psi(\boldsymbol{r}', \omega)g^{*}_{\omega}(\boldsymbol{r}, \omega|\boldsymbol{r}', \omega)dS', \tag{5.1}$$

where * denotes complex conjugate, and

$$g_{\omega}(\boldsymbol{r}, \omega|\boldsymbol{r}', \omega) = \frac{1}{4\pi|\boldsymbol{r}-\boldsymbol{r}'|}e^{-j\omega\frac{|\boldsymbol{r}-\boldsymbol{r}'|}{v_m}}, \tag{5.2}$$

is the frequency domain Green's function for the scalar wave equation.

Another important part of proving the equivalence of KM and F-K migration is writing equation (4.24) in the frequency domain. In the frequency domain, (4.24) becomes:

$$\Psi(x, y, z, \omega) = \left(\frac{1}{2\pi}\right)\int_{-\infty}^{\infty}\int_{-\infty}^{\infty}P(k_x, k_y, \omega)e^{j(k_x x + k_y y + k_z z)}dk_x dk_y. \tag{5.3}$$

We will now show that the two frequency domain solutions of the scalar wave field, (5.1) and (5.3) are equivalent.

We can demonstrate that, in $z > 0$,

$$e^{jk_z z} = -2\frac{\partial}{\partial z}\tilde{g}^{*}_{\omega}(z;\omega, k_x, k_y), \tag{5.4}$$

where

$$\tilde{g}_{\omega}(z;\omega, k_x, k_y) = \left(\frac{1}{2\pi}\right)\int_{-\infty}^{\infty}\int_{-\infty}^{\infty}g_{\omega}(x, y, z;\omega)e^{-j(k_x x + k_y y)}dxdy, \tag{5.5}$$

and

$$g_{\omega}(x, y, z;\omega) = g_{\omega}(\boldsymbol{r};\omega) = \frac{1}{4\pi|\boldsymbol{r}|}e^{-j\omega\frac{\boldsymbol{r}}{c}} \tag{5.6}$$

is the Green's function of the Helmholtz equation. It can be shown (Zhdanov [5]) that the function $\tilde{g}_{\omega}(z;\omega, k_x, k_y)$ satisfies the 1-D Helmholtz equation,

$$\left(\frac{\partial^2}{\partial z^2} + k_z^2\right)\tilde{g}_\omega(z;\omega, k_x, k_y) = -\delta(z). \tag{5.7}$$

Therefore, $\tilde{g}_\omega(z;\omega, k_x, k_y)$ is the Green's Function for the 1-D Helmholtz equation (where we may apply the term Helmholtz because we have assumed that the velocity in the Helmholz equation is one, i.e $c = 1$). The solution to this equation is [5]

$$\tilde{g}_\omega(z;\omega, k_x, k_y) = -\frac{1}{2jk_z}e^{-jk_z|z|}. \tag{5.8}$$

For $z > 0$,

$$\frac{\partial}{\partial z}\tilde{g}^*_\omega(z;\omega, k_x, k_y) = -\frac{1}{2}e^{jk_z z} \quad . \tag{5.9}$$

Which is (5.4). Placing (5.4) into the frequency domain representation of the sum of plane waves solution for F-K migration (equation (5.3)) we arrive at:

$$\Psi(x, y, z, \omega) = -2\left(\frac{1}{2\pi}\right)\int_{-\infty}^{\infty}\int_{-\infty}^{\infty} P(k_x, k_y, \omega)\frac{\partial}{\partial z}\tilde{g}^*_\omega(z;\omega, k_x, k_y)e^{j(k_x x + k_y y)}dk_x dk_y \ . \tag{5.10}$$

Utilizing the fact that the FT of the product of two functions is equal to the convolution of these two functions, we obtain

$$\Psi(\boldsymbol{r}, \omega) = -2\frac{\partial}{\partial z}\oint_S \Psi(\boldsymbol{r}', \omega)g^*_\omega(\boldsymbol{r}, \omega|\boldsymbol{r}', \omega)dS', \tag{5.11}$$

which is equation (5.1), the frequency domain representation of the KM solution of the scalar wave equation. Therefore, from a theoretical perspective, we have that the two solutions are equivalent. Differences that do occur between the two algorithms come when we implement the two algorithms.

5.1.2 Similarities and Differences of F-K Migration and Stripmap SAR

The key to comparing these two algorithms is the sum of plane waves solution interpretation of both. To the authors knowledge, neither algorithm has been previously presented in this form. The real differences between these two algorithms lies in the method of finding the image equations, not the initial assumptions of the models.

Given that initial modelling equation (3.13) of Stripmap SAR was shown to be equivalent to a plane wave expansion of the received field in section 3.4.3, we can see that the sum of plane waves method used to solve for the F-K migration image could be used with the Stripmap SAR equation as the known portion of the scalar wave field. That is, we could now let the initial Stripmap SAR equation (3.13) be our known scalar field at $z = 0$, That is, for the 2-D version of F-K migration, let $\psi(y, z = 0, t) = s(y, t)$ and solve for the total field following the procedure used for F-K migration (section 4.4).

The real differences lie in the method of selecting what we called the 'desired image'. Once the initial model of Stripmap SAR is given, we derive the final imaging equation by comparison with an 'ideal image' consisting of Dirac delta functions, where in F-K migration we define the desired image as the backward extrapolated wave field at time $t = 0$.

Also of interest is to note that the Stripmap SAR initial modelling equation ignores the 3-D spreading loss term $1/R$. F-K migration, as a rigorous solution of the scalar wave equation, does take this spreading loss into account.

The Stripmap SAR algorithm is not a rigorous solution of the scalar wave equation, it is a solution of the particular model selected. Due to the fact that the F-K migration is a rigorous solution and clealy states the approximations used (in the exploding source model), we consider it a superior algorithm for pedagogical purposes. In section 5.4 we will show that the practical differences between the two algorithms are slight.

5.2 Practical Implementation of Imaging Algorithms

While Stripmap SAR, KM migration and F-K migration algorithms have all been developed, it remains to be shown how they were practically implemented (i.e. computational implementation). Here, we show the three imaging algorithms in flow chart form.

All synthetic and experimental data considered comes from a Stepped-Frequency Continous Wave (SFCW) radar which is moved along a single line, as shown in Figure 1.2. With a SFCW radar data is collected in the frequency domain. As such, we assume for

this section that we have knowledge of a scalar wave field along the $z = 0$ axis at a set of discrete points in both y and ω. We denote this field

$$\Psi(y_a, z = 0, \omega_b) = \Psi(y_a, \omega_b) \tag{5.12}$$

where $y_a = a\Delta y$, $a = 0, 1, \ldots, A-1$ and $\omega_b = b\Delta\omega$, $b = 0, 1, \ldots, B-1$. The values of B, A, Δy and $\Delta\omega$ depend on the particular data set collected.

We also assume that we have generated the full frequency domain response (i.e. we have negative and positive frequency data). When the data is not in this form (i.e. it is collected from an SFCW radar), it should be appropriately zero-padded and the negative frequency data generated as described in section 2.5.2 for the following flow charts to be applicable.

5.2.1 B-Scans

A B-scan consists of taking the FFT of the collected data in the ω direction, then scaling the resulting time axis using the equation $z = v_m t$. The flow chart is shown in Figure 5.1. The B-scan results in an unfocused image. Matlab code for the implementation

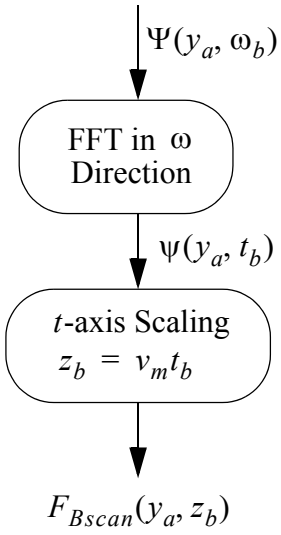

Figure 5.1: Implementation of a B-scan

of B-scans is given in Appendix B.

In GPR for landmine detection, we are often only interested in a small range of data, e.g., $0 < z < 0.5$ (meters). As such, we often display only a portion of the total image, $F_{Bscan}(y_a, z_b)$, by displaying a selected set of values of z_b.

5.2.2 Stripmap SAR/F-K Migration

The implementation of Stripmap SAR and F-K migration are very similar. The only difference from an implementation point of view is that a different multiplication is required before the final 2-D IFFT. For quick reference, the (continous variable) imaging equation for Stripmap SAR with the data in the form of (5.12) is

$$F_{SAR}(y, z) = \frac{1}{2\pi} \int_{-\infty}^{\infty} \int_{-\infty}^{\infty} \frac{\Psi(k_y, k_z)}{P(\omega)} e^{j(k_y y + k_z z)} dk_y dk_z, \tag{5.13}$$

and the imaging equation for F-K migration is

$$F_{FK}(y, z) = \frac{1}{2\pi} \int_{-\infty}^{\infty} \int_{-\infty}^{\infty} \frac{v_m^2 k_z}{\omega} \Psi(k_y, k_z) e^{j(k_y y + k_z z)} dk_y dk_z. \tag{5.14}$$

The flow chart is shown in Figure 5.2. Details of the interpolation procedure are

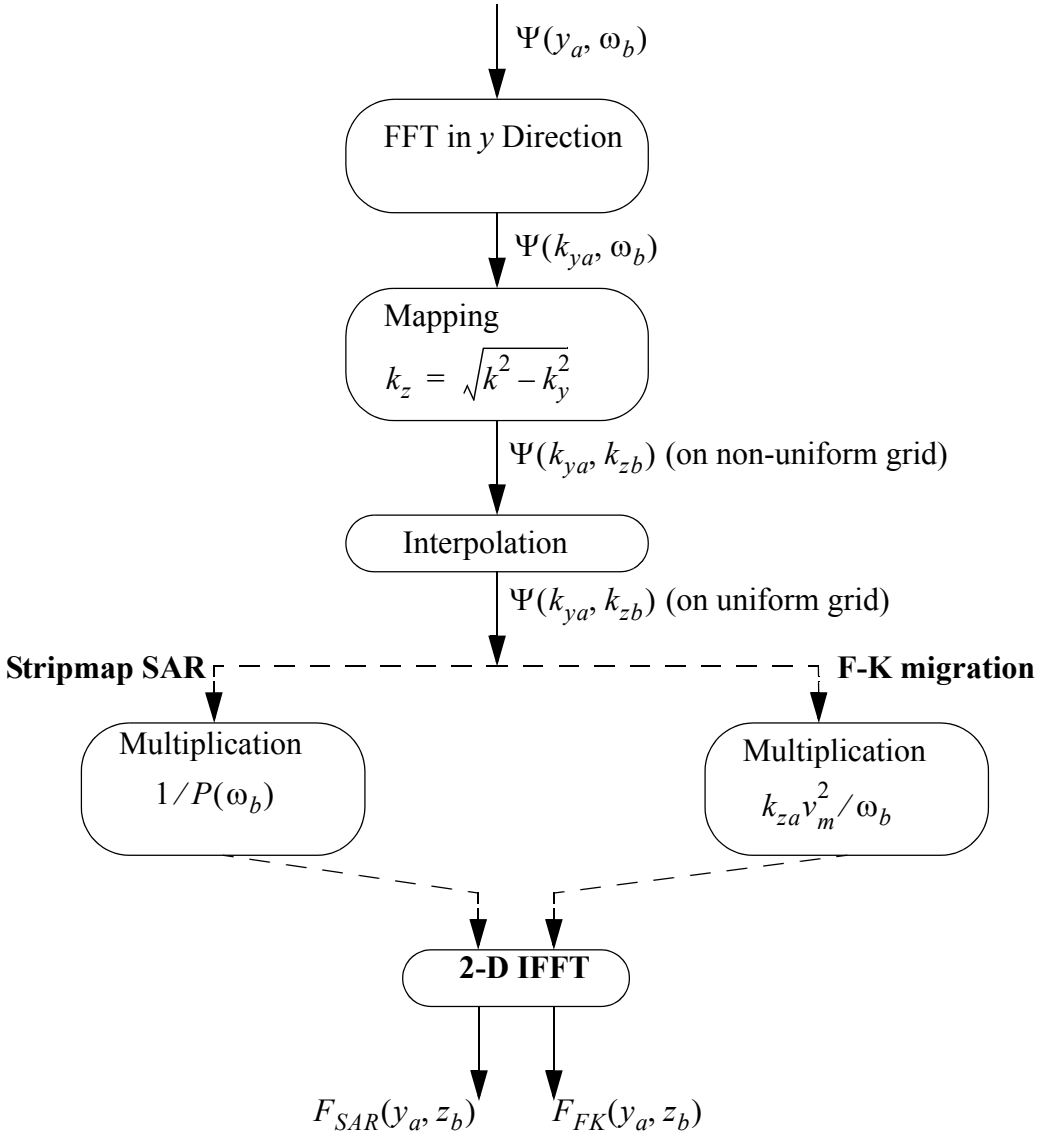

Figure 5.2: Practical Implementation of Stripmap SAR and F-K Migration Flow Chart

found in Appendix A, and Matlab code for the implementation of this flow chart is shown in Appendix B.

Again, because we are often interested in a small depth of targets, we often only display a selected portion of the image, e.g. $0 < z_b < 0.5$.

5.2.3 Kirchhoff Migration

Here, we give the flow chart for the implementation of KM. Due to the fact that we can select which points we want to migrate, we save significant computational time by selecting a sub-region over which to migrate. Here, we select, for example, the region $0 < z_b < 0.5$ before we perform the full KM migration.

The KM equation for the SFCW radar data is given by:

$$F_{KM}(y,z) = \frac{1}{2\pi v_m}\sum_{a=1}^{A}\frac{\partial}{\partial t'}\psi(y'_a, z'=0,\ t'_b = |\boldsymbol{r}-\boldsymbol{r}'|/v_m)\frac{\cos(\theta)}{|\boldsymbol{r}-\boldsymbol{r}'|}. \qquad (5.15)$$

The KM flow chart is shown in Figure 5.3

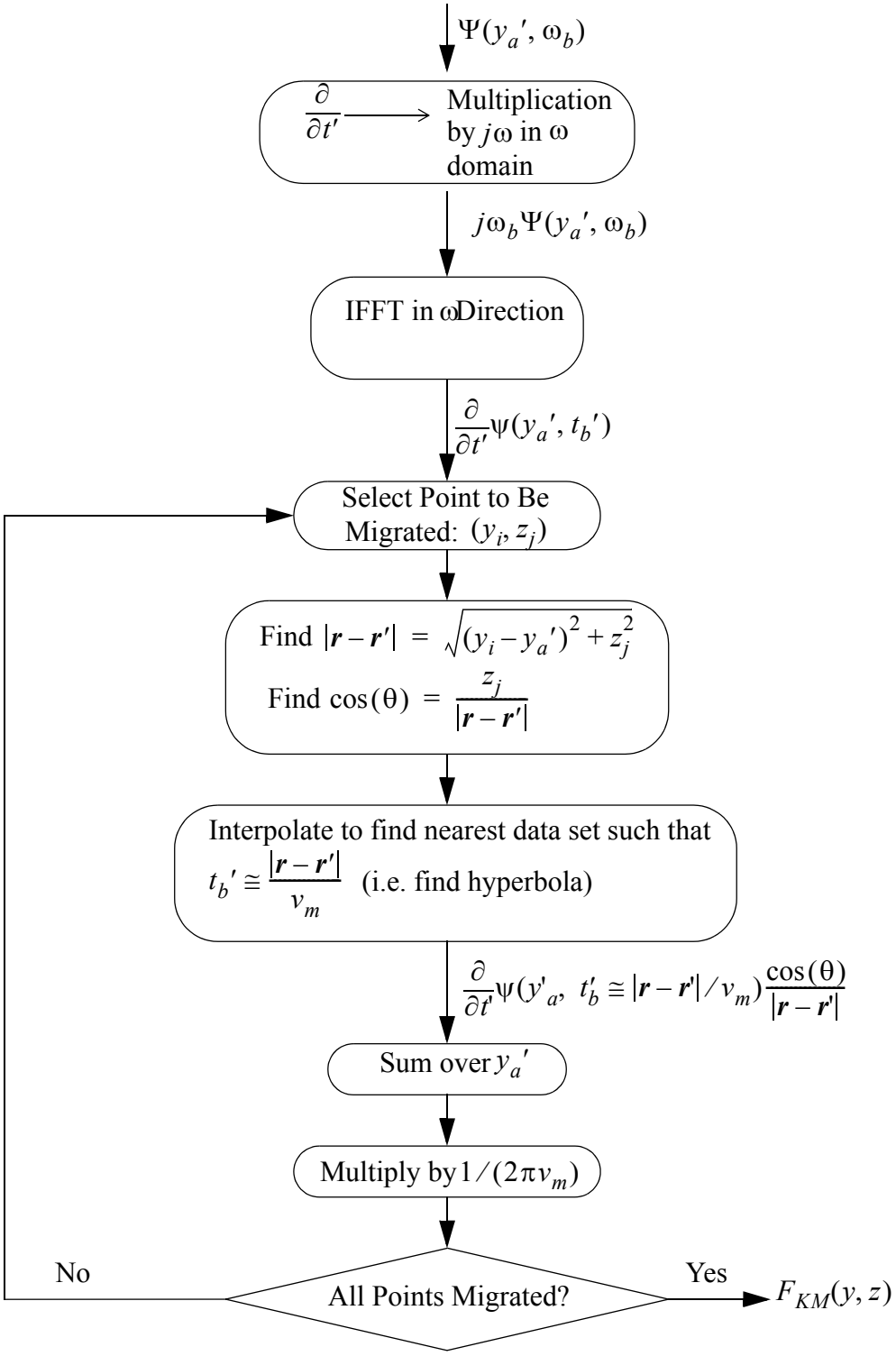

Figure 5.3:Practical Implementation of KM Flow Chart

Here, instead of migrating the whole image then selecting a sub-portion to display, we may migrate only the part of the image we wish to display by properly selecting the points we wish to migrate.

The Matlab code for the KM algorithm is given in Appendix B.

5.3 Experimental Setup

In this section we describe how both synthetic and experimental data were generated. All data comes from SFCW radar (simulated or experimental).

5.3.1 Synthetic Data Generation

To simulate data coming from a point target, the following equation is used:

$$B(y, \omega) = \sum_{i=1}^{N} \frac{\sigma_i F(\theta)}{(2R_i)^2} e^{j2\pi f \frac{2R_i}{c_m}}, \tag{5.16}$$

where σ_i is the reflectivity, R_i is the distance from the ith target to the antenna position, $F(\theta) = (\cos(\theta))^2$ is a simulated antenna radiation pattern, f is the frequency of excitation, and c_m is the velocity of the medium. The total number of point targets is N.

The purpose of the synthetic data is to ensure that the implementations of the focusing algorithms are working. As such, there is no ground-air interface simulated in the data: we assume a homogenous medium with material parameters ε_1, μ_1 and $\sigma = 0$ (i.e. conductivity is zero. Due to the fact that the synthetic data closely represents our initial assumptions of the exploding source model which is applied to the focusing algorithms, we expect the algorithms to perform well with this data.

5.3.2 Experimental Data

The general experimental set-up is shown in Figure 5.4.

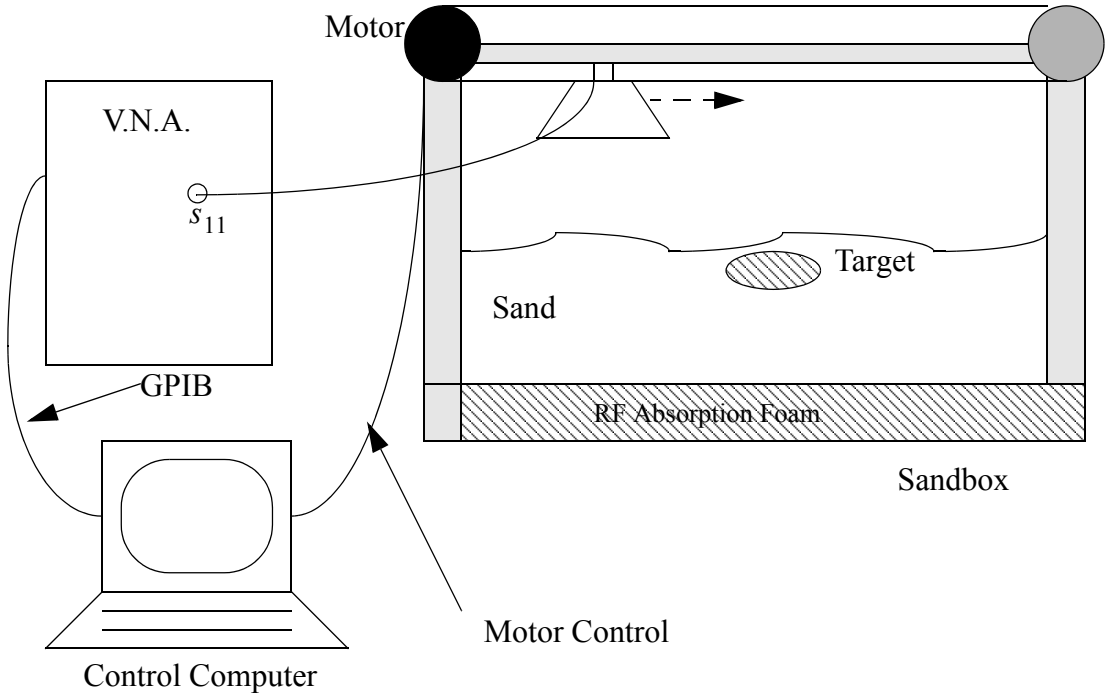

Figure 5.4: Experimental Setup

Here, an Anritsu 360 B Vector Network Analyzer (VNA) is used to collect s_{11} data from a single antenna (monostatic radar). The VNA is controlled over a General Purpose Instrumentation Bus (GPIB) via ethernet using a National Instruments GPIB-Ethernet Adapter. The computer also controls a motor that moves the single antenna along a set of rails suspended above the sandbox. This setup allows for movement along a single line with a controllable step size. A photograph of the sandbox (with a horn antenna) is shown in Figure 5.5.

The sandbox was filled with dry silica sand, with $\varepsilon_r \approx 2.2$. For the purposes of the imaging algorithms, we assumed $\sigma = 0$. Here, we have also placed blocks of RF absorp-

Figure 5.5: Photograph of Experimental Setup

tion foam beneath the sand.

5.4 Results

All three major algorithms, Stripmap SAR, KM and F-K migration were programmed in Matlab. All algorithms were implemented in 2-D format.

5.4.1 Synthetic Data Results

First, the algorithms were compared by imaging synthetic data. The unfocused B-scan image of the synthetic data is shown in Figure 5.6. Here we have created the data

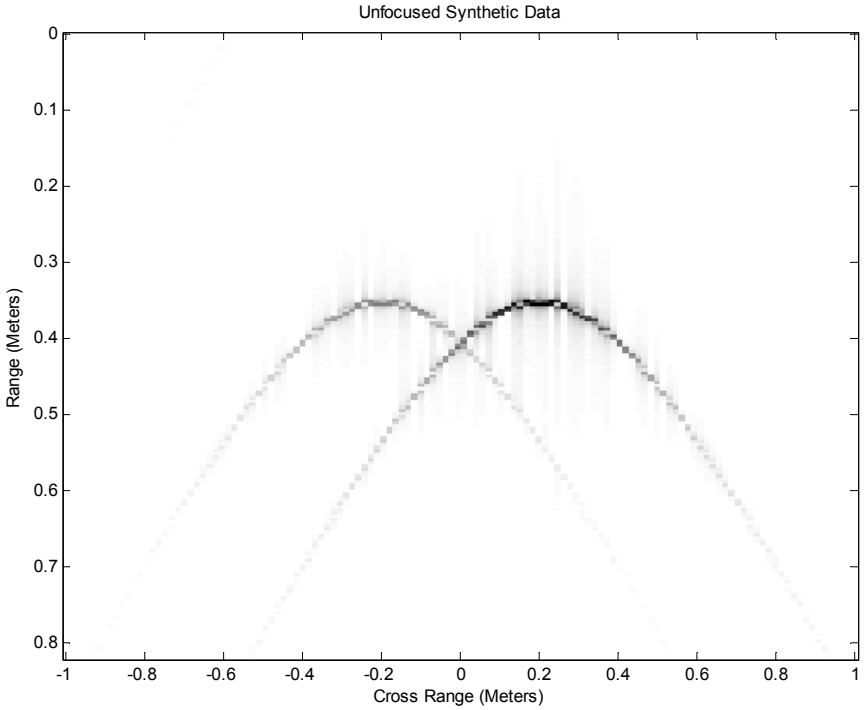

Figure 5.6: Unfocused Synthetic Data for Two Point Targets

using the method described in section 5.3.1, with the medium parameters $\varepsilon_r = 2.2$, $\mu_r = 1$, and $\sigma = 0$. There are two point targets located at $(y_1, z_1) = (-0.2, 0.35)$ and $(y_2, z_2) = (0.2, 0.35)$ with reflectivities 0.5 and 1 respectively. The data was collected with a step size in the cross range of 1 cm, over a simulated frequency range of 1-12.4 GHz. The discretized target hyperbolas can clearly be seen. However these hyperbolas are not perfect (i.e there is some distortion), so we expect imperfections in the focused images.

Next, we present the focused image of the data using the Stripmap SAR algorithm. This is shown in Figure 5.7. The target hyperbolas have been focused. The next figure,

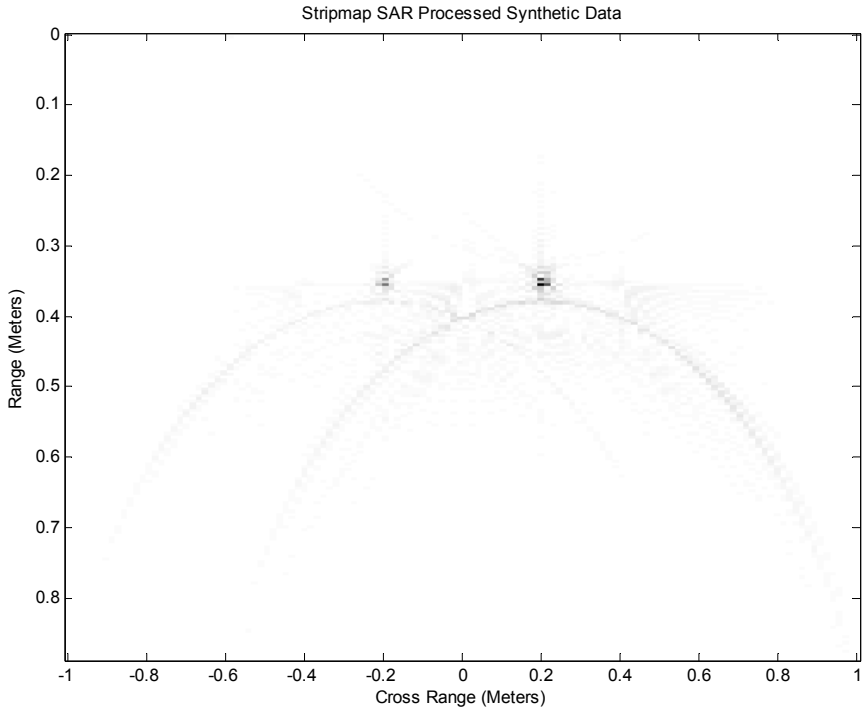

Figure 5.7: Stripmap SAR Focused Synthetic Data for Two Point Targets

Figure 5.8, is the F-K migrated image, and the KM image is shown in Figure 5.9. All

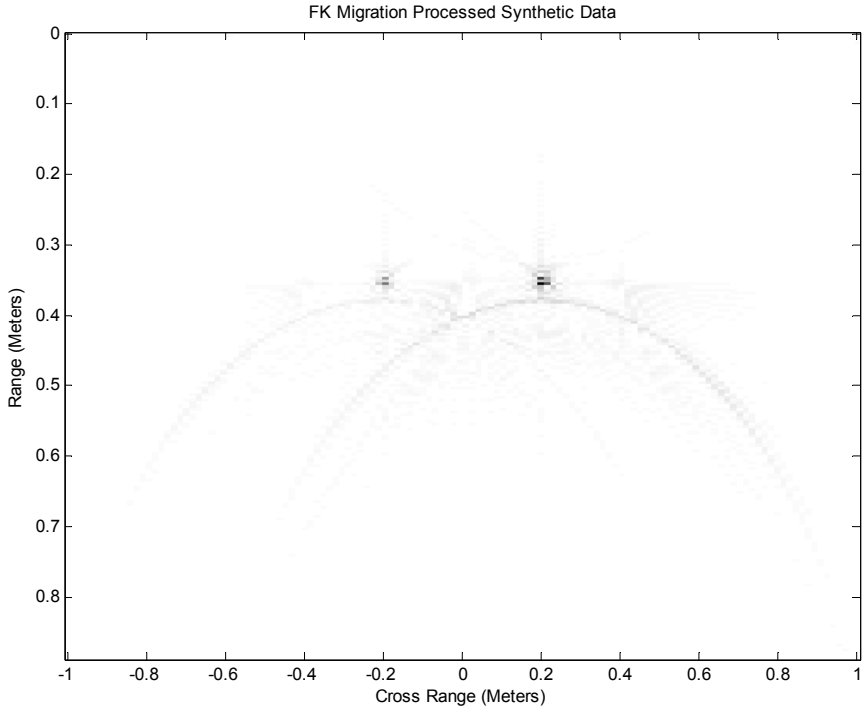

Figure 5.8: F-K Migration Focused Synthetic Data for Two Point Targets

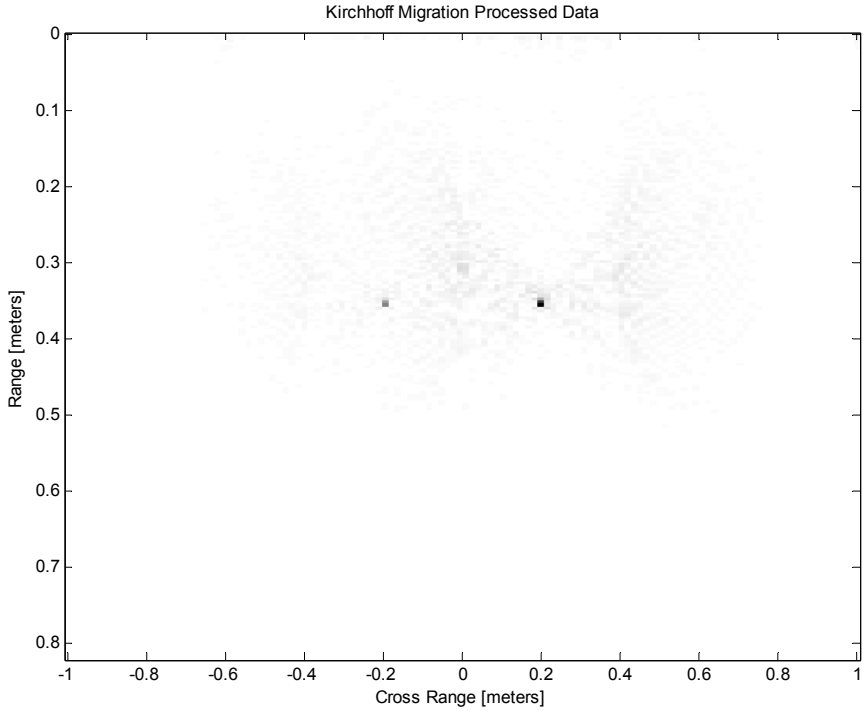

Figure 5.9: KM Focused Synthetic Data for Two Point Targets

images have been normalized so that the maximum magnitude is one. In addition, we have selected a viewing range of $0 < z < 0.9$ meters.

Subjectively, we might say that KM focuses the image slightly better than the other two algorithms. The error in the focusing does not appear in the form of a residual hyperbola, which occur in the Stripmap SAR and F-K images. It is unclear where these ghost hyperoloid images come from at this time. We do not expect ideal focusing, as the algorithms were derived for the case of continous data over the whole y axis, and we clearly do not have this situation.

One of the advantages of using synthetic data is that we can define the ideal image as a single pixel at location $(y_1, z_1) = (-0.2, 0.35)$ of magnitude 0.5 and a pixel at location $(y_2, z_2) = (0.2, 0.35)$ with magnitude 1. Utilizing this ideal image, we can now calculate the RMS error between the ideal image and the three focusing algorithms defined as:

$$E_{RMS} = \sqrt{\sum_{a=0}^{A-1} \sum_{b=0}^{J-1} \left(F_{ideal}(y_a, z_b) - F_{focused}(y_a, z_b)\right)^2} \quad . \tag{5.17}$$

where $J-1$ is the index of the largest z_b in the displayed image. For the three figures above, this would be $z_{J-1} = 0.9$. The RMS error will vary depending on the selection of $J-1$. Note that A and J can be selected to change the range over which the RMS error is calculated, but it is important to select the same number of pixels from each image to ensure proper comparison. The RMS error for the three images is shown in Table 5.1.

Other metrics were attempted, such as entropy. However, it provided similar results to the RMS error metric (with even less difference between images than RMS error). Essentially, the error metrics are close for all three images.

As another algorithm metric we have presented the time required to complete each focusing algorithm. While no claim to the most efficient implementation of these algorithms is made, (especially KM) the results seen in Table 1 are instructive.

While all three RMS errors are similar, the time to process is very different. We can conclude from visual inspection and the RMS error that all three algorithms focus images comparably, but KM shows over a two magnitude increase in computation time over the

more efficient FFT-based Stripmap SAR and F-K methods. The slight improvement in RMS error does not justify the huge amount of processing time required to complete the focusing of KM.

Table 5.1 Comparison of Focusing Algorithms for Synthetic Data

Focusing Algorithm	Time Required to Process Image (Seconds)	RMS Error
Stripmap SAR	1	2.76
Frequency-Wavenumber Migration	1	2.69
Kirchhoff Migration	546	2.37

5.4.2 Experimental Results

Experimental data is obtained using a monostatic setup with a Vivaldi patch antenna and the VNA from 0.8 to 5 GHz. The targets consist of, from right to left, two mine-like dielectric targets, a small piece of wood, and a small (shrapnel-like) metallic target. A dia-

gram of the targets is shown in Figure 5.10. The first dielectric target consists of a 5x12x2

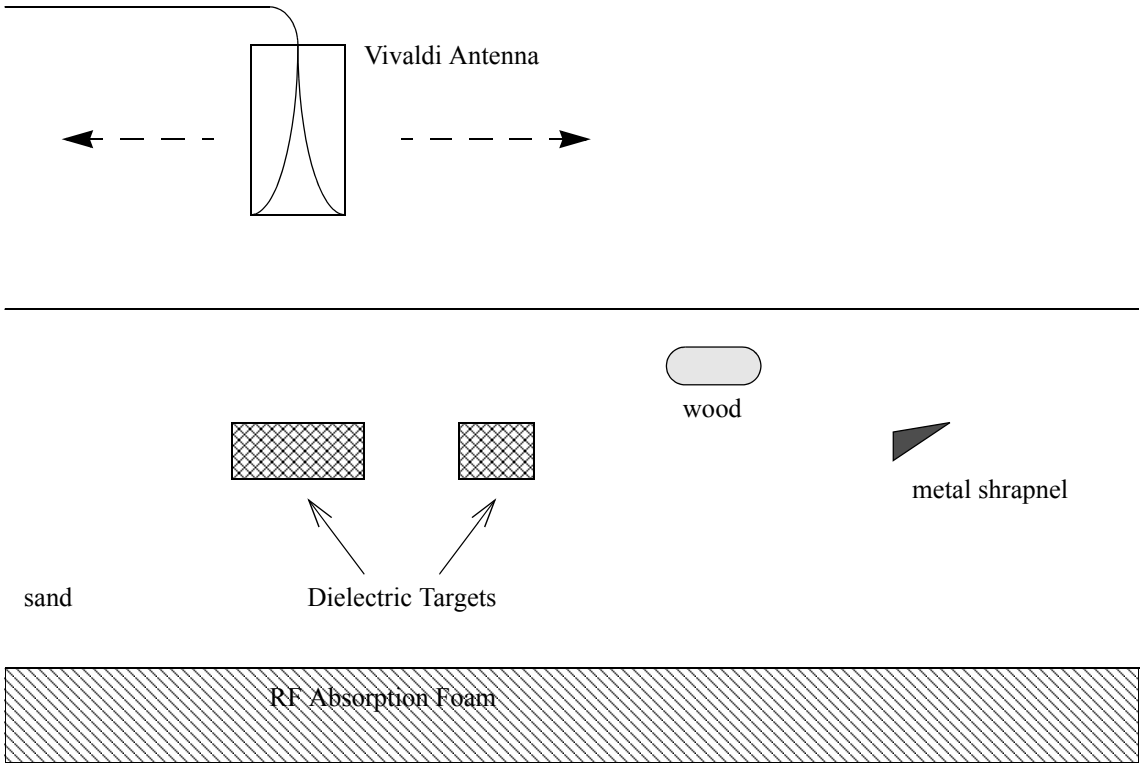

Figure 5.10: Experimental Data Layout

cm foam block, while the second dielectric target consists of cylindrical shaped foam with a depth of 2 cm and a diameter of 8 cm. The piece of wood is a 5x3x6 cm piece of spruce, and the metallic target is a small piece of sheet metal with a maximum dimension of less than 12 cm.

As the purpose of this section is to compare the image focusing algorithms, a particular set of targets is not the main consideration. It is important that the GPR is able to detect both metallic and dielectric targets in the sand, but this detection ability is a factor of the antenna, transmit/receive system, and the material parameters of the targets involved. It has been shown previously (e.g. Phelan [27]) that detection of these types of targets is feasible with this particular experimental setup.

Data was collected at a 1 cm step size in the cross range. Here, the ground surface has been windowed out of the image to enhance the relative magnitude of the targets. The

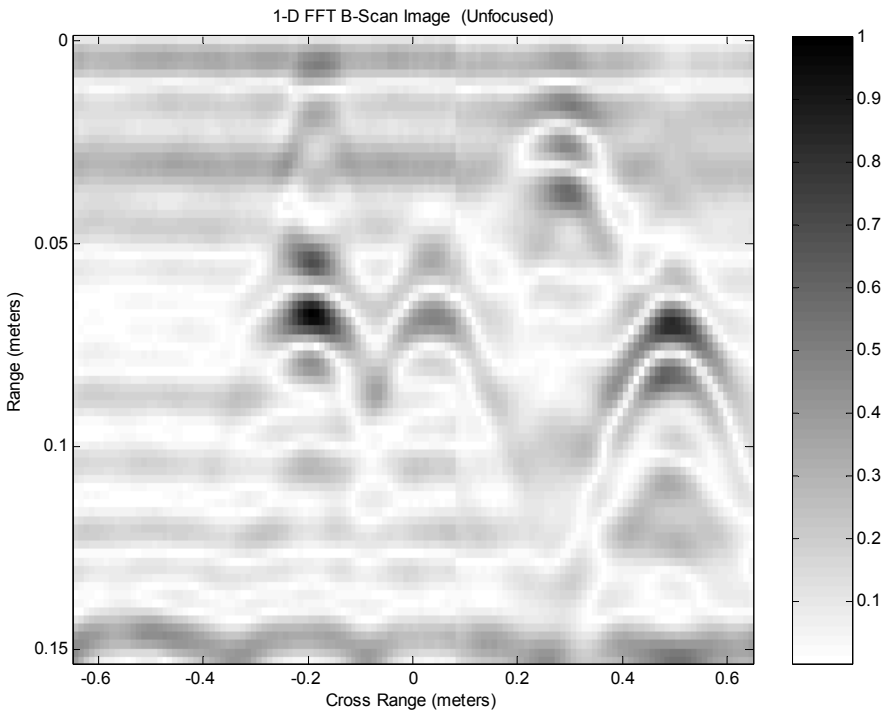

Figure 5.11: Unfocused Data for 0.8-5GHz SFCW Radar

unfocused image is presented in Figure 5.11. All images in this section have been normal-

ized magnitude of one. The Stripmap SAR focused image is shown in Figure 5.12 The F-

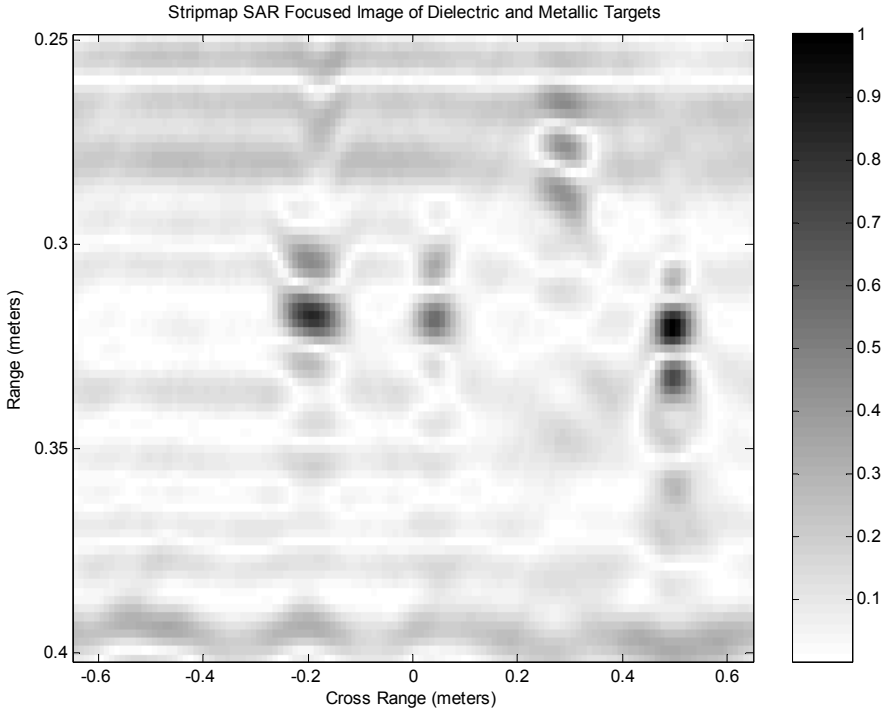

Figure 5.12: Stripmap SAR Focused Image for 0.8-5GHz SFCW Radar

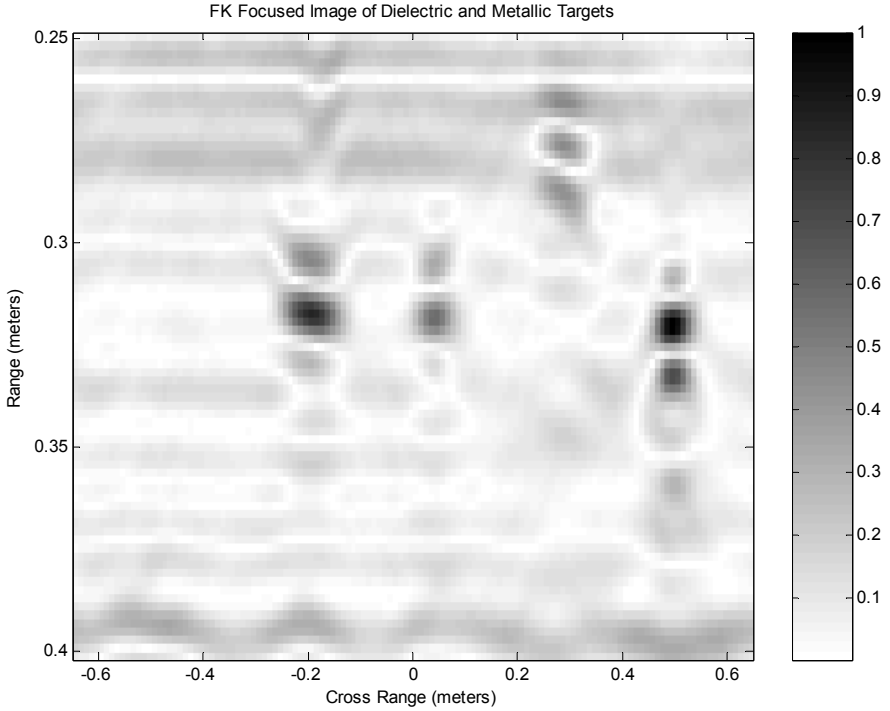

Figure 5.13: F-K Migration Focused Image for 0.8-5GHz SFCW Radar

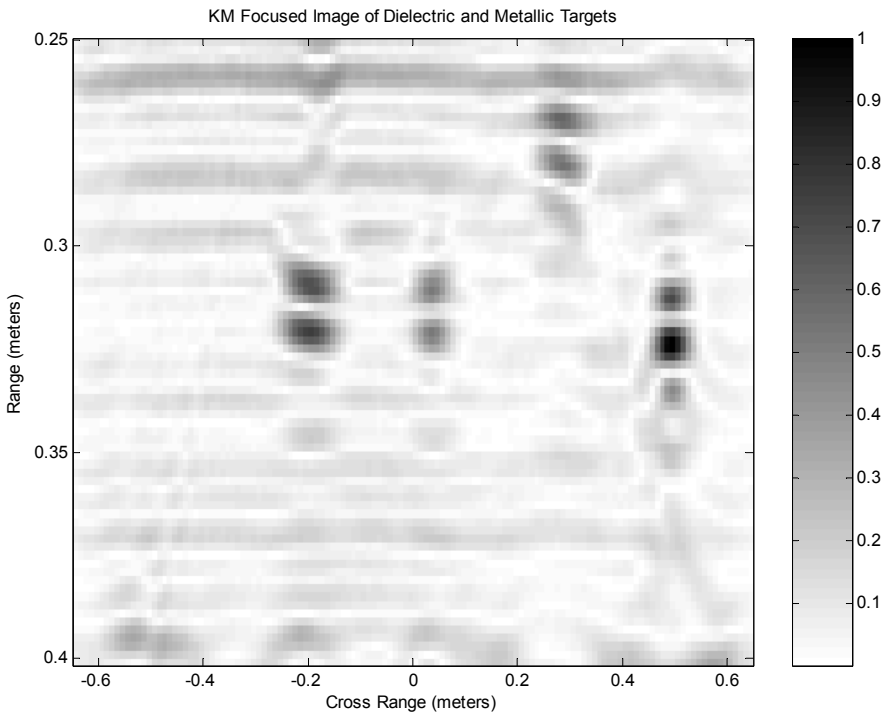

Figure 5.14: KM Focused Image for 0.8-5GHz SFCW Radar

K focused image is shown in Figure 5.13. The KM focused image is shown in Figure 5.14.

As can been seen all three focused images provide a reasonable focusing of the unfocused radar data. All three focused images are visually very similar, with some slight differences in KM. While not shown here, KM again took over two orders of magnitude longer than the FFT based algorithms. Obviously, KM has high computational demands with little or no gain in image quality.

To help determine the differences between Stripmap SAR and F-K migration, which are not visible to the eye, a plot of the difference between the Stripmap SAR image in Figure 5.12 and the F-K image in Figure 5.13 was computed. This plot is shown in Fig-

ure 5.15. We note that the maximum magnitude difference is of 1.6% of the maximum

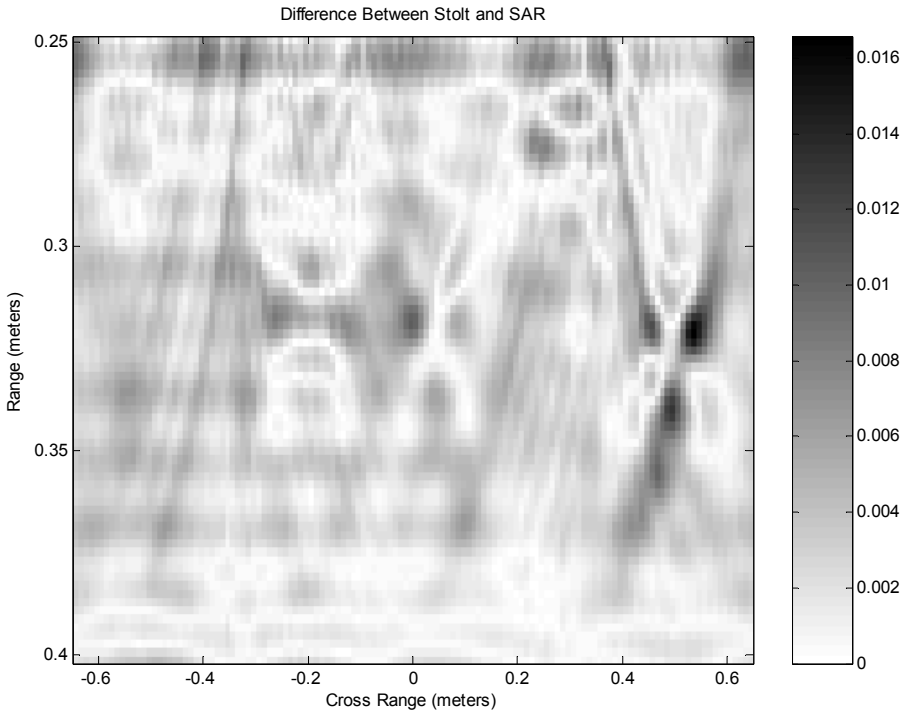

Figure 5.15: Difference Between Stripmap SAR and F-K Focused Images for 0.8-5GHz SFCW Radar

magnitude of the two regular images. This, combined with the very similar results of Figure 5.12 and Figure 5.13 allows us to conclude that the differences in the multiplicative constant taken before the final 2-D IFFT (see Figure 5.2) makes little practical difference at these frequencies. The effects may be different for alternate frequency ranges.

5.5 Conclusions and Future Work of Part I

We have shown how various migration and SAR algorithms, which can be applied to GPR imaging of landmines, are developed, and shown the similarities and differences both from a theoretical and experimental point of view. Images formed by these algorithms show little subjective difference. The main difference is compuational time and it was shown that Stripmap SAR and F-K migration are much more computationally efficient than KM. Confusion around the close relationship between Stripmap SAR and F-K algorithms was alleviated by using a sum of plane wave interpretation of both techniques.

While this investigation shows how imaging algorithms may be applied to GPR data to focus images into slightly better focused images which can aid in target detection, these forms of inverse imaging do not provide an adequate method to identify/discriminate landmine targets. For example, in the experimental data presented above, we cannot discriminate the two mine-like dielectric targets from either the wood ‘clutter’ or metallic (shrapnel) ‘clutter’. We can see where possible targets exist, but we cannot determine the nature of those targets. Clearly, other methods will be required to properly identify land mine like targets from surrounding clutter. The exploration of the Singularity Expansion Method as a solution to the identification problem is the subject of Part II of this thesis.

5.5.1 Future Work

For the purposes of aiding in the detection of landmine targets, it seems that these focusing algorithms are sufficient at this time. While other imaging algorithms do exist (see, for example, Milisavljevic [23]), the larger problem seems not to be in the detection, but rather identification of subsurface targets. As such, our efforts are now focusing on target identification.

Part II

A Preliminary Investigation into the use of the Singularity Expansion Method for Identification of Buried Objects

Chapter 6

Introduction to Part II

Using the methods described in part I of this thesis, we are able to construct subsurface images of objects which have different electromagnetic properties than the surrounding medium. These images allow for the detection of buried objects, but give very little help in identifying the target (other than some idea of the basic dimensions of the target). With the ultimate goal of implementing an effective landmine detection and identification GPR system, the second part of this thesis is concerned with the use of the Singularity Expansion Method (SEM) to aid in the identification problem once these objects have been detected.

Many different identification techniques have been proposed and attempted, including the (SEM) (Baum [24][25]) auto-regressive (AR) modelling of return signal (Rhenberegen REF), Image enhancement techniques such as polarimitry and Symmetry filters (Stiles, [26] Phelan, [27]), and image processing techniques such as moment based methods (Gilmore et. al. [28]). We have chosen to concentrate here on the SEM method.

Many of these techniques fall under what is called model-based parameter estimation (Miller and Sarkar). In these we analyze and create, on a physics based (i.e. Maxwell's equations) analysis of the general problem, some type of model and then fit the parameters of the model to our observed data. Part II focuses on the Singularity Expansion Method, which is a model-based parameter estimation technique.

6.1 The Singularity Expansion Method for Detection of Landmines

The Singularity Expansion Method was first introduced by Baum in 1971 [24] and reviewed in [25]. It arose from considering general electromagnetic scattering and has resulted in an effective method to identify large-scale (e.g., airplane) targets in free-space. The method has recently been expanded to aid in the identification of buried targets. For simplicity, we can explain the basic principles of the SEM method by considering an acoustic tuning fork. This description is based on Peters [44].

If an acoustic tuning fork is struck sharply, there is a short transient pulse followed by a long decaying ringing (or resonance, or natural response) at a the tuning frequency. This ringing signal can be described as

$$f(t) = Ae^{-\alpha t}\sin(wt) \tag{6.1}$$

where the amplitude term A is dependent upon the initial strike, while the decay term α and resonant frequency w are dependent only on the construction of the tuning fork (when the fork is located in free space). In the two-sided Laplace domain, we can represent $f(t)$ as:

$$F(s) = \frac{A}{s-(\alpha+jw)} + \frac{A}{s-(\alpha-jw)}, \tag{6.2}$$

where $s = \Omega + j\omega$ is the Laplace transform variable (or complex frequency). Thus, the identifying information of the particular tuning fork is located in a set of poles in the complex frequency domain, and these poles are independent of the excitation (initial strike). The magnitude of the poles is dependent on the exitation. These poles in the complex frequency domain are known as Complex Natural Resonances (CNR), complex poles, or simply poles.

Baum's major contribution in [24] was to prove that electromagnetic scattering could be represented in a similar fashion. We represent a scattered field component as

$$F(s) = \sum_{m=1}^{M} \frac{R_m}{s-s_m} + G(s) \tag{6.3}$$

where R_m is the residue, or strength of the particular pole, s_m is the m^{th} pole, and M is the total number of poles. $G(s)$ is an everywhere analytic (entire) function in the complex frequency plane. $G(s)$ is usually called the early time response, because it represents the initial 'strike' of the electromagnetic field.

The poles arise from resonant currents on (or in) the scatterer. The resonant currents will tend to follow very specific patterns for particular objects. The different locations of the set of poles corresponding to an object allow for the effective identification of the object illuminated by the incident pulse.

The advantages of the SEM method are clear. If a particular mode (resonance) can be excited on the target by the incident pulse, and that mode can be detected, then it provides some very specific information corresponding to the target that can be used to identify the target.

For humanitarian de-mining, we know the types of landmines and their construction that have been used in any particular minefield. This gives us targets for which we can calculate (either experimentally or computationally) electromagnetic responses. These responses allow the construction of a library of possible landmine targets. When a certain set of poles are detected from an unknown object we can then compare these to the library, and possibly identify the object.

6.1.1 Finding Poles from an Arbitrary Signal

To make the SEM an effective target identification technique, we must have a way of reliably detecting the poles of a given arbitrary signal contaminated with noise. Many methods have been proposed and implemented including the matrix pencil method (Sarkar [38] - [40]), Prony type methods such as the regular Prony, Least-Square Prony and Total-Least-Squares Prony (Hildebrand [41]), and State-Space based methods (Jang [42]). For an overview of some commonly used methods, see [42]. In this thesis, we implement the Matrix Pencil Method (MPM). The MPM has been shown to be equivalent or better in both accuracy and efficiency, than other competing algorithms [42].

6.2 The SEM Method for Buried Targets

When attempting to utilize the SEM method for buried targets, the problem becomes significantly more complicated. Here, we could imaging trying to strike a tuning fork in water. Clearly, the tuning fork will not resonate at the same frequency as in air due to the different acoustic properties of water. The complex poles of electromagnetic targets will similarly change when they are buried in an external medium.

6.2.1 Buried PEC Targets

For canonical Perfect Electric Conductor (PEC) targets, such as spheres and cylinders buried in a homogenous medium (i.e. not for the half-space problem), Baum [30] has provided analytic solutions. In [30] he also introduces a perturbation formula for general PEC targets buried inside a homogenous medium. The perturbation formulae for conducting targets perturb free space poles, i.e. the poles that arise when the PEC target is located in free space. The perturbation is a simple formula based only on the material parameters of the surrounding medium (see section 7.2), and is an exact solution (for the homogenous problem) when the material parameters are known and do not vary with frequency.

However, the basic perturbation formulae for PEC targets, given in [30], consider only targets buried in a homogenous medium, i.e. they do not take into account the air-ground interface. Hanson [33] has provided a further perturbation technique for targets buried in layered media. Using the layered media perturbation allows for the modelling of the air-ground interface. However, the perturbation formula in [33] is no longer as simple a transformation. For the layered medium perturbation of the free space poles, we must know the depth and orientation of the buried object in addition to the material parameters of the surrounding ground. While we may obtain an estimate of the depth from focused GPR images, the orientation of the object is extremely hard to determine.

6.2.2 Buried Dielectric Targets

To aid the identification of buried dielectric targets, Baum and Hanson [31][32] have introduced perturbation formulae to determine the resonances of buried dielectric targets based on the internal resonances of the object with PEC boundaries. These resonances are

not the same as the free-space poles used for the PEC perturbation formula. Again the dielectric perturbation formulae are for a homogenous external medium. Hanson's layered media perturbation formula [33] also applies, but again is aspect and depth dependent and no easy to use library could be constructed from its use.

To calculate the internal resonances of an arbitrary object one can either calculate analytically, or determine numerically, the internal resonances. These internal resonances, which are entirely on the imaginary axis in the complex frequency plane, combined with the perturbation formula outlined would form the basis of the library for identifying dielectric targets.

The dielectric perturbation formula is not an exact solution for the SEM poles (even for the homogenous case), as the internal resonances of the target buried in the external medium are not exactly as if the target were surrounded by PEC. Worthy, in [34], provides a comparison of the perturbation formula outlined in [31] with known analytic poles for canonical dielectric objects (such as a sphere) in a homogenous medium. No computational or experimental data are presented. He then provides graphs of the 'effective' area of the perturbation formulae presented by Baum and Hanson in [31] and [32]. An 'effective' perturbation is considered to be a pole that is within 6% of the analytic solution. In [35] and [36] Worthy provides libraries of responses for both cylindrical and rectangular dielectric mines.

6.2.3 Discussion of Buried Targets in General

The wide-band and resonant responses of buried targets (taking into account the air-ground interface) have been studied extensively using the Method of Moments (MoM) [45] - [54]. For an overview of recent developments, see Carin [45]. These papers utilize a half-space Green's function to calculate both full bandwidth time-domain responses and the resonances of targets of interest. Both dielectric and PEC targets are considered, although only Bodies of Revolution (BOR) are considered dielectric targets (see Geng, [46] and [47]).

The essential result of both Hanson's perturbation formula given in [33] and the numerical results of [45] - [54] is to show that as the depth of the buried target and the orientation of orientable targets varies, so do the poles. As the depth increases, the poles tend

to move in a spiral pattern around the poles for the object buried in a homogenous space. A good graphical example is given in [33], reprinted here in Figure 6.1, with permission from the author. The exact scale used for the axes in Figure 6.1 is not important, but it is

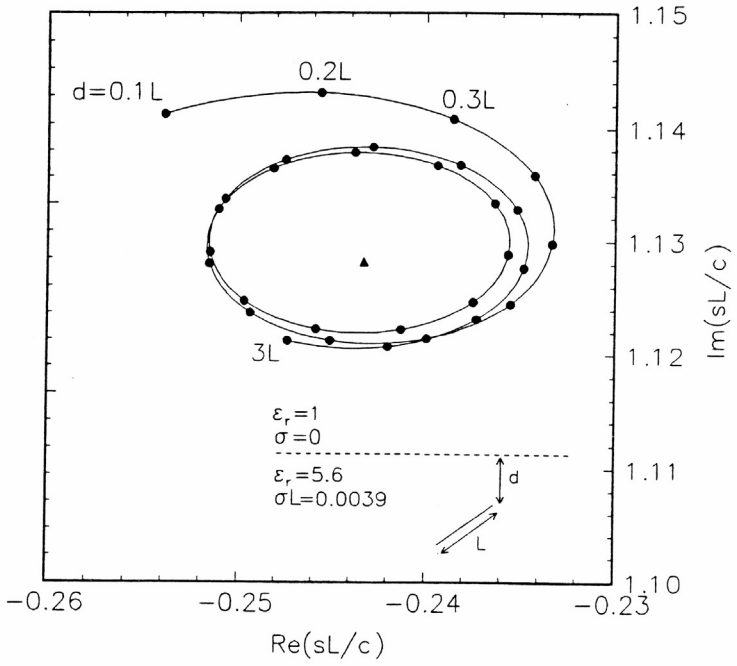

Fig. 5(a). Results of perturbation formula (35) for the natural frequencies of an inclined wire (45 degrees) in a lossy ground below an air half-space. Triangle denotes the natural frequency for a wire in a homogeneous-space (lossy ground).

Figure 6.1: Poles for Wire in Half-Space

(Reprinted with Permission from [33])

important to note that the scale is linear.

Thus, for buried targets, we would have to call the complex natural resonances of an object at best only *quasi*-invariant identification technique as the poles will change not only with ground parameters, but also with orientation and burial depth. However, from a survey of the pertinent literature ([45] - [54] and [33]) we can see that the variation of the imaginary part (frequency of resonance) from the homogenous case tends to be small, on the order of 5-10%, depending on orientation and burial depth.

In practical situations, the estimates of the ground parameters (σ and ε) will vary significantly over even a small area. Water content alone causes significant changes in

both ε and σ. For example, in sandy soils ε rises from $3\varepsilon_o$ to $30\varepsilon_o$, and σ rises from 0.001 to 0.1 for a water content rise of 0 to 40% [34]. Additional changes in material parameters come from the 'trenching effect' where the disturbed earth above the mine has different properties than the surrounding materials.

In addition to changes in ground material parameters, complications from other clutter, defined here as non-landmine targets, will preclude us from calculating the exact resonances of the object. As such, when we are attempting to decide whether a particular target is a landmine or clutter, an object giving rise to a pole within of 5-10% of our estimated poles for landmines buried in the area should be treated as a mine (i.e. exhumed).

6.3 Implementation of the SEM Method for GPR

While the resonances of buried objects have been studied numerically, there have been relatively few attempts to utilize the perturbation formulations for PEC and dielectric targets. In fact, only the PEC perturbation techniques have ever been implemented. In Wang [51], resonances of conducting planar objects are considered, and the PEC perturbation formulae of [30] and [33] are compared with MoM generated numerical results. The perturbation formulae correspond well with the MoM solution for conducting planar objects. In [37], Chen implements a GPR system for the detection of Unexploded Ordinance (UXO) and utilizes the basic perturbation formula in [30] to approximate the length of PEC scatterers buried underground. The results of the paper show some promise in the technique for conducting targets like UXO.

To this authors knowledge, no attempt at comparing the perturbation formulae for dielectric targets, even with computational data, has been presented. In addition, the use of the basic PEC perturbation formula has not been presented for landmine like targets either for computational methods or experimental data. To begin the preliminary exploration of the use of SEM for landmine detection, we implement a simplified GPR system in FDTD.

6.3.1 FDTD Simulation of GPR

With the ultimate goal of implementing a effective landmine GPR detection and identification system, we have chosen to simulate a GPR system using a Finite-Difference

Time-Domain (FDTD) code (Mardare et. al. [55]). FDTD techniques provide an effective tool for the simulation of GPR problems (see Bourgeois [56]).

Chapter 7

The Singularity Expansion Method

This chapter covers the essentials of the SEM method, then discusses the perturbation formulae for both PEC and dielectric buried targets. The implementation of the Matrix Pencil Method is discussed, as well as determining the onset of late-time.

This section of the thesis is presented in 'application oriented' format. Due to the fact that this is a preliminary investigation into the use of the SEM method for landmine identification/discrimination many of the in-depth proofs and derivations required for the use of the SEM method have been omitted. The references for the required proofs/derivations are provided at appropriate spots. For example, the derivations of the perturbation formulae for the poles of buried objects will not be presented, only the final results.

As previously mentioned, we have restricted our experimental data to Finite-Difference Time Domain (FDTD) produced synthetic data. No experimentally collected data from a laboratory environment is considered/presented. The FDTD method provides an accurate method to test the predictions that come from the use of the SEM method.

7.1 Introduction to the SEM

The basic diagram associated with the SEM problem is shown in Figure 7.1.

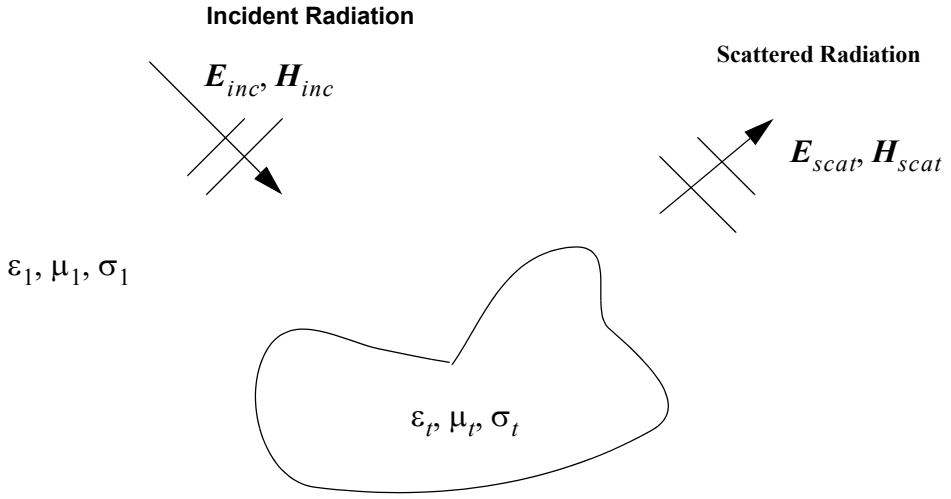

Figure 7.1: Scattering of an Incident Wave by a Target

Here, we present the equations for the SEM method for a PEC target ($\sigma_t = \infty$). The method can be extended for dielectric targets. If we assume the scatterer is illuminated with a plane wave of the form [25]

$$\boldsymbol{E}^{(inc)}(\boldsymbol{r}, t) = E_o f\left(t - \left(\frac{\mathbf{1}_i \cdot \boldsymbol{r}}{c}\right)\right)\mathbf{1}_p \tag{7.1}$$

which in the two-sided Laplace domain is written as

$$\tilde{\boldsymbol{E}}^{(inc)}(\boldsymbol{r}, s) = E_o \tilde{f}(s)\mathbf{1}_p e^{-\gamma(\mathbf{1}_i \cdot \boldsymbol{r})}, \tag{7.2}$$

where $\gamma = s/c$, s is the complex frequency, $c = (\mu\varepsilon)^{-1/2}$ is the speed of light in the external medium, $\mathbf{1}_i$ is the direction of incidence, and $\mathbf{1}_p$ is the direction of polarization. Here $\mathbf{1}_i \cdot \mathbf{1}_p = 0$ and $\tilde{f}(s)$ is the two-sided Laplace transform of $f(t)$.

The SEM form of the solution [25] for the current density on a PEC target is:

$$\boldsymbol{J}_s(\boldsymbol{r}_s, s) = E_o \sum_{m=1}^{M} \tilde{f}(s)\eta(\mathbf{1}_i, \mathbf{1}_p)\boldsymbol{j}_s(\boldsymbol{r}_s)[s - s_m]^{-1} e^{-(s-s_m)t_o} + \tag{7.3}$$

singularities of $\tilde{f}(s)$ + possible entire function

where $\eta(\mathbf{1}_i, \mathbf{1}_p)$ is a coupling coefficient, $\boldsymbol{j}_s(\boldsymbol{r}_s)$ is a natural mode, s_m is the complex natural resonance, M is the total number of poles and $\boldsymbol{r}_s$ is the space vector on the surface of the scattering object. In the time domain, the poles $[s - s_m]^{-1} e^{-(s-s_m)t_o}$ are replaced with $e^{s_m t} u(t - t_o)$.

7.1.1 SEM From a Signal Processing Perspective

Stepping from the electromagnetic domain and into the signal processing domain, we make the assumption that we can write our two-sided Laplace transform of the scattered signal, *after the onset of the poles at* $t = t_o$, from a target as:

$$F(s) = \sum_{m=1}^{M} \frac{R_m}{s - s_m^0} + G(s), \tag{7.4}$$

where $G(s)$ is an entire function representing the early-time contribution of the received scattered form. R_m is the residue of the m^{th} pole, s_m^0 is the location of the m^{th} free space pole, and M is the total number of poles. In general, $G(s)$ may contain poles itself (i.e., the poles associated with the transmitting antenna and transmitted waveform). However, for this discussion we assume that it is everywhere analytic (entire). We can represent the poles as

$$s_m^0 = \alpha_m + j\omega_m, \tag{7.5}$$

where α_m is the decay rate of the pole, and ω_m is the frequency. For real time domain signals (as seen in all real radar problems) we expect the poles to occur either on the $\omega = 0$ (real) axis, or in complex conjugate pairs. In stable problems (again all real radar problems) α_m will be negative, i.e. the received signal will decay towards zero.

In the time domain, the received signal, $f(t)$ can be represented as

$$f(t) = \sum_{m=1}^{M} |c_m| e^{[(\alpha_m + j\omega_m)t + j\phi_m]} + g(t) = \sum_{m=1}^{M} R_m z_m^t + g(t), \tag{7.6}$$

where

$$R_m = |c_m| e^{j\phi_m}, \tag{7.7}$$

and

$$z_m = e^{(\alpha_m + j\omega_m)}. \tag{7.8}$$

If we assume, for example, that all poles come in complex conjugate form, then M is even, and

$$f(t) = \sum_{m=1}^{M/2} R_m e^{\alpha_m t} \cos(\omega_m t) + g(t) \ . \tag{7.9}$$

In other words, if there is no DC component of our scattered signal, we can represent the late time portion of the signal as a sum of exponentially damped sinusoids.

An example of a free space scattered signal from a long, thin, wire like object is seen in Figure 7.2. This represents the scattered field from a perfect electric conductor 40 cm x

1cm x 1cm. The incident field is at a 45 degree angle to the length of the wire, and an amplitude of 1 kV/m, polarized in the E_x direction. This data was obtained using FDTD.

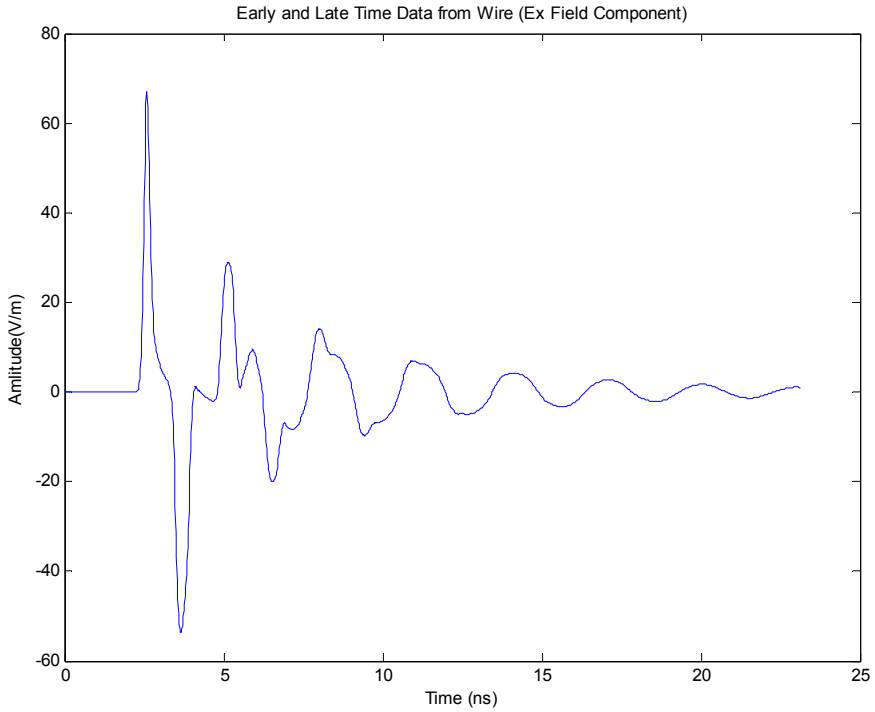

Figure 7.2: Early and Late Time Representation of a Signal

Here, we can see an early-time signal (around 3-6 ns) that, in later time becomes a summation of exponentially damped sinusoids (poles).

7.1.2 Determining the Onset of Late-Time

In order to properly model our scattered signal from an object as a set of complex poles, we need to distinguish between the so-called early and late-times. Determining the onset of late-time can be viewed as determining the time $t = t_o$ in equation (7.3). Only the late-time content can be modelled with a summation of damped sinusoids. Typically, the early-time consists of impulse-like components.

The problems with finding the onset of late-time have received some attention (see for example, Selli [43]). However, for the purposes of this preliminary investigation we utilize a process of trial and error in order to determine the onset of late-time. If the reso-

nances have a low damping coefficient, we can usually visually distinguish an adequate location to switch from early-time to late-time.

7.2 Perturbation Formula For Buried PEC Targets

In 1993, Baum presented the perturbation for the SEM method for Perfect Electric Conductor (PEC) targets buried in a surrounding homogenous, non-magnetic medium [30]. The setup for the problem is the same as in Figure 7.1, with $\sigma_t = \infty$, and the external medium having material parameters $\varepsilon_1 = \varepsilon_r\varepsilon_0$, $\mu_1 = \mu_0$ and σ_1. The material parameters are assumed to be frequency independent. It is important to note that Baum's perturbation formula is for the poles in a homogenous medium and that it is analytically derived with the only approximation being that the material parameters are frequency independent. The more complicated situation of layered media is discussed in [33], but as previously mentioned, the perturbation formula of [33] requires knowledge of the material parameters, target orientation and shape, and the burial depth while providing limited extra accuracy. As such, it is not presented here.

Given that an object a has free space pole given by s_m^o, Baum's analytic formula for the perturbed poles in the external medium is

$$s_m = -\frac{\sigma_1}{2\varepsilon_r} \pm \left[\left(\frac{\sigma_1}{2\varepsilon_r}\right)^2 + \frac{1}{\varepsilon_r}(s_m^o)^2\right]^{1/2}, \tag{7.10}$$

where s_m is the perturbed pole, and the $+$ term is selected for s_m^o in the right-hand s plane (i.e, positive real part of s), and the $-$ is selected for s_m^o in the left-hand s plane. Baum also notes that there is a possible branch cut introduced into the representation of the scattered signal in the Laplace domain. However, the branch cut occurs only for dispersive external medium [29]. In this discussion, no dispersive external media are considered, so the branch cut is not considered here.

For high frequencies, (frequencies above the so called relaxation constant of the medium) where $|s_m| \gg \sigma_1/\varepsilon_1$, the perturbation formula becomes

$$s_m = \frac{1}{\sqrt{\varepsilon_r}} s_m^o - \frac{\sigma_1}{2\varepsilon_r} + O(s_m^o). \tag{7.11}$$

This is a simple scaling of the poles by $1/\sqrt{\varepsilon_r}$, and a shift along the real axis by $\sigma_1/(2\varepsilon_r)$. As Baum notes, for high frequencies we expect the pattern of the poles to remain the same, and possibly aid in identification.

To implement this perturbation formula, we must have prior knowledge of the type targets we are attempting to find. This is usually not a problem, because for humanitarian demining we have lists of what types of landmine were buried and approximate locations (see, for example, [35] and [36]). To utilize the perturbation formula presented here it is required that we find the free space poles of the scattering object, and know the materials of the surrounding ground. For a PEC the free space poles can easily be found either numerically, utilizing some type of EM modelling code (such as FDTD), or experimentally in an anechoic chamber. The ground parameters could be found by taking several samples of the ground in suspected burial sites.

7.3 Perturbation For Dielectric Targets

The problem of detecting the resonances of dielectric targets is a much more complicated problem than detecting the resonances of a PEC target. In general, the resonances are significantly weaker for the dielectric targets [37]. The set up for the problem again follows from Figure 7.1, but with the external medium having parameters ε_1, μ_o and σ_1. The target will be a loss-free dielectric with parameters ε_2 and μ_o.

In [32] Hanson and Baum provide an approximate perturbation formula for arbitrarily shaped scatterers based not on the free-space resonances, but on the interior cavity resonances, which are located on the $j\omega$ axis in the Laplace (s) plane. Again, Hanson in [33] provides a perturbation formula for layered media but it is dependent on the burial depth and orientation of the target.

The key assumption made in the basic dielectric perturbation formula is that there is a high contrast between the target and external medium wave impedances, which translates into a high contrast in the permittivities from target to ground. The wave impedance in the external medium in the Laplace-domain is given by

$$Z_1 = \sqrt{\frac{\mu_o}{\varepsilon_1}}\left[1 + \frac{\sigma_1}{s\varepsilon_1}\right]^{-\frac{1}{2}}. \tag{7.12}$$

The Laplace domain wave impedance of the target is given by:

$$Z_2 = \sqrt{\frac{\mu_o}{\varepsilon_2}}. \tag{7.13}$$

The ratio of the internal to external wave impedances is defined as:

$$\xi(s) \equiv \frac{Z_2(s)}{Z_1(s)} = \sqrt{\frac{\varepsilon_1}{\varepsilon_2}}\left[1 + \frac{\sigma_1}{s\varepsilon_1}\right]^{\frac{1}{2}}. \tag{7.14}$$

As $\xi \to \infty$, we can assume that the target is surrounded by a PEC [31]. This creates a set of interior cavity resonances, that for canonically shaped targets (such as rectangular cavities or cylindrical cavities) can be analytically calculated. For example, the internal resonances of a rectangular cavity can be found in [3]. For non-canonically shaped objects the internal resonances would have to be found numerically or experimentally. We denote these unperturbed internal resonances as s_α^o. These resonances will be on the $j\omega$ axis, because the targets have no losses.

Under the assumption of a large impedance ratio, $\xi \gg \sqrt{\varepsilon_1 / \varepsilon_2}$, we can represent the perturbed poles as

$$s_m = s_\alpha^o + \Delta s_\alpha, \tag{7.15}$$

where the shift in the pole is given by

$$\Delta s_\alpha = \frac{-1}{2\xi(s_\alpha^o)\sqrt{\mu_o \varepsilon_2}}\left[\frac{\oint_S |\boldsymbol{H}_o|^2 dS}{\int_V |\boldsymbol{H}_o|^2 dV}\right]. \tag{7.16}$$

The area of integration is on the surface and volume of the cavity, where $\boldsymbol{H}_o$ is the unperturbed magnetic field of the internal cavity resonances.

There exists a source of error that is intrinsic to the use of this formula (7.16). The assumption that the field $\boldsymbol{H}_o$ is the field when the target is surrounded by PEC does not match the physical reality, where the target is surrounded by another dielectric (with a

higher relative permittivity. How this source of error effects the perturbed poles is explored by Worthy [34].

7.4 The Matrix Pencil Method

The SEM method is not practical without a method to extract the poles and residues from the late-time signal. Many methods have been proposed and implemented including the matrix pencil method [38] - [40], Prony type methods such as the regular Prony, Least Square Prony and Total-Least Squares Prony [41], and State Space based methods [42]. All these methods are concerned with determining, from an arbitrary *digital* (or discrete time) signal, the best fit of a series of exponentials. Two major concerns are the performance in noise, and how to decide the number of poles with which to model the signal (i.e. how to pick M).

In this thesis, we consider the Total Least-Squares (TLS) Matrix Pencil Method (MPM). In the presence of noise, the TLS-MPM has been shown to perform better or as well as other competing techniques [42]. The underlying assumption of the MPM is that the late-time part of the scattered signal $y[k]$ (which has now been digitized), can be modelled as a linear combination of damped sinusoids:

$$y[k] = \sum_{m=1}^{M} R_m z_m^{kTs} \tag{7.17}$$

where R_m and z_m are given in equations (7.7) and (7.8) respectively, T_s is the sample period and $k = 0, 1 \ldots N-1$.

The derivation of the matrix pencil method is presented in [40]. This particular implementation of the TLS-MPM is given in [42]. We begin by constructing a Hankel matrix, $[Y]$ as

$$[Y] = \begin{bmatrix} y(0) & y(1) & \ldots & y(L) \\ y(1) & y(2) & \ldots & y(L+1) \\ \ldots & \ldots & \ldots & \ldots \\ y(N-L-1) & y(N-L) & \ldots & y(N-1) \end{bmatrix}_{(N-L)\times(L+1)} \tag{7.18}$$

where N is the total number of samples in the signal $y[k]$, and L is the so-called pencil parameter which, for efficient noise filtering, should be chosen in the range $N/3$ to $N/2$. For a large amount of samples, the particular selection of L makes little difference [43].

Next, we complete the Singular Value Decomposition (SVD) of the matrix $[Y]$ written as

$$[Y] = [U][\Sigma][V]^H, \tag{7.19}$$

where $[U]$ and $[V]$ are matrices composed of the eigenvectors of $[Y][Y]^H$ and $[Y]^H[Y]$ respectively. H represents the complex conjugate transpose, and $[\Sigma]$ is the singular value matrix, containing only diagonal elements of the singular values of $[Y]$.

The matrix $[\Sigma]$ allows us to make an extremely important step in the MPM process. At this point, $[Y]$ is an ill-conditioned matrix. By analyzing the relative magnitude of the singular values, σ_m inside the singular matrix $[\Sigma]$, we can get an idea of how many poles, M, we should select to model our signal $y[k]$. For example, if we have collected data with p significant digits, then all singular values σ_c, such that

$$\frac{\sigma_c}{\sigma_{max}} \leq 10^{-p} \tag{7.20}$$

are singular values (and therefore, poles) that are caused by numerical noise.

After M total singular values have been selected, we then create a 'filtered' version of $[V]$, $[V']$, which contains only the M vectors of $[V]$ corresponding to the M largest eigenvalues. For example, if $[V]$ is a $C \times C$ matrix, then $[V']$ will be a $C \times M$ matrix. It is this step in the MPM that allows for efficient noise filtering, and provides an effective method for selecting the number of poles with which to model the signal.

We then construct two matrices from the 'filtered' matrix $[V']$: $[V_1']$ and $[V_2']$. $[V_1']$ is obtained from $[V']$ by deleting the last row of $[V']$. $[V_2']$ is obtained by deleting the first row of $[V']$. Thus, both $[V_1']$ and $[V_2']$ will be $C \times M - 1$ sized matrices. Finally, the complex poles, z_m, are given by

$$z_m = eig(\{[V_1']^H\}^+ [V_2']^H) = eig([V_2']^H \{[V_1']^H\}^+), \tag{7.21}$$

where eig denotes an operator that retrieves the eigenvalues of a matrix, and + denotes the generalized (Moore-Penrose) inverse.

Once the poles, z_m are known, the residues, R_m can be found from the least squares problem:

$$\begin{bmatrix} y(0) \\ y(1) \\ \cdots \\ y(N-1) \end{bmatrix} = \begin{bmatrix} 1 & 1 & \cdots & 1 \\ z_1^{Ts} & z_2^{Ts} & \cdots & z_M^{Ts} \\ \cdots & \cdots & \cdots & \cdots \\ z_1^{(N-1)Ts} & z_2^{(N-1)Ts} & \cdots & z_M^{(N-1)Ts} \end{bmatrix} \begin{bmatrix} R_1 \\ R_2 \\ \cdots \\ R_M \end{bmatrix}. \tag{7.22}$$

Chapter 8

Results and Conclusions from Part 2

This chapter presents the methodology used for synthesizing data for a simple GPR model using the Finite-Difference Time-Domain (FDTD) algorithm and presents the results of applying the SEM method to this data. Data is presented for a variety of targets, including PEC wires and mine-like targets, as well as dielectric mine-like targets.

The perturbation formulae for PEC and dielectric targets are implemented and compared with the FDTD generated data.

8.1 Total Field Formulation FDTD Generation of Data

Consider the geometry of the FDTD problem as shown in Figure 8.1. Here we are utilizing the total field formulation of FDTD.

The FDTD space is defined physical locations $0 < x < 60$ cm, $0 < y < 61$ cm, and $0 < z < 30$ cm. The spacing is uniform, with all step sizes being 1 cm. We have defined a simplified GPR antenna to direct more of the EM energy into the ground by creating 12 PEC objects of zero thickness in the FDTD space at $z = 15$. This antenna is clearly not

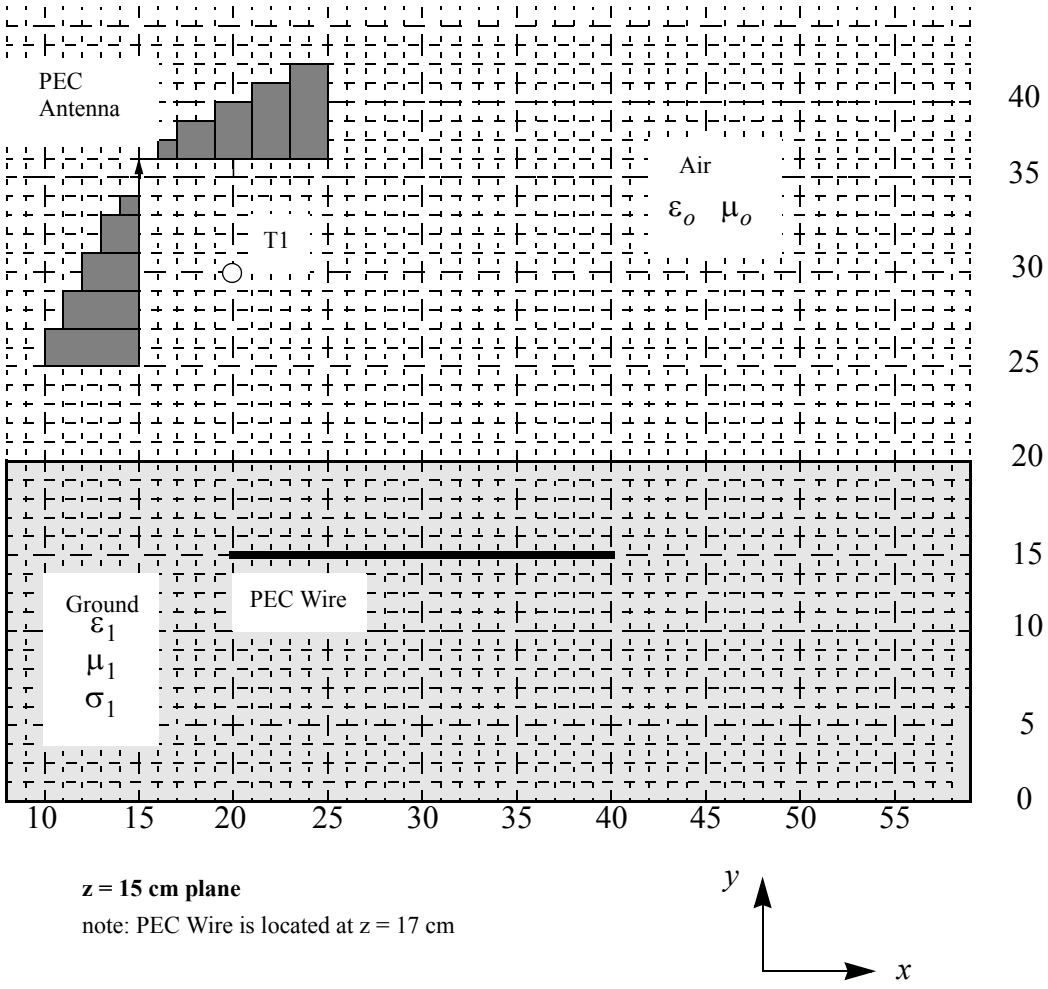

Figure 8.1: FDTD GPR System

an accurate description of an experimental (field) GPR system, but is used for this proof-of-concept investigation.

The ground is defined from locations $0 < x < 60$, $0 < y < 20$ and $0 < z < 30$. The parameters of the ground for the lossless case are $\varepsilon_1 = 4\varepsilon_o$, $\mu_1 = \mu_o$ and $\sigma_1 = 0$. For the case of lossy ground, we set $\sigma_1 = 0.01$. These parameters approximate the material parameters of dry sand. For the cases of dielectric targets we increase the permittivity to $\varepsilon_1 = 10\varepsilon_o$. Here, we could consider wetting the sand to artificially increase the difference in dielectric constants between the landmines and surrounding ground.

There are several different targets considered for the simplified GPR system, but the target shown in Figure 8.1 is a PEC 'wire' of 20cm x 1cm x 1cm. The FDTD locations are $20 < x < 39$, $y = 15$ and $z = 17$. PEC is defined as having $\sigma_t = \infty$. Other targets will be discussed in the appropriate sections.

For the source, we excite the y-component of the current density at grid location $x = 15$, $y = 35$ and $z = 15$. The imposed current density, J_y is given the time-domain form of the derivative of a Gaussian function

$$J_y(15, 35, 15) = -2\frac{(t - t_o)}{b^2} e^{-\frac{(t-t_o)^2}{b^2}} \tag{8.1}$$

where $t_o = 2x10^{-9}$, and $b = 5x10^{-10}$. A graph of the time domain of the Gaussian pulse is shown in Figure 8.2, and the magnitude of the frequency domain is shown in Figure

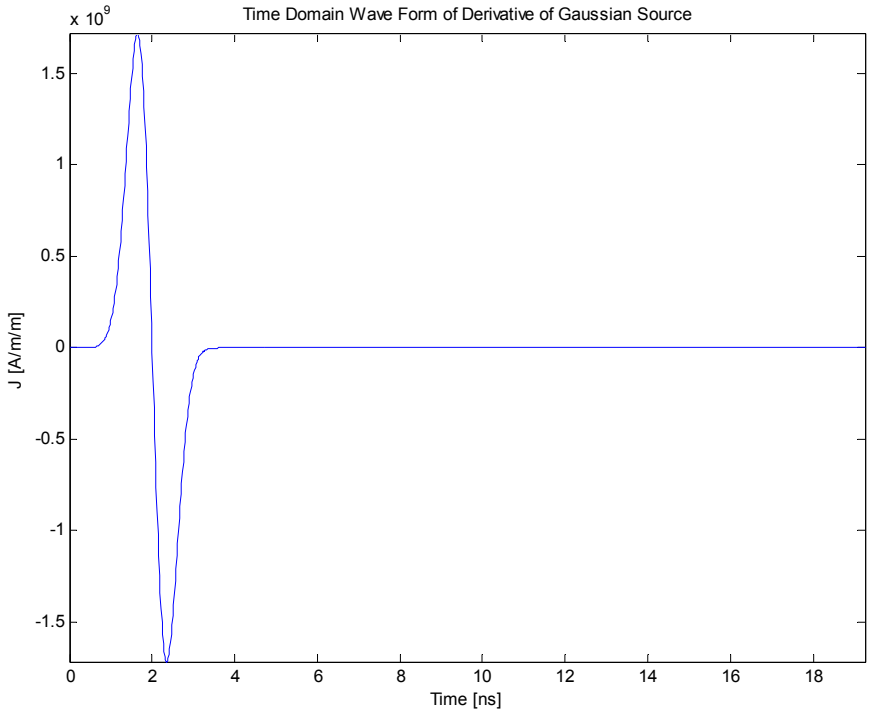

Figure 8.2: Time Domain Wave Form of Derivative of Gaussian Source

8.3.All 3 rectangular electric field components E_x, E_y and E_z are recorded at point T1

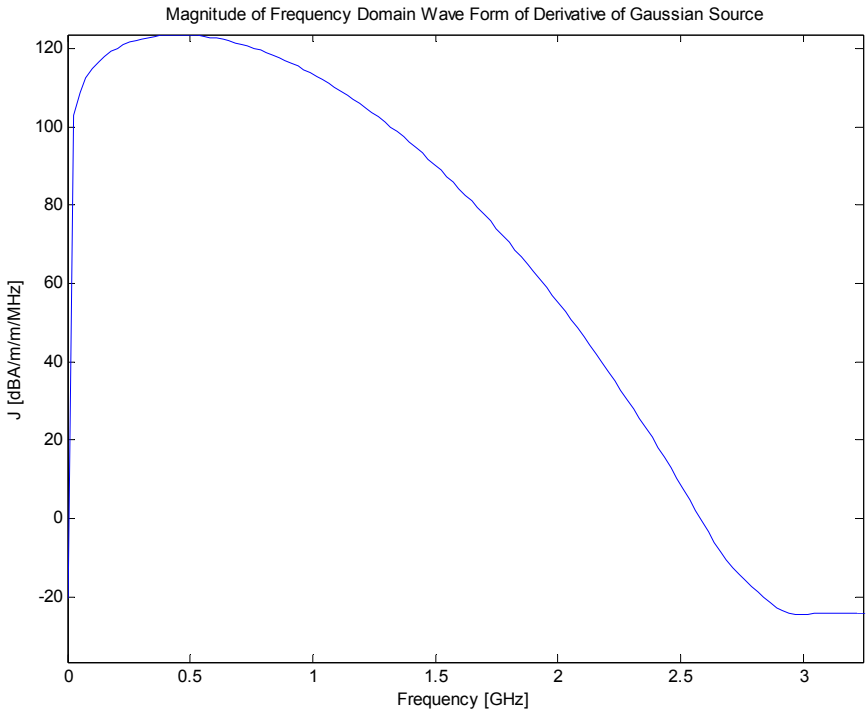

Figure 8.3: Magnitude of Frequency Domain of FDTD Source

which has been placed at the location $x = 20$, $y = 30$ and $z = 15$.

An example of an FDTD code source file is given in Appendix B.

8.1.1 Generation of FDTD Data

In all cases we have constructed our target response in the following manner:

1. The FDTD code was run with only the antenna and ground present
2. The FDTD code was then run with antenna, ground and target present

The target response is then calculated by subtracting the second run of the code from the former. For free-space responses, the same two tests were run but without the ground. This process is allowable because of the linearity of EM fields. This clearly is not a situation that is applicable to a practical landmine identification system but for this preliminary

investigation it provides results that are instructive to test the perturbation formulae from the preceding chapter.

Table 8.1 List of FDTD Experiments Conducted

Experiment Number	Target	Ground Type	Shown in Thesis
1	PEC Wire	Lossless	Yes
2	PEC Wire	Lossy	Yes
3	PEC Landmine	Lossless	Yes
4	PEC Landmine	Lossy	Yes
5	Dielectric #1	Lossless	Yes
6	Dielectric #1	Lossy	No
7	Dielectric #2	Lossless	No
8	Dielectric #2	Lossy	Yes

A list of experiments conducted is provided in Table 8.1. The exact details of each experiment are provided in the pertinent section.

8.2 Experiments 1 and 2: Twenty Centimeter PEC Wire

The first experiment was conducted with a high-Q resonator: a 20cm x 1cm x 1cm PEC wire. Its location in the FDTD grid is $20 < x < 39$ cm, $y = 15$ cm and $z = 17$ cm. First, the free space poles are determined. Next, we consider the wire buried in a both a lossy and non-lossy dielectric ground (half space).

8.2.1 Free Space Poles of 20 cm Wire

The free space response of the wire was determined by running the FDTD code with only the antenna present, then running it again with both the antenna and wire present. The

E_x wave-form at point T1 in the FDTD space resulting from the subtraction of the free space result from the antenna result is shown in Figure 8.4

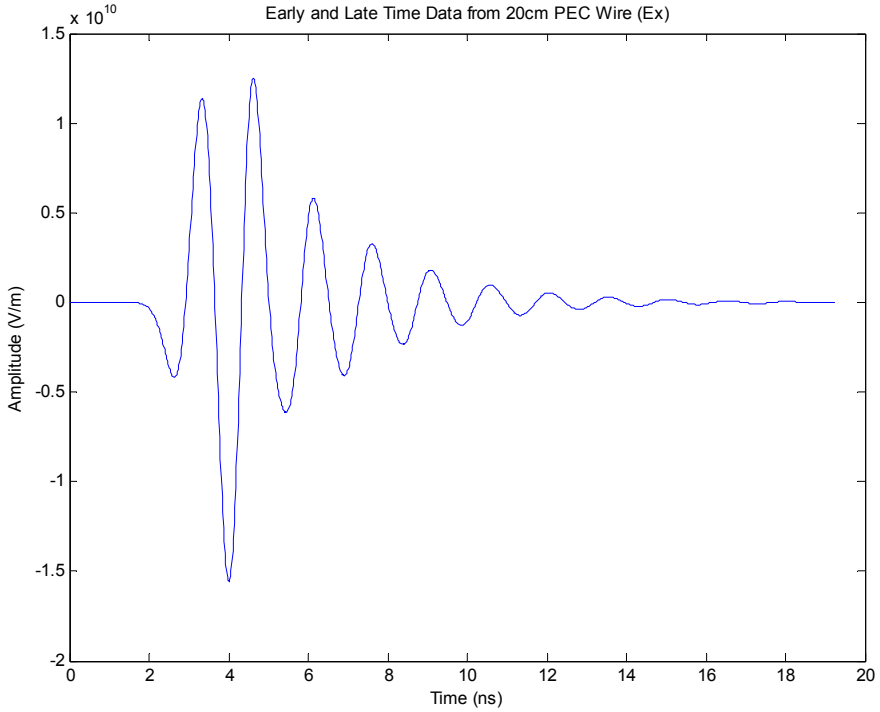

Figure 8.4: Ex from 20 cm x 1 cm x 1 cm PEC Wire in Free Space

By a process of trial and error, an onset of late-time of 6 nanoseconds was selected. From the time-domain response it is clear that at 6 ns we have reached the resonant (late-time) part of the scattered signal.

Next, the MPM was applied to the late-time portion of the signal ($t > 6ns$). The plot of the first 100 singular values is shown in Figure 8.5. As can be seen from the plot, the

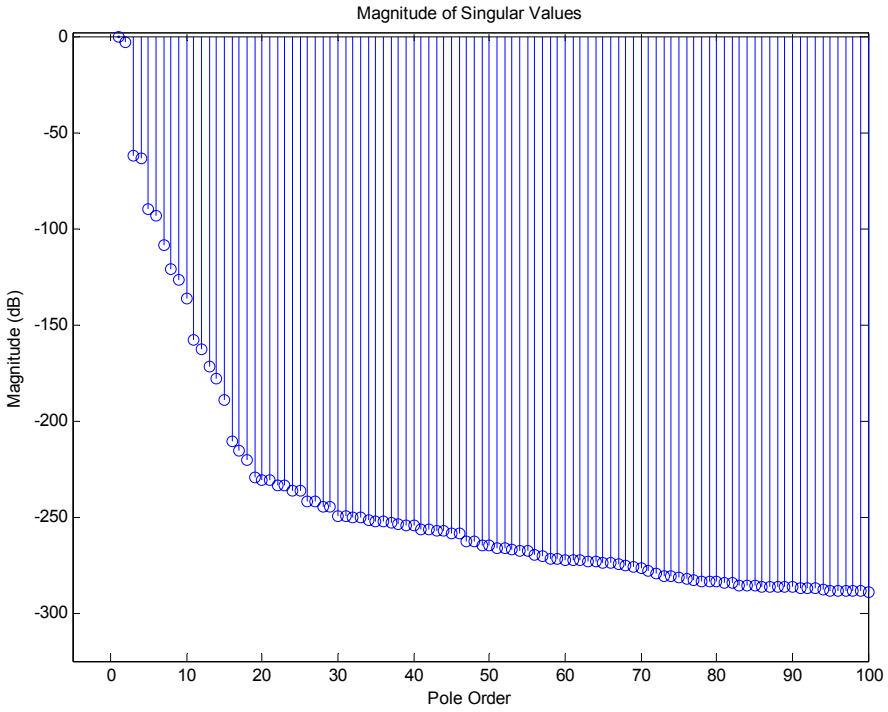

Figure 8.5: Magnitude of Singular Values for 40 cm PEC Wire

assumption of 2 poles fits quite well, because all poles beyond the 2nd are over -50 dB below the most dominant pole. However, it is recommended (Sarkar [58]) to over-estimate the number of poles slightly. As such, the late-time portion of this signal was modelled with 4 poles. The free space poles of the 20 cm PEC wire with the onset of late-time at 6

ns are given in Figure 8.6. Note that the poles come in complex conjugate pairs. The loca-

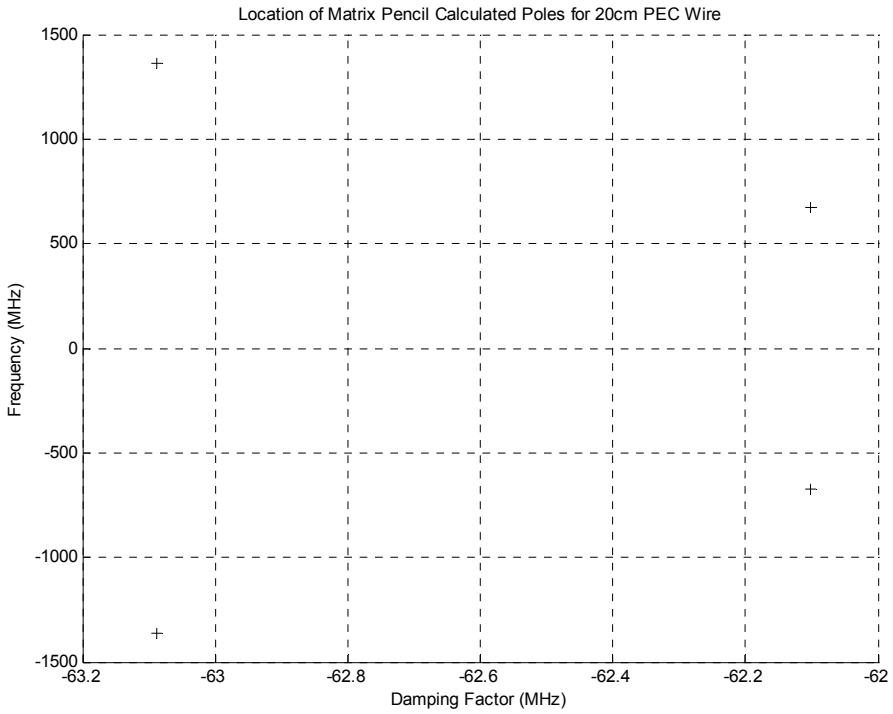

Figure 8.6: Poles for Free Space 20cm PEC Wire

tions of the positive frequency free-space poles are listed in Table 8.2.

Table 8.2 PEC Wire Free-Space Pole Locations

Description	Pole #1 (MHz)	Pole #2 (MHz)
Free Space Poles	$-62.1 + j675.6$	$-63.1 + j1364.6$

With a 20cm long resonator, we expect the most dominant pole to occur when $\lambda/2 \cong 0.2$. The resonant frequency ($f_{resonant} = c/\lambda$) occurs at 750 MHz. Since this resonant frequency is exact only for an infinitely thin wire, we expect the most dominant pole's frequency to occur slightly below $f_{resonant}$. Table 8.2 shows that the main resonant frequency occurs at 675.6 MHz, which is a reasonable result. This set of free-space poles is used for the poles s_m^o in equations (7.10) and (7.11).

It seems that higher order poles are not excited by the pulse that is transmitted across the FDTD grid. It is assumed here that if we used a pulse with higher frequency that more (higher frequency) poles would be visible in the above signal. We have not used a higher frequency pulse because in FDTD transmission of higher frequencies requires a finer grid spacing, which results in extended computation time. This problem is discussed in more detail in section 8.4.

8.2.2 Twenty cm Wire Buried in Lossless Ground

Next, we considered the effects on the poles by burying the 20cm x 1cm x 1cm wire in a half space with $\varepsilon_r = 4$, $\mu_r = 1$, and $\sigma_1 = 0$ (lossless ground). Here, we apply Baum's transformation seen in equation (7.10). Equation (7.10) is equivalent to equation (7.11) for lossless media. Once again, the FDTD program was run with the only the antenna and ground present, then run a second time with the antenna, ground, and target present. Figure 8.7 shows the E_x field component at location T1.

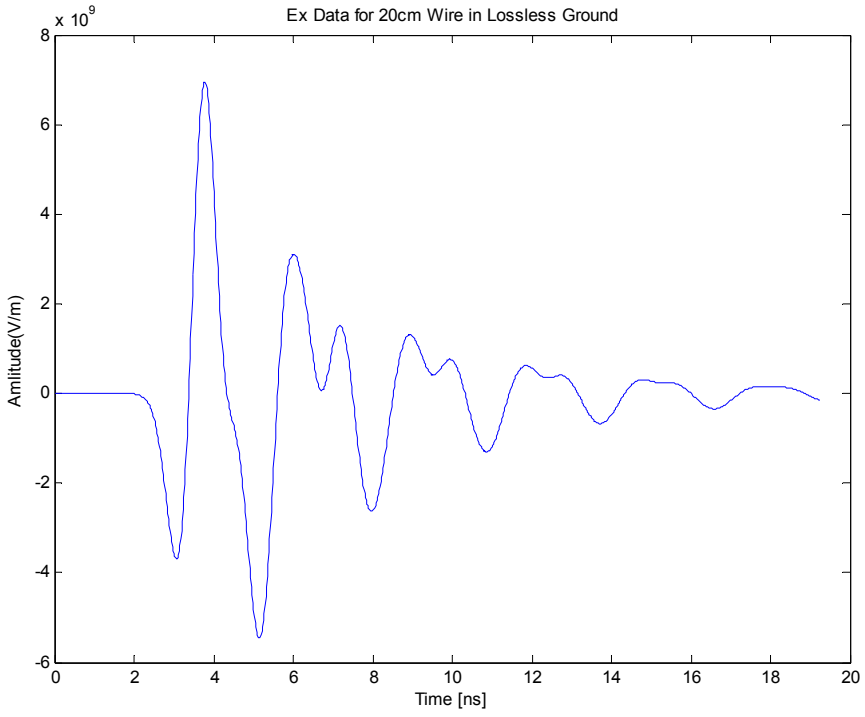

Figure 8.7: Ex from 20 cm x 1 cm x 1 cm PEC Wire Buried in Lossless Media

By visual inspection, the late-time onset was determined to be around 6 ns. The resulting poles are shown in Figure 8.8. Here, the perturbed free-space poles are shown as

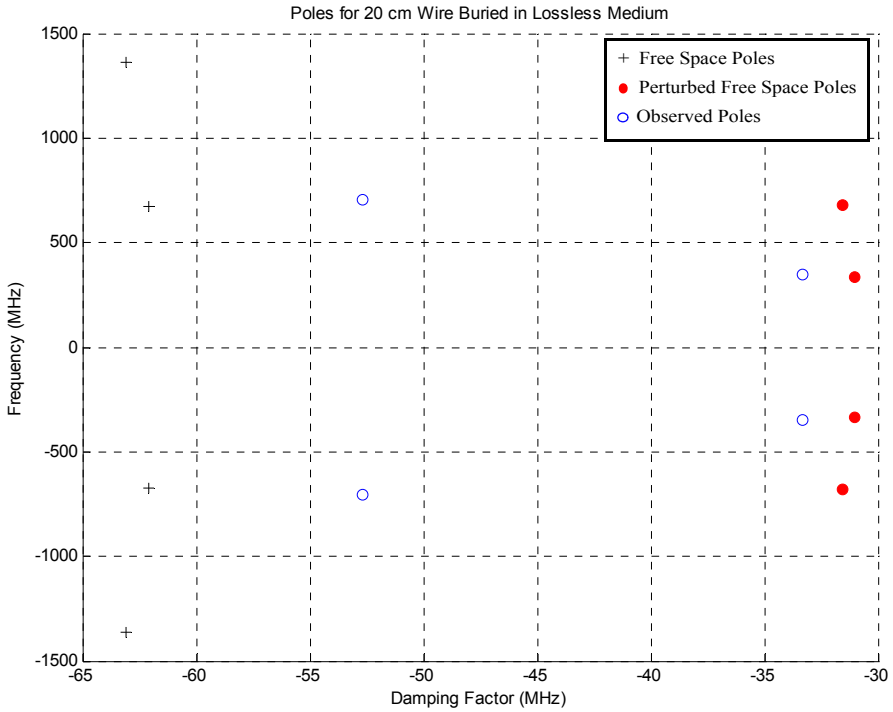

Figure 8.8: Poles for 20 cm Wire Buried in a Lossless Medium

filled circles, free space poles are shown as '+' signs, and the poles observed in the buried target signature as hollow circles. The poles all come in complex conjugate pairs, and Table 8.3 lists the positive frequency poles.

Table 8.3 PEC Wire in Lossless Medium Pole Locations

Description	Pole #1 (MHz)	Pole#2 (MHz)
Perturbed	$-31.1 + j337.8$	$-31.5 + j682.3$
Observed	$-33.3 + j345.9$	$-52.7 + 706.6$

Overall, the two least damped poles (Pole #1) offer the best correlation from perturbed to observed poles. There is a reasonably good correlation for both the decay rate (real part) and the resonant frequency (complex part). However, for Pole #2, we see that the damping ration does not correspond well between perturbed and observed pole. In

both cases, the resonant frequency is reasonably close. The discrepancy between damping ratios has been noted by other researchers [37]. We do not currently have a complete explanation of this phenomenon.

The differences seen in the resonant frequencies can all be attributed to the fact that the perturbation formula used is meant for a target in homogenous space, while here the target is in a half-space. As discussed in the introduction, research on the resonances of objects buried in a half-space has shown that the poles will change location from the homogenous case [33]. While this can account for the differences of frequency seen, it does not fully account for the differences in damping ratios.

This discrepancy seen in the damping ratio was commonly seen with our data when utilizing the SEM for buried object detection. In the majority of cases, it was not useful for identification purposes but the resonant frequency was useful for identification purposes. These unexpected shifts in the damping ratio also precludes the use of the pole pattern as an additional identifying technique (as suggested by Baum in [29]).

8.2.3 Twenty cm Wire Buried in Lossy Ground

The same process was repeated, except with ground parameters $\varepsilon_r = 4$, $\mu_r = 1$, and $\sigma_1 = 0.01$. Here, we again performed the subtraction of the FDTD data. We selected 4 poles, and the onset of late time was determined to be 7 ns. The plot of the E_x field at

location T1 is shown in Figure 8.9. Here, we can easily see that the resonances are more

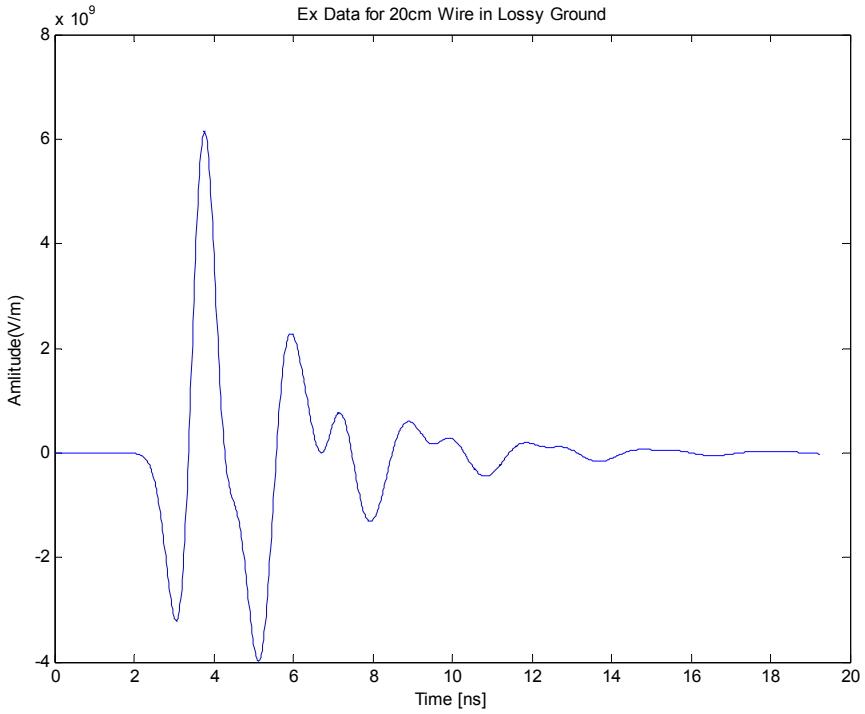

Figure 8.9: 20 cm Wire Buried in Lossy Medium

highly damped.

The final result of the MPM is shown in Figure 8.10, and the exact location of the positive frequency perturbed and observed poles are given in Table 8.4.

Table 8.4 PEC Wire in Lossy Medium Pole Location

Description	Pole #1 (MHz)	Pole #2 (MHz)
Perturbed	$-53.6+j337.1$	$-54.0+j681.9$
Observed	$-49.6+j342.6$	$-76.8+j694.3$

As with the lossless case, we see close correlation with the frequencies of the observed poles to the calculated poles, but poor correlation overall in the damping ratio. The damping ratio of the least damped set of poles could possibly be used to help identify the target. The observed resonant frequencies for the least damped poles are located at

342.6 MHz, and the (perturbation formula) calculated resonant frequencies are at 315.2 MHz. For the secondary poles, the observed resonant frequencies are at 694.3 MHz and the perturbed poles are at 681.9 MHz. Again, we can attribute the differences to the fact that we have a resonant object buried in a half-space rather than a fully homogenous space.

We note here that even in a lossy ground, this method of detecting resonant frequencies allows for at least preliminary identification of a highly resonant PEC object.

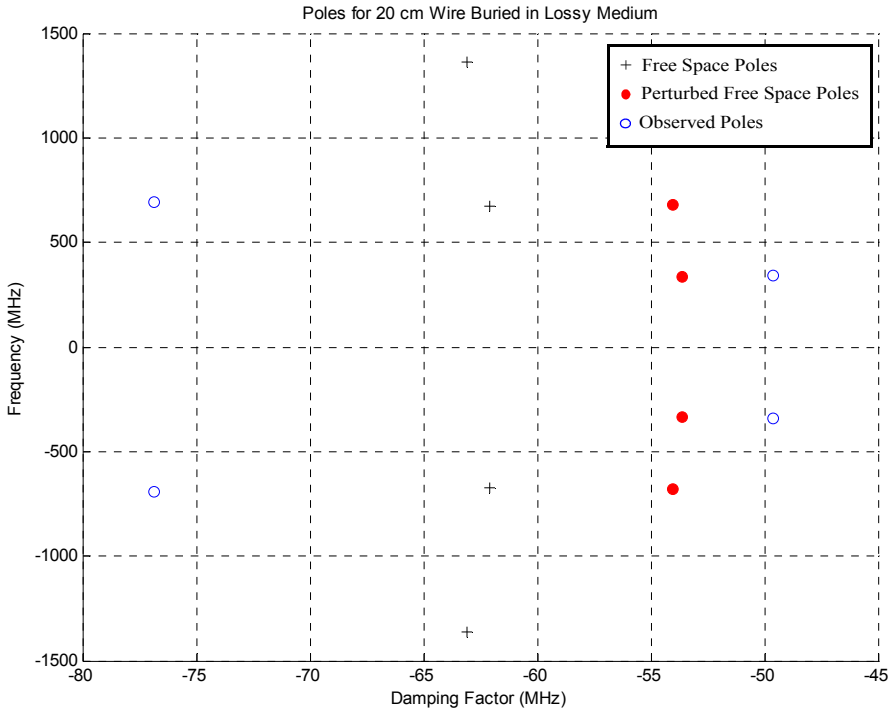

Figure 8.10: Poles for 20 cm Wire Buried in Lossy Medium

8.3 PEC Landmine

Next, we considered a PEC landmine of the dimensions 12cm x 5 cm x 6 cm. Its location in the FDTD grid is $26 < x < 37$ cm, $11 < y < 15$ cm and $13 < z < 17$ cm. We again illuminated the PEC landmine in free space in order to obtain the free space poles. The same illuminating pulse as shown in Figure 8.2 and Figure 8.3 was used.

The time domain response of the E_x field component at point T1 of the PEC landmine in free space is given in Figure 8.11. As can be seen from this plot, the resonances are much more highly damped and much harder to find compared to the wire-like resonators (i.e. we have a low-Q resonator).

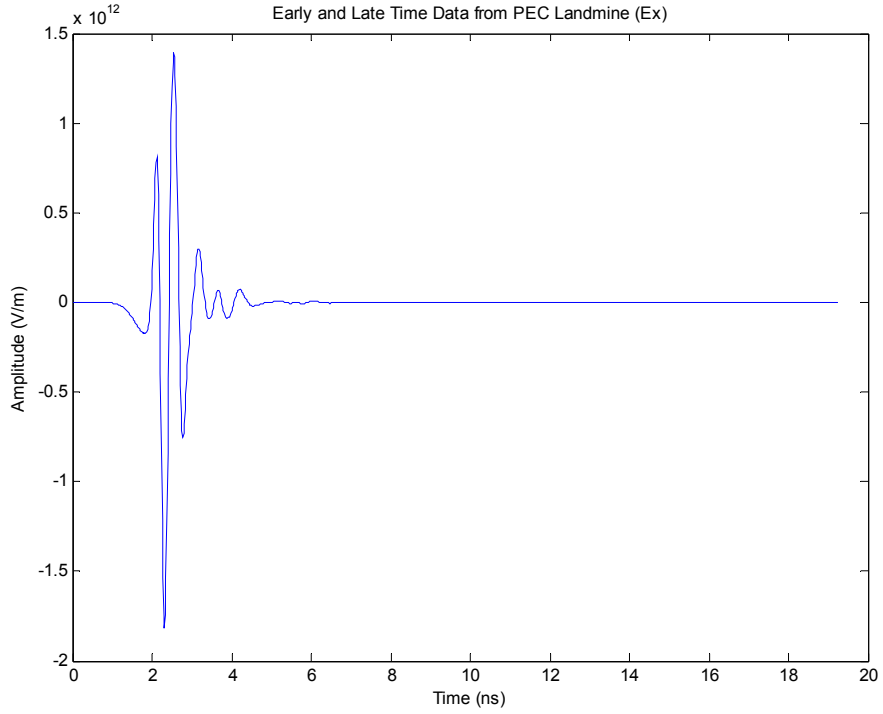

Figure 8.11: Free Space Response from PEC Landmine at T1

Because of significantly higher damped poles, the onset of late-time is much harder to determine. In this case, trial and error was utilized and the onset of late-time was selected to be 2.5 ns. When this choice, 6 poles modelled the signal well. The resultant free space poles can be seen as the '+' marks in Figure 8.13 and Figure 8.14. The exact positive frequency poles are given in Table 8.5.

8.3.1 PEC Landmine Buried in Lossless Medium

Next, the PEC landmine was buried in a lossless medium with $\varepsilon_r = 4$, $\mu_r = 1$. The standard subtracted time domain response was calculated and is shown for the E_x

component at point T1 in Figure 8.12. The positive frequency poles, including the free

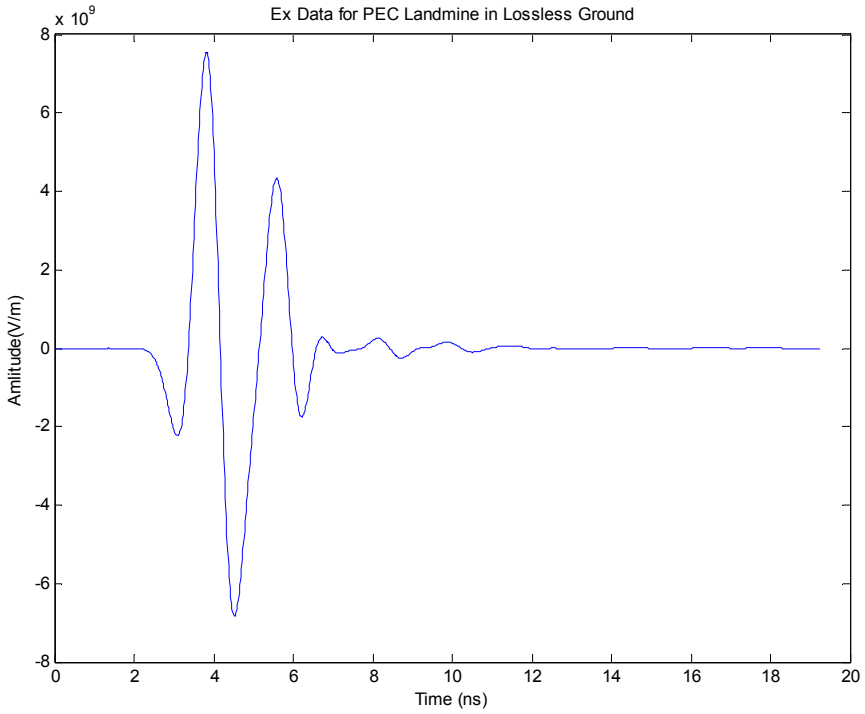

Figure 8.12: PEC Landmine Buried in Lossless Medium

space poles are given in Table 8.5.

The onset of late-time was chosen as 7 ns. When the late-time signal was analyzed with the MPM, 4 poles fit the signal well. The result of the MPM analysis is shown in Figure 8.13. The free space poles are shown with '+'s, the perturbation formula (7.11) calculated poles with filled circles and the observed poles (observed in the signal shown in Figure 8.12) are shown with 'o's. The exact pole locations for poles with positive imaginary parts are given in Table 8.5.

Table 8.5 PEC Landmine in Lossless Medium Pole Locations

Description	Pole #1 (MHz)	Pole #2 (MHz)	Pole #3 (MHz)
Free Space	$-191.1 + j1115.7$	$-298.9 + j1783.9$	$-460.7 + j2902.4$
Perturbed	$-95.5 + j557.9$	$-149.4 + j892.0$	$-230.3 + j1451.2$
Observed	$-48.8 + j570.6$	$-63.3 + j1045.1$	N/A

Again, the perturbation formula calculated damping ratios do not match very well with the observed damping ratios. However, the least damped poles show a reasonable match in resonant frequencies (557.9 MHz to 570.6 MHz). These frequencies are close enough to allow for at least approximate identification of the object. The difference in these poles here is again attributed to the switch from homogenous to layered medium.

The more highly damped set of poles (#2) do not match well in either frequency or damping ratio. This is not entirely unexpected, because of the highly damped nature of the free space time-domain response. The particular location of the higher frequency (and more damped) poles varies significantly with changes in the selection of the onset of late-time while the location of the least damped poles is more stable with respect to the onset of late-time. Poles that change location significantly with small changes in the selection of late time are probably not part of the late-time response, rather they are probably part of the early-time response, which is not an identifying feature.

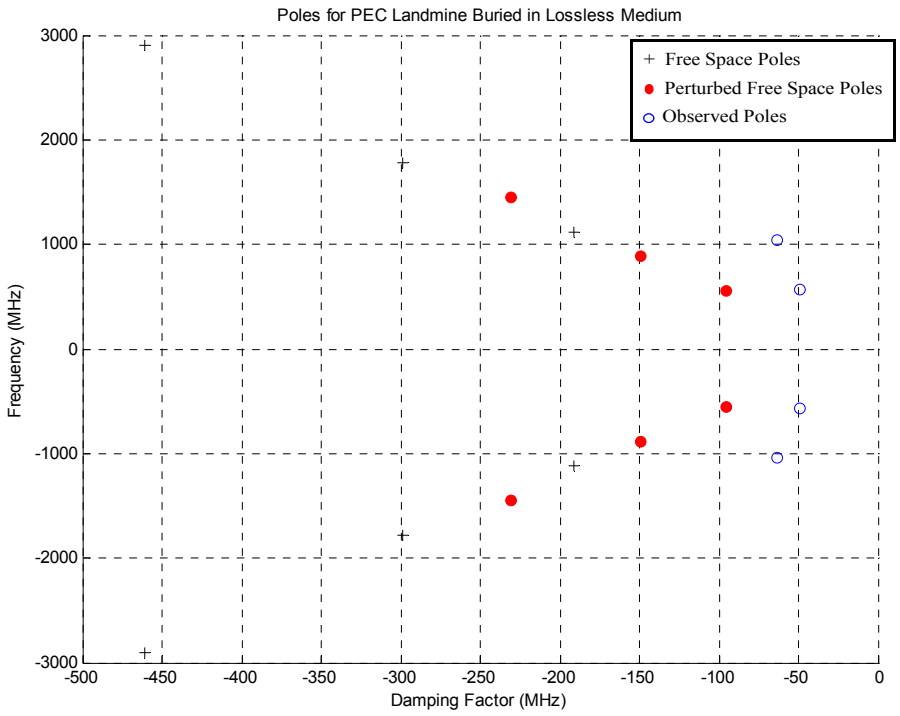

Figure 8.13: Poles for Buried Landmine in Lossy Medium

8.3.2 PEC Landmine in Lossy Medium

The FDTD code was re-run with the ground parameters changed to $\varepsilon_1 = 4\varepsilon_o$,

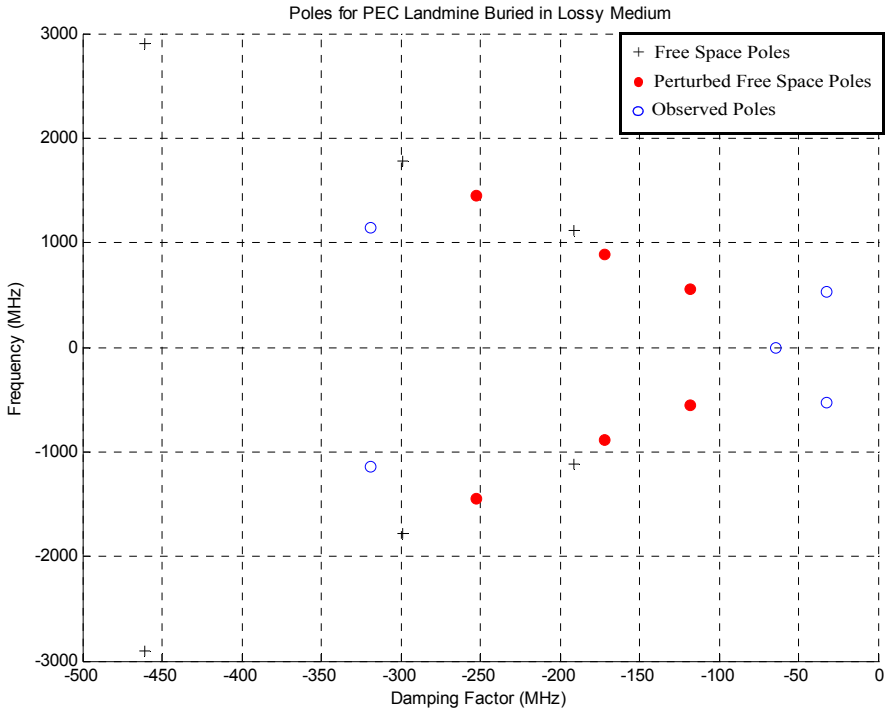

Figure 8.14: Poles for PEC Landmine in Lossy Medium

$\mu_1 = \mu_o$, and $\sigma_1 = 0.01$. Again, we considered the E_x field at point T1 in the FDTD grid. While not shown here, the time domain signal was generated and a late-time of 6.5 ns was selected by trial and error. The resulting poles are shown in Figure 8.14. The exact locations of positive frequency poles for the observed and perturbed poles are given in Table 8.6. Here, we note that there is a DC component in the late-time signal. We can see

Table 8.6 PEC Landmine in Lossy Medium Pole Locations

Description	Pole #1 (MHz)	Pole #2 (MHz)	Pole #3 (MHz)
Perturbed	$-118.1 + j557.4$	$-172.0 + j891.7$	$-252.8 + j1451.0$
Observed	$-32.7 + j534.0$	$-319.1 + j1147.5$	$-64.1 + j0$

this from the inclusion of a pole with zero frequency in Figure 8.14 and Table 8.6.

Similar to the lossless case, we see poor correlation in the damping ratios but the resonant frequency of the least damped poles shows promise as an identifier of the object. We can see, that even in lossy media, we can detect identifying features for PEC land-mine-like targets.

8.4 Dielectric Landmine-Like Targets

The dielectric perturbation formula of equation (7.16) provides a way to calculate the poles of dielectric targets buried in a homogenous medium. In [34], Worthy provides a region of effectiveness for the perturbation formula based on the material parameters of the surrounding medium, material parameters of the target and the depth of the target. He provides regions of 6% error and regions of 2% error.

To place our dielectric target within the 'effective' (6% error) region of the perturbation formula, we require a high dielectric contrast between the target and the surrounding medium. This means we must set the permittivity high inside the ground, which leads to a slower (by a factor of $\sqrt{1/\varepsilon_r}$) velocity of light in the ground. The lowest wavelength propagated in FDTD is limited by the grid spacing. Typically, this is taken to be around $\lambda_{min} = 5\Delta x$, where Δx is the grid spacing.

This creates a problem. We would like to increase the permittivity contrast between the ground and target by raising the ground permittivity significantly, but we also need to be able to detect the resonant frequencies of the object, which means reducing the FDTD grid spacing. If we were to use a small, realistic (anti-personnel landmine sized) dielectric object and still wanted to detect the resonant frequencies the grid spacing in our FDTD space would have to be made prohibitively small, creating extremely long processing times (measured on the order of days). To avoid these problems we have chosen a large dielectric target (more on the order of an ant-tank mine) for our simulations.

For dielectric targets, we note that there are now two known sources of error. One is the error caused from the use of a perturbation formula for homogenous media on targets embedded in a half-space, and the other is the error that is intrinsic to the use of the perturbation formula itself (the error associated with the assumption that the internal resonances

are based on the target being surrounded by PEC). This is contrasted with the PEC perturbation formula (equation (7.10)), where the only error is caused from the switch to half-space. Thus, we can expect the results from the dielectric perturbation formula to be less accurate than for the PEC case.

8.4.1 Calculation of Internal Resonances and Perturbations

The internal resonances of a (non-magnetic) dielectric-filled cavity with edge lengths of a, b and c, surrounded by a PEC, are given by [3]:

$$s_{\alpha,0} = \frac{j}{\sqrt{\mu_o \varepsilon_t}} \left[\left(\frac{m\pi}{a}\right)^2 + \left(\frac{n\pi}{b}\right)^2 + \left(\frac{p\pi}{d}\right)^2 \right]^{\frac{1}{2}}. \tag{8.2}$$

where ε_t is the permittivity of the cavity and m, n and p are integers representing the different resonant modes. The most dominant mode (lowest frequency) occurs when the integer of the smallest dimension is 0 and the other two are unity [36]. Thus, for our dielectric target, the most dominant mode is given by

$$s_{\alpha,0} = \frac{j}{\sqrt{\mu_o \varepsilon_t}} \left[\left(\frac{\pi}{a}\right)^2 + \left(\frac{\pi}{b}\right)^2 \right]^{\frac{1}{2}}. \tag{8.3}$$

After applying the surface and volume integrals in (7.16) to the fields generated by this mode we can find the perturbation Δs_α to be [36]:

$$\Delta s_\alpha = \frac{-1}{\xi(s_{\alpha,0})\sqrt{\mu_o \varepsilon_2}} \left[\frac{2a^3 d + 2b^3 d + ab^3 + a^3 b}{abd(a^2 + b^2)} \right], \tag{8.4}$$

where $\xi(s_{\alpha,0})$ is given by equation (7.14). Utilizing these formulae, we are now ready to compare observed poles with these calculated dominant poles.

8.4.2 Dielectric Landmine in Lossless Ground

In order to generate data within the 6% error region of the perturbation formula, we have selected a 20 cm x 5 cm x 20 cm dielectric target with the parameters $\varepsilon_t = \varepsilon_o$, $\mu_t = \mu_o$ and $\sigma_t = 0$. Essentially, we are simulating a cavity within the ground. The FDTD coordinates of the mine are $20 < x < 39$ cm, $11 < y < 15$ cm and $10 < z < 29$ cm. To accommodate the larger target, the z component of the FDTD space has been extended to cover from $0 < z < 40$ cm. The rest of the FDTD grid, including the antenna and current

density source positions remain unchanged. The ground parameters for the lossless case are selected to be $\varepsilon_1 = 10\varepsilon_o$, $\mu_1 = \mu_o$ and $\sigma_1 = 0$.

The time-domain signal resulting from the standard FDTD subtraction procedure for the E_x signal component from point T1 is shown in Figure 8.15.

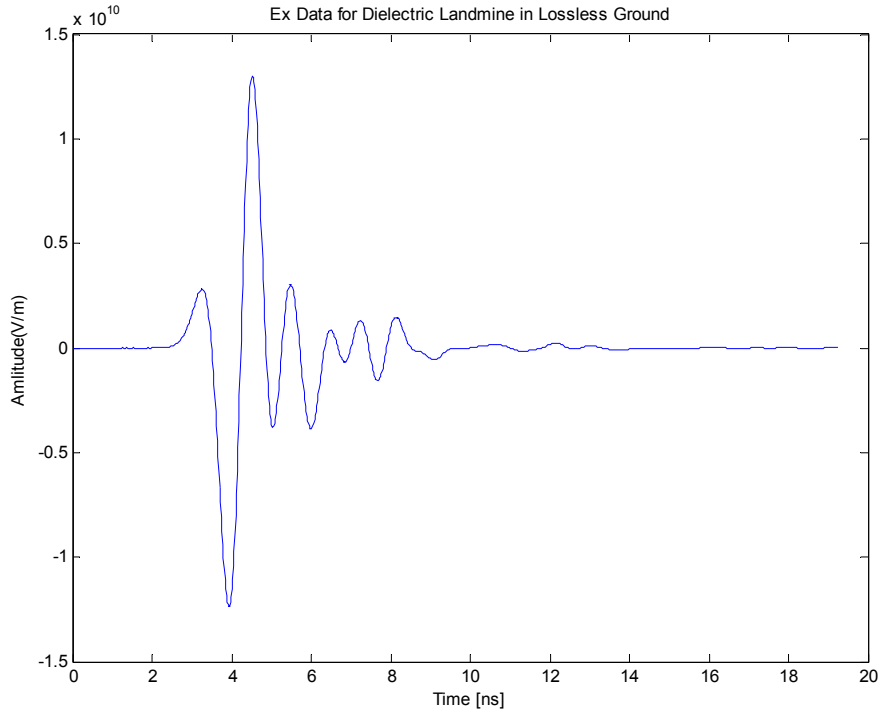

Figure 8.15: Time Domain Response of Dielectric Landmine In Lossless Medium

The onset of late-time was chosen to be 6 ns, and 4 poles were selected to model the signal. The results of applying the MPM are shown in Figure 8.16 and the exact locations of the perturbed internal resonances and observed poles are given in Table 8.7.

Table 8.7 Dielectric Landmine #1 in Lossless Medium Pole Locations

Description	Pole #1 (MHz)	Pole #2 (MHz)
Perturbed	$-452.7 + j1059.9$	N/A
Observed	$-99.1 + j1158.2$	$-84.5 + j699.4$

As can be seen the observed poles (shown with the ‘o’ mark) and the calculated poles (shown with filled circles) differ significantly in decay rate. The decay rate does not seem promising as an identifier for this problem.

In addition, we get an unexpected set of poles at 699.4 MHz. This frequency obviously does not correspond with the perturbation formula calculated poles, located at 1059.9 MHz. We assume that this lower frequency pole is caused by a resonance not directly related with the target and due to the lower frequency, we expect that this is a resonance that is related to the external medium. The FDTD code used utilizes boundary conditions (Mur second order) that are meant to absorb free-space radiation, and the placement of the ground material directly next to the absorbing boundary conditions will cause reflections in the FDTD simulation. We expect that if the boundary conditions were changed to be compatible with the ground medium that this pole would disappear.

There is a set of observed poles at a frequency of 1158.2 MHz. The perturbed internal resonance is at 1059.9 MHz and if we consider the two known sources of error: the half-space vs. homogenous space error, and the error associated with the use of the perturbation formula itself, this resonant frequency is within a a reasonable range and possibly qualifies as a suitable identifier.

However, there is a very large difference in the expected decay rates of these poles. It may be that the dielectric resonance that we would like to detect is so damped that

another resonance (caused by the external medium) is dominating the time-domain response.

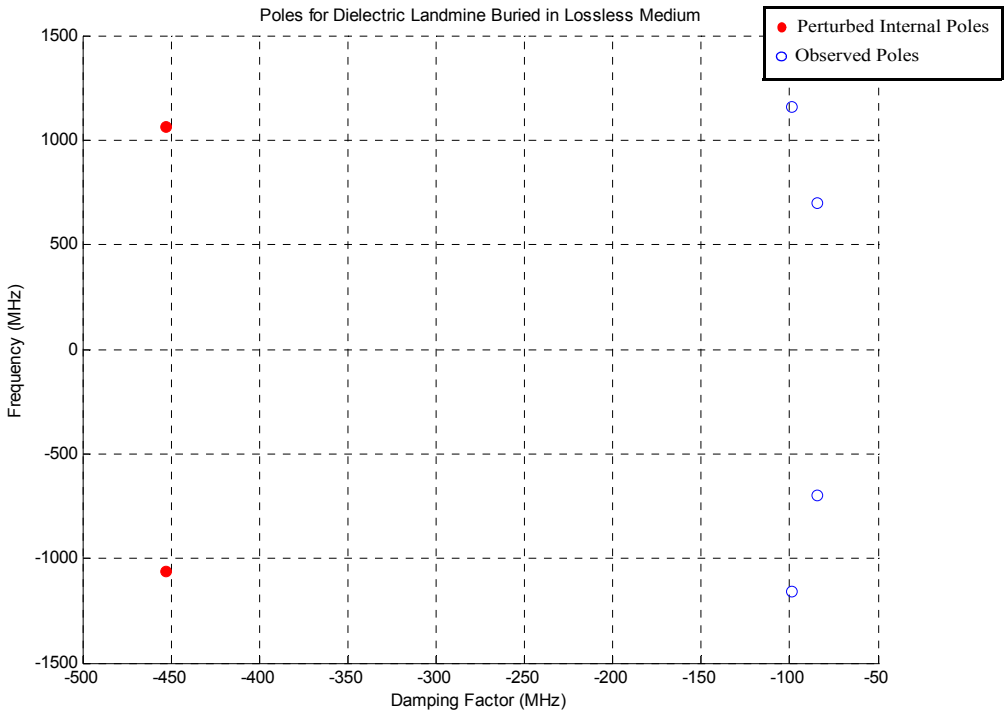

Figure 8.16: Poles for Dielectric Landmine in Lossless Medium

The dielectric mine in lossy media is not presented here, but offers similar results as the lossless case, with the observed poles having higher damping ratios.

8.4.3 Dielectric Landmine Number 2

To provide more data on dielectric targets, the FDTD code was run with a larger dielectric mine. Here, we defined a 40cm x 20cm x 5 cm object in the FDTD locations

$10 < x < 59$ cm, $11 < y < 15$ cm and $10 < z < 29$ cm. The new parameters were re-entered

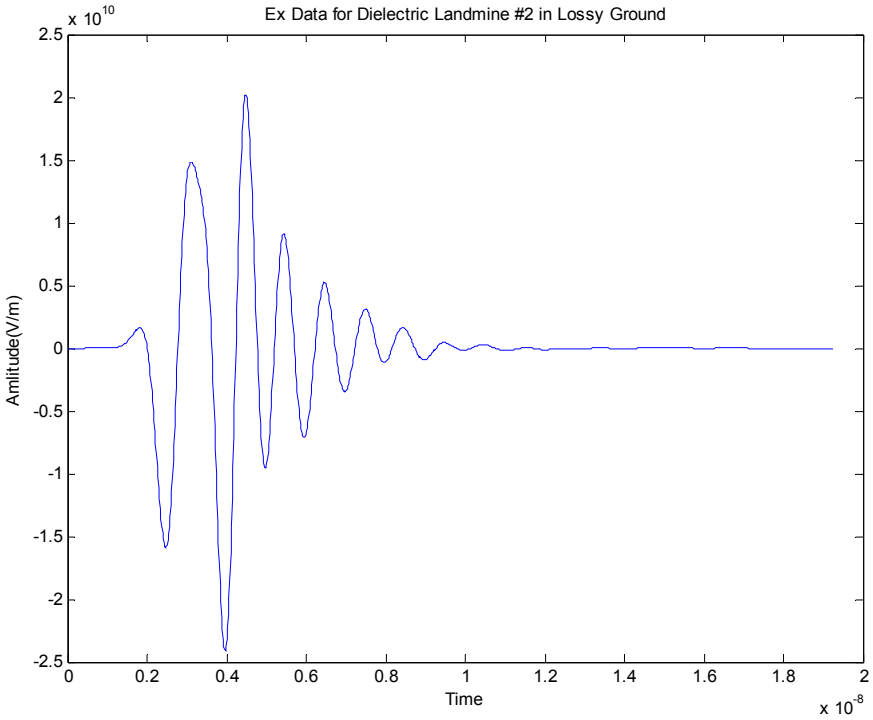

Figure 8.17: Time Domain Response of Dielectric Landmine #2 in Lossy Ground

and the time-domain results for the landmine buried in the lossy medium ($\varepsilon_r = 10$, $\sigma_r = 0.01$.) are shown in Figure 8.17. It is clear from this image that we are some type of resonance is occuring in the simulation. With a selected late-time of 6 ns and modelling the late-time signal with four poles, the results of the MPM are shown in Figure 8.18, with exact pole locations given in Table 8.8.

Table 8.8 Dielectric Landmine #2 in Lossy Medium Pole Locations

Description	Pole #1 (MHz)	Pole #2 (MHz)
Perturbed	$-437.5 + j833.3$	N/A
Observed	$-95.3 + j979.3$	$-18.2 + j135.4$

Once again, we see an unexpected set of poles, this time at a resonant frequency of 135.4 MHz. The set of observed poles (which have a significantly higher magnitude or residue, not shown here) are at a resonant frequency of 979.3 MHz, Again, with the

known sources of error taken into account, this seems a reasonable result. The fact that pole #1 has dropped in resonant frequency for dielectric landmine #2 (as compared to the smaller dielectric landmine #1) gives us reason to believe that pole #1 is a result of the dielectric target resonating.

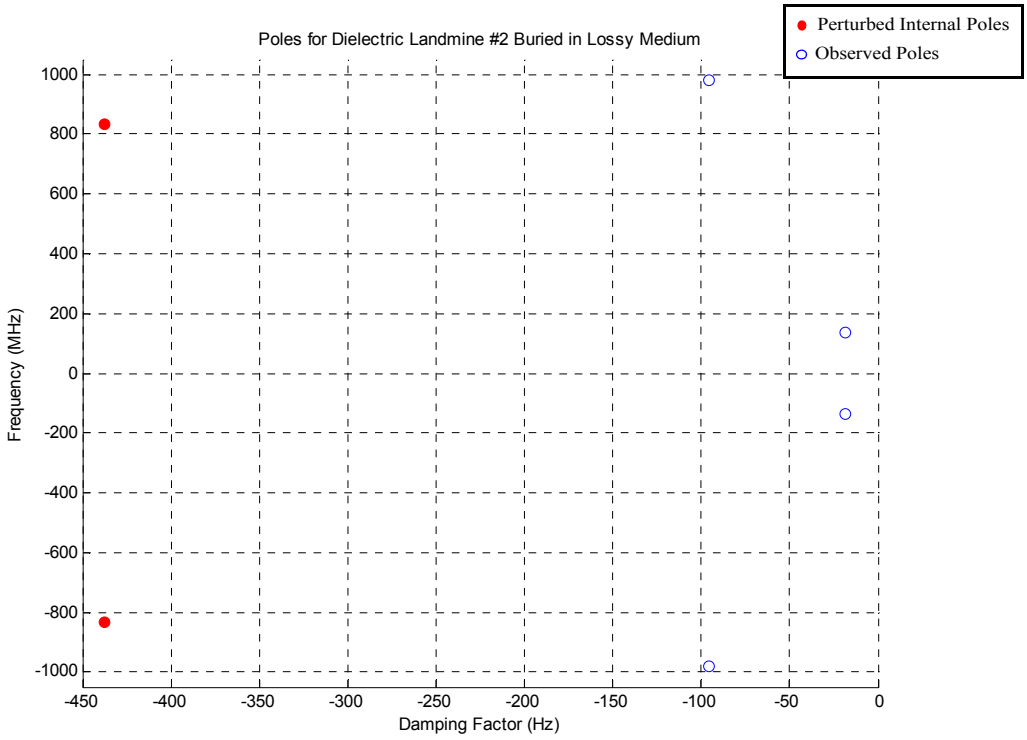

Figure 8.18: Poles for Dielectric Landmine #2 in Lossless Medium

The case for the lossless ground $\sigma_r = 0$ showed similar results, with the observed poles being slightly more damped.

8.5 Conclusions and Future Work

Utilizing perturbation formulae for buried PEC and dielectric targets we have applied the SEM method in an attempt to identify the targets. At this time, no solid conclusions can be made from the results, rather, the results point to areas where future work should be conducted.

It is clear from the results that the damping ratio, α_m, of the poles varies significantly from the predicted ratio for both PEC and dielectric perturbation formulae. It does

not show promise as an identifier for landmines detected using GPR (especially dielectric targets).

However, the resonant frequency (imaginary part of the complex pole) shows promise as an identification feature, taking into account known sources of error. For both PEC and dielectric targets the resonances show good correlation with resonances calculated with the perturbation formulae. For PEC targets the observed error can be attributed to the fact that the perturbation formulae are based on the target being surrounded by a homogenous medium, when in the GPR case they are located in a half-space. For dielectric targets, we have the homogenous vs. half-space error, as well as error introduced by the use of the dielectric perturbation formula. Unsurprisingly, the observed poles match the perturbation formula calculated poles better for the PEC perturbation formula than for the dielectric perturbation formula.

8.5.1 Future Work

There are several areas deserving further investigation that follow from these preliminary results. First, even when we have the almost ideal case of knowing all material parameters, the material parameters being frequency independent, the ground material being homogenous, and being able to subtract out the initial ground reflections there is still significant difference between the expected perturbed pole locations and the observed pole locations (especially for dielectric targets). We need to eliminate all sources of error that we can.

To do this, we suggest the implementation of the half-space perturbation formula of Hanson [33]. Although this will add significant complexity, it should eliminate a large portion of the error. For PEC targets, the use of the layered-medium perturbation formula should almost eliminate the error entirely for these FDTD simulations.

With the ultimate goal of implementing an experimental GPR system for the detection and identification of landmines, we also need to investigate time-domain signals that are not generated from the subtraction method used here (section 8.1.1). The FDTD subtraction method, while providing an excellent way to identify more fundamental sources of error (such as the half-space vs. homogenous problem) is not applicable to an experimental GPR system. Signals that match what is available from an experimental GPR sys-

tem need to be investigated. We can perhaps use a similar subtraction method, but subtract out the antenna free-space response, which would be easy to generate in an experimental GPR system.

Finally, we outline the need for a laboratory experimental time-domain GPR system to determine if detection of the natural resonances of buried dielectric and PEC objects is feasible from available equipment. The use of FDTD code provides an extremely large dynamic range, one that is not realizable for current time-domain radar receivers. It needs to be seen if this loss of dynamic range precludes the detection of these resonances.

Chapter 9
Conclusions

In part I we have shown how the image reconstruction techniques of Stripmap SAR, Kirchhoff Migration and Frequency Wavenumber migration are developed and implemented. The mathematical and physical models used for each algorithm were delineated and it was shown that Stripmap SAR and Frequency Wavenumber are almost identical from a computational point of view. The reasons for this were shown using a sum of plane waves interpretation of both techniques. The theoretical equivalence of KM and FK migration was shown. Stripmap SAR and FK migration are much more computationally efficient than KM, while offering similar image quality.

In part II we simulated a simplified GPR system with an FDTD code and showed that it is possible to detect the complex resonances of PEC and dielectric targets buried in both lossy and lossless ground (half-space). The location of these complex poles was predicted by the use of perturbation formula based on the free-space poles for PEC targets, and the internal resonances for dielectric targets. The perturbation formula shown were developed for homogenous medium surrounding the target, and this creates error in the prediction of the location of the poles. The decay rate (real part of the complex pole) is not predicted very well by the perturbation formula, but the resonant frequency (imaginary part of the complex pole) shows promise as an identifying feature.

Appendix A

Interpolation in Stripmap SAR and Frequency-Wavenumber Migration

The most time consuming step in both the Stripmap SAR and Frequency-Wavenumber focusing algorithms is the interpolation step. It occurs when we wish to map our data in the ω domain into the k_z domain, using

$$k_z = \sqrt{k^2 - k_y^2} \tag{a.1}$$

where $k = \omega / v_m$. The problem is best illustrated by the next series of diagrams.

We begin by considering discrete data collected in the y and ω domains. This is shown in Figure a.1. The data is plotted with respect to k. We have collected data only at the dis-

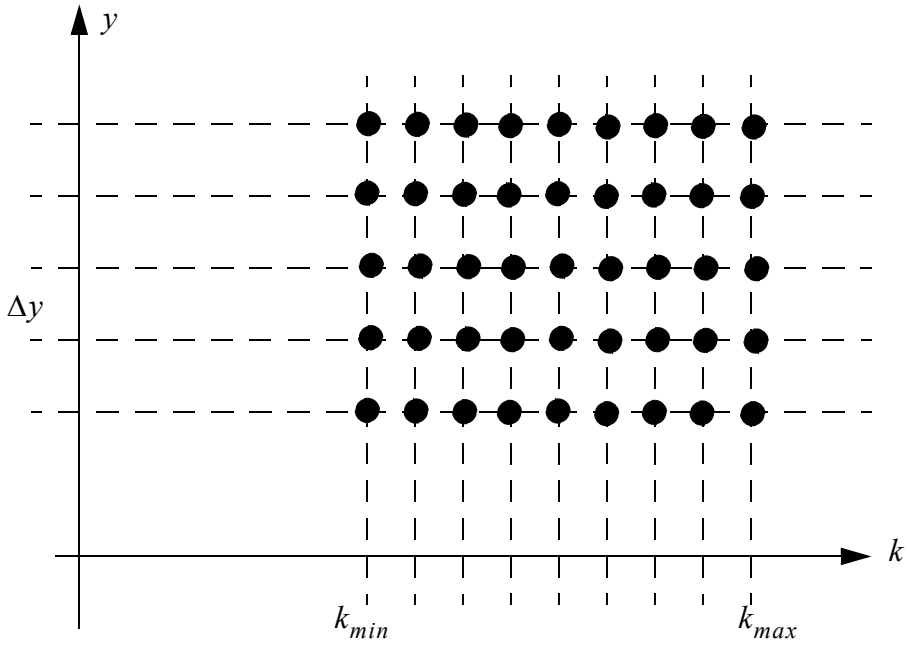

Figure a.1: Discrete Data in Stripmap SAR

crete points shown by the black dots. Outside the black dots, we don't have any data.

This first step in the Stripmap SAR algorithm is to take the FT in the y direction. This poses no problem, as we go from one evenly spaced grid to another. The next diagram is shown in Figure a.2.

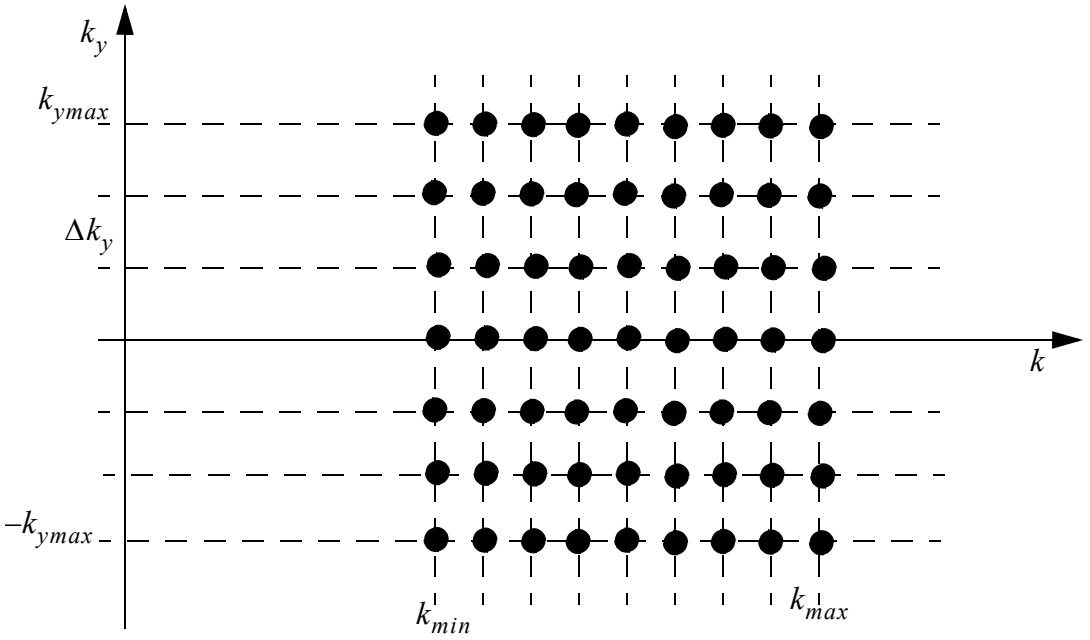

Figure a.2: Discrete Data in the Regular Frequency and Spatial Frequency Domain

The next step is the mapping step - which takes our data in the $S(k, k_y)$ (equivalently $S(\omega, k_y)$) domains and maps it to the $S(k_y, k_z)$ domains. This is completed through the equation

$$k_z = \sqrt{k^2 - k_y^2}. \tag{a.2}$$

In the k_z, k_y domain, this equation can be re-written as

$$k_z^2 + k_y^2 = k^2 \tag{a.3}$$

which describes circles of radius k in the k_z-k_y plane. Thus, *each line of constant k is mapped to a circle in the k_z-k_y plane.* The next mapping step is shown graphically in Fig-

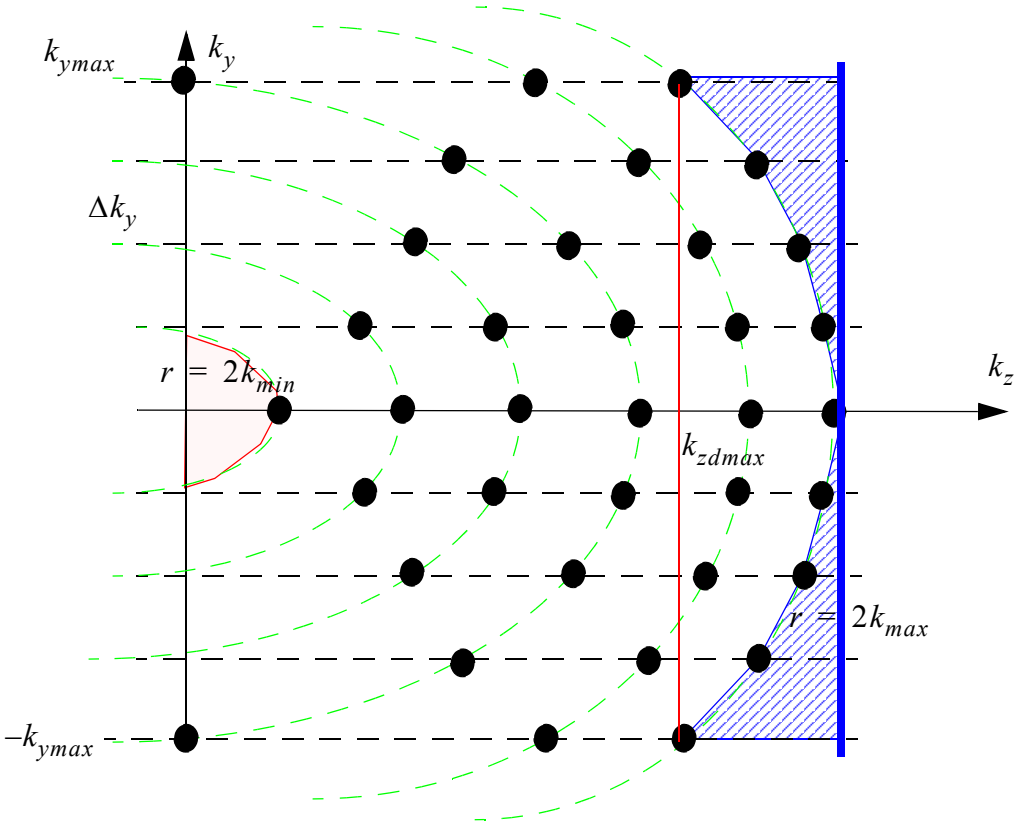

Figure a.3: Discrete Stripmap SAR data in Spatial Frequency Domains

ure a.3.

Complex values of k_z, i.e., when $k_y^2 > k^2$ are ignored.

Now, *for each value of k_y* there is an unevenly spaced set of data points in the k_z direction. In order to complete the discrete inverse fourier transform (see equation (3.20)) the data must be evenly spaced in k_z and k_y. To accomplish this, we must interpolate onto an evenly spaced grid in the k_z-k_y domain.

The starting point to accomplish the interpolation is to select an evenly spaced grid over which to interpolate onto. We denote the desired range of interpolation as being from k_{zdmin} to k_{zdmax}. In order to simplify the IDFT process, $k_{zdmin} = 0$. Whereas k_{zdmax} is

selected such that no extrapolation is required. Note that if we select k_{zdmax} equal to the maximum value of data we have on the k_z axis, as shown by the thick line in Figure a.3, we will have to extrapolate new data points in the top right and bottom right corners of the grid, shown as the hashed regions.

However, if we select

$$k_{zdmax} = \sqrt{4k_{max}^2 - k_{ymax}^2} \tag{a.4}$$

then no extrapolation is required. The location of k_{zdmax} is shown in Figure a.3 as a thin, solid vertical line. This selection of k_{zdmin} and k_{zdmax} is by no means the only selection possible.

Another possible area of concern is the area shown with the small dots. If k_{min} is too large, the area inside the smallest circle $r = 2k_{min}$ will be very underpopulated with data. Care must be taken to ensure that this area gives an accurate interpolation.

Now that we have selected the maximum and minimum of the grid we wish to interpolate onto, we need to choose the new discretize grid on which to interpolate. A simple choice for the number of points to discretize the k_z domain is the same number of points as we have collected for frequencies (i.e. if we have 501 different frequencies that we have collected data at, pick 501 sample points in the k_z domain). This is certainly not the only choice possible. Once this number has been chosen, the interpolation can be completed.

The interpolation can be done using any general method. Some specific methods are given in [6]. Another method, which was implemented here, is to use the built in function of MATLAB [17]- 'griddata'. The 'griddata' function allows for different interpolation techniques to be completed over any two non-regularly spaced grids. For example, we can complete linear, nearest neighbour and cubic interpolation schemes in 2-D. The linear and cubic interpolation are much better than nearest neighbour, but show little difference between each other.

Once the interpolation has been completed, the new range axis (z) can be computed from the formulae developed in equations (2.50) to (2.51).

Other techniques are available to complete this interpolation process [6], but are not considered here.

Appendix B

Source Code Examples

For part I of this thesis, the source code includes the code to generate synthetic data, Kirchhoff migration code, and a combined Stripmap SAR/FK migration code. All code is in the Matlab language.

For part II, source code is given here for the FDTD program outlined in [55] and for the implementation of the MPM in Matlab script. Only code for the PEC 20 cm wire is provided, as the other data generated comes from simple changes in these two programs.

b.1 Source Code for Part I

b.1.1 Matlab Source Code for Stripmap SAR, F-K Migration and B-scans

One program was used to generate B-scans, Stripmap SAR and F-K Migration images.

```
clear all
close all
clc

tic
%************************************************************************
% SAR Specifications
%************************************************************************

%************************************
% Database Information
%************************************

data_file = 'bistatic9_F_F_W1_M_s11.txt';
calibration_file = 'antenna1.txt';
data = load(data_file);
calibration = load(calibration_file);

% t = 1:4:501;
```

```
% data = data(t,:);
% calibration = calibration(t,:);
%
% [N TwoM]=size(data);
% data = [zeros(2*N,TwoM);data];
% calibration = [zeros(2*N,2);calibration];
[N TwoM]=size(data);
% data = data(N/2:end,:);
% calibration = calibration(N/2:end,:);
% N = N/2;


%%%%%%%%%%%%%%%%%%%%%%%%%%%%%%%%%%%%%%%%%%%%
% Zero Pad Factor (in the w domain)
%%%%%%%%%%%%%%%%%%%%%%%%%%%%%%%%%%%%%%%%%%%%
freqZeroPad = 8;
apertureZeroPad = 1;


%************************************
% Medium Information
%************************************

c=3e8;                                          %speed of light in the medium
Er = 3.5;                                       %Relative permitivity of the gound
encountered
v = c/sqrt(Er);                                 %relative velocity in the medium
c = v;

%************************************
% Frequency Domain Information
%************************************

fstart = 0.8;                                     %start frequency (in GHz)
fstop = 5;                                     %stop frequency (in GHz)
f = linspace(fstart,fstop,N)*1e9;               %frequency vector
df = f(2)-f(1);                                 %frequency step size

%************************************
% Spatial Information
%************************************

du = 0.01
M = TwoM/2;                                     %number of points in the synthetic
aperture
apertureLength = du*(M-1);                      %length of synthetic aperture
u = linspace(-apertureLength/2,apertureLength/2,M);           %Antenna position
vector


%************************************
% Range Informarion
%************************************

Fs = 2*f(end);
dt = 1/(Fs);
dx = v*dt/2;
```

```
%************************************
% Windowing Information
%************************************

xmin = 0.25;
xmax = .4;

%*************************************************************************
% Processing
%*************************************************************************

%************************************
% PreProcess Data To Create S = I+jQ
%************************************

p=1:2:(TwoM-1);
q=2:2:TwoM;
I=data(:,p);
Q=data(:,q);
S=I+j*Q;
[N M]=size(S);

%************************************
% Spectrum Completion:
%   As S = S(w,u) where w is band limited
%   between w1 and w2 (w1>0) we wish to
%   add the frequencies from DC to w1
%************************************

fLowFreq = fliplr((f(1)-df):-df:0);         %generate frequencies from 0 to w1
(actually from 0+eps (eps<df) to w1-df
lowZeros = length(fLowFreq);                %create zeros of this length
S = [zeros(lowZeros,M);S];                 %The positive frequency side of S is
now completed by concatenation
[N M] = size(S);                            %Store the new size of the matrix
f = [fLowFreq f];                           %The frequencies should also be con-
catenated


%************************************
% Load Cable Calibration Information
%************************************


calI=calibration(:,1);
calQ=calibration(:,2);
calS=calI+j*calQ;
calS = [zeros(lowZeros,1);calS];

%************************************
% Process Calibration -
%   Find the end of the cable by largest
%   reflection of open cct data.
%************************************

calSNegative = flipud(conj(calS(2:end-1,:)));
calS = [calS;calSNegative];
calRange = ifft(calS);
```

```
[Max Index] = max(abs(calRange));
Index = 0;
%************************************
% Process Calibration -
%   Shift so that the end of the cable
%   is the first element
%************************************

S_negative = flipud(conj(S(2:end-1,:)));
S = [S;S_negative];
rangeS = ifft(S);
rangeS = circshift(rangeS,-Index);

[FullN FullM] = size(S);

%************************************
% Define The Range Vector
%(We now have the length Required)
%************************************
x = (0:FullN-1)*dx;

%************************************
% Data Windowing -
%   Consider Range of xmin-xmax m past the
%   end of the cable
%************************************

minIndex = find(x>xmin-dx/2 & x<=xmin+dx/2);
maxIndex = find(x>xmax-dx/2 & x<=xmax+dx/2);

% Occasionally, minIndex and maxIndex may not be found.
% This is probably due to round off error in Matlab
if isempty(minIndex) | isempty(maxIndex)
    ERROR = 'Distance Index is Empty.  Try changing xmin and xmax slightly.'
    return
end


H = rectwin(maxIndex-minIndex);
H = [zeros(1,minIndex) H' zeros(1,(FullN-length(H)-minIndex))]';
H = repmat(H,1,FullM);
rangeS = rangeS.*H;


%************************************
% Post Windowing -
%   Convert back to frequency domain
%************************************

S = fft(rangeS);
S = S(1:N,:);
[N M] = size(S);                            %Store the new size of the matrix



%%%%%%%%%%%%%%%%%%%%%%%%%%%%%%%%%%%%%%%%%%%%%%%%%%%%%%%%%%%%%%%%%%%
% Zero Padding in the Frequency Domain
%%%%%%%%%%%%%%%%%%%%%%%%%%%%%%%%%%%%%%%%%%%%%%%%%%%%%%%%%%%%%%%%%%%
[N M] = size(S);
```

```
Nzeroed = freqZeroPad*N;
S_w_u = zeros(Nzeroed,M);
S_w_u(1:N,1:M) = S;

%This needed later for Bscan Imaging
BScanS = S_w_u;


%Now, Must Redefine Frequencies
if freqZeroPad ~= 1;
    fupper = linspace(f(end),f(end)*freqZeroPad,Nzeroed-N);
    f = [f fupper];
end

%**************************************************************************
% SAR Processing
%**************************************************************************




%*******
%STEP 1: Take the FFT in the u domain
%*******

S_w_ku = fftshift(fft(S_w_u,[],2),2);          %take the fft along the 2nd dimen-
sion (u)
k = 2*pi*f/v;                                %the wave number
dku = 2*pi/((M-1)*du);                         %the step size in the slow-time dop-
pler domain
ku = (-pi/du:dku:pi/du);
ky = ku;                             %the slow time doppler vector
[N M] = size(S_w_ku);

%*******
%STEP 2: Interpolation from unevenly spaced data
%   Here we use capitals to denote full matrices
%*******

KU = repmat(ku,N,1);                          %ku exists, constant vector for each
frequency
K = repmat(k',1,M);                           %k exists, constant vector for each
position
KY = KU;                                     %side effect of the physical problem,
ky = ku
KXmn = 4*K.^2-KU.^2;                         %side effect of the physical problem,
kx ~= k
KXmn = sqrt(KXmn);

for a = 1:N                                 %This (stupid) loop, converts imaginary
kx to negative kx
    for b = 1:M
        if ~isreal(KXmn(a,b)) == 1
            KXmn(a,b) = j*KXmn(a,b);
        end
    end
end
```

```
F_kxmn_ky = S_w_ku;                          %Now our function (F) is in the kxmn,
kymn domain (but kymn = ky)
kxmin = 0;                                  %We wish to reconstruct our information
over valid kx
kxmax = sqrt(4*k(end)^2-max(abs(ky))^2);
kx = linspace(kxmin,kxmax,N);                %construct the desired kx vector
(whereas kxmn is actual)
KX = repmat(kx',1,M);

%******************************
% Matlab Interpolation
%******************************

% Freal = griddata(KXmn,KY,real(F_kxmn_ky),KX,KY,'cubic');
% Fimag = griddata(KXmn,KY,imag(F_kxmn_ky),KX,KY,'cubic');
F_kx_ky_positive = griddata(KXmn,KY,F_kxmn_ky,KX,KY,'linear');
% F_kx_ky_positive= Freal +j*Fimag;
% F_kx_ky_positive = F_kxmn_ky;


%%%%%%%%%%%%%%%%%%%%%%%%%%%%%%%%%%%%%%%%%%%%%%%%%%%%%%%%%%%%%%%%%%%%%%%55
% Stolt Migration
%
%%%%%%%%%%%%%%%%%%%%%%%%%%%%%%%%%%%%%%%%%%%%%%%%%%%%%%%%%%%%%%%%%%%%%%%

W = c/2*(KX.^2+KY.^2).^0.5;
Jacobian = (c/2)^2*KX./W;
F_kx_ky_positive_Stolt = Jacobian.*F_kx_ky_positive;


%********
%SAR Imaging
%********
[N M] = size(F_kx_ky_positive);
F_kx_u_positive = ifft(ifftshift(F_kx_ky_positive,2),M,2);     %First take thje
ifft in the ky direction to get u
F_kx_u_negative = flipud(conj(F_kx_u_positive(2:end,:)));     %Create the full
spectrum over kx
F_kx_u = [F_kx_u_positive; F_kx_u_negative];
[N M] = size(F_kx_u);
F_x_u = ifft(F_kx_u);                                          %Take the ifft to
get x

[N M] = size(F_x_u);
dx = pi/kxmax;
x = (0:N-1)*dx;
u = linspace(-apertureLength/2,apertureLength/2,M*apertureZeroPad);


%********
% Display
%********


minIndex = find(x>xmin-dx/2 & x<=xmin+dx/2);
maxIndex = find(x>xmax-dx/2 & x<=xmax+dx/2);

% Occasionally, minIndex and maxIndex may not be found.
% This is probably due to round off error in Matlab
```

```
if isempty(minIndex) | isempty(maxIndex)
    ERROR = 'Secodary Distance Index is Empty.  Try changing xmin and xmax
slightly.'
    return
end

display_F_x_u = F_x_u(minIndex:maxIndex,:);

display_F_x_u = display_F_x_u/max(max(display_F_x_u));

figure
% subplot(3,1,1)
imagesc(u,x(minIndex:maxIndex),abs(abs(display_F_x_u)));
xlabel('Cross Range (meters)');
ylabel('Range (meters)');
title(' Stripmap SAR Focused Image of Dielectric and Metallic Targets');
colormap(flipud(gray));
colorbar
F_x_u_SAR = display_F_x_u;


%%%%%%%%%%%%%%%%%%%%%%%%%%%%%%%%%%%%%%%%%%%%%%%%%%%%%%%%%%%%%%%%%%%%%%%%%%%%%%%
% Stolt Migration
%%%%%%%%%%%%%%%%%%%%%%%%%%%%%%%%%%%%%%%%%%%%%%%%%%%%%%%%%%%%%%%%%%%%%%%%%%%%%%%

%********
%SAR Imaging
%********
[N M] = size(F_kx_ky_positive_Stolt);
F_kx_u_positive = ifft(ifftshift(F_kx_ky_positive_Stolt,2),M,2);     %First take
thje ifft in the ky direction to get u
F_kx_u_negative = flipud(conj(F_kx_u_positive(2:end,:)));     %Create the full
spectrum over kx
F_kx_u = [F_kx_u_positive; F_kx_u_negative];
[N M] = size(F_kx_u);
F_x_u = ifft(F_kx_u);                                                %Take the ifft to
get x

[N M] = size(F_x_u);
dx = pi/kxmax;
x = (0:N-1)*dx;
u = linspace(-apertureLength/2,apertureLength/2,M*apertureZeroPad);


%********
% Display
%********


minIndex = find(x>xmin-dx/2 & x<=xmin+dx/2);
maxIndex = find(x>xmax-dx/2 & x<=xmax+dx/2);

% Occasionally, minIndex and maxIndex may not be found.
% This is probably due to round off error in Matlab
if isempty(minIndex) | isempty(maxIndex)
    ERROR = 'Secodary Distance Index is Empty.  Try changing xmin and xmax
slightly.'
    return
end
```

```
display_F_x_u = F_x_u(minIndex:maxIndex,:);

display_F_x_u = display_F_x_u/max(max(display_F_x_u));

figure
% subplot(3,1,2)
imagesc(u,x(minIndex:maxIndex),abs(abs(display_F_x_u)));
xlabel('Cross Range (meters)');
ylabel('Range (meters)');
title('FK Focused Image of Dielectric and Metallic Targets');
colormap(flipud(gray));
colorbar

%load in the kirchhoff image to display
load Kirchhoff_Real
load Kirchoff_Real_Range
load Kirchhoff_Real_Cross_Range
% subplot(3,1,3);
figure
krichhoff_dielectric = krichhoff_dielectric/max(max(krichhoff_dielectric))
imagesc(u,X,krichhoff_dielectric);
title('KM Focused Image of Dielectric and Metallic Targets');
xlabel('Cross Range (meters)');
ylabel('Range (meters)');
xlabel('Cross Range (meters)');
colormap(flipud(gray))
colorbar



%%%%%%%%%%%%%%%%%%%%%%%%%%%%%%%%%%%%%%%%%%%%%%%%
% Plot the Difference Betweeen Stolt and SAR Processing
%%%%%%%%%%%%%%%%%%%%%%%%%%%%%%%%%%%%%%%%%%%%%%%%
figure
imagesc(u,x(minIndex:maxIndex),abs(display_F_x_u-F_x_u_SAR));
title('Difference Between Stolt and SAR');
xlabel('Cross Range (meters)');
ylabel('Range (meters)');
colormap(flipud(gray));
colorbar

%
% %************************************
% % Straight B-Scan imaging:
% %   In the case where we take the ifft directly,
% %   we must calculate the plotting parameters
% %   carefully
% %************************************
%
% Fs = f(end);                                %In this case we have only positive
spectrum
% dt = 1/(Fs);                                 %Fs = fmax
% dx = v*dt/2;
% x = (0:N-1)*dx;
% plotX = 0:dx:(length(display_F_x_u(:,1)-1));
%
% minIndex = find(x>xmin-dx/2 & x<=xmin+dx/2);
% maxIndex = find(x>xmax-dx/2 & x<=xmax+dx/2);
```

```
%
% figure                                        %plot the B-Scan image (This is
losing information.... it must be.)
% Temp = abs(real(ifft(BScanS)));
% display_Temp = Temp(minIndex:maxIndex,:);
% plotX = 0:dx:(length(display_Temp(:,1)-1))*dx;
% imagesc(u,plotX,display_Temp);
% xlabel('Cross Range (meters)');
% ylabel('Range (meters)');
% title('1 Sided FFT Image (Unfocused)');
%
%************************************
% B-Scan imaging using Spectrum reconstruction:
%   Here we reconstruct the double sided spectrum
%   in order to produce the appropriate image
%************************************

BScanPositive = BScanS;
BScanNegative = flipud(conj(BScanPositive(2:end-1,:)));
BScanFull = [BScanPositive;BScanNegative];
[N M] = size(BScanFull);

Fs = 2*f(end);
dt = 1/(Fs);
dx = v*dt/2;
x = (0:N-1)*dx;

minIndex = find(x>xmin-dx/2 & x<=xmin+dx/2);
maxIndex = find(x>xmax-dx/2 & x<=xmax+dx/2);

figure
TempFull = abs(real(ifft(BScanFull)));
display_TempFull = TempFull(minIndex:maxIndex,:);
plotX = 0:dx:(length(display_TempFull(:,1)-1))*dx;
display_TempFull = display_TempFull/max(max(display_TempFull));
imagesc(u,plotX,display_TempFull);
xlabel('Cross Range (meters)');
ylabel('Range (meters)');
title('1-D FFT B-Scan Image  (Unfocused)');
colormap(flipud(gray));
colorbar;
toc
```

b.1.2 Kirchhoff Migration Source Code

```
%Kirchhoff synthetic data program


clear all
close all
clc
tic

%%%%%%%%%%%%%%%%%%%%%%%%%%%%
% Load in the fake Data - Generated by Hong Su's Program
% Stored Originally as swu - I want S
%%%%%%%%%%%%%%%%%%%%%%%%%%%%
load FakeData
S = swu;
```

```
[N M] = size(swu);

%%%%%%%%%%%%%%%%%%%%%%%%%%%%%%%%%%%%%%
%Zero Padding Factor - Used in the Inverse FFT (and nowhere else)
%%%%%%%%%%%%%%%%%%%%%%%%%%%%%%%%%%%%%%5

freqZeroPad = 1;
apertureZeroPad = 1 ;


%%%%%%%%%%%%%%%%%%%%%%%%%%%%%%%%%%%%%%%%%%%%
% The desired viewing area (if we know where the synthetic targets are)
% note, must also choose to plot the windowed version of the final F_x_u
%%%%%%%%%%%%%%%%%%%%%%%%%%%%%%%%%%%%%%%%%%%%%%%
xmin = 0;
xmax = 0.82;

%**************************************
% Medium Information
%**************************************

c=3e8;                                       %speed of light in the medium
Er =2.2;                                      %Relative permitivity of the gound
encountered
v = c/sqrt(Er);                              %relative velocity in the medium
c = v;

%**************************************
% Frequency Domain Information
%**************************************

fstart = 1;                                  %start frequency (in GHz)
fstop = 12.4;                                   %stop frequency (in GHz)

f = linspace(fstart,fstop,N)*1e9;            %frequency vector
df = f(2)-f(1);                              %frequency step size

%**************************************
% Spatial Information
%**************************************

apertureLength = 2;                          %length of synthetic aperture
dBistatic = 0;                               %distance between Tx and Rx antennas
                                             %number of points in the synthetic
aperture
u = linspace(-apertureLength/2,apertureLength/2,M);%Antenna position vector
du = u(2)-u(1);                              %antenna position step size


%**************************************
% Spectrum Completion:
%   As S = S(w,u) where w is band limited
%   between w1 and w2 (w1>0) we wish to
%   add the frequencies from DC to w1
%**************************************

fLowFreq = fliplr((f(1)-df):-df:0);          %generate frequencies from 0 to w1
(actually from 0+eps (eps<df) to w1-df
lowZeros = length(fLowFreq);                 %create zeros of this length
```

```
S = [zeros(lowZeros,M);S];                  %The positive frequency side of S is
now completed by concatenation
[N M] = size(S);
f = [fLowFreq f];

%%%%%%%%%%%%%%%%%%%%%%%%%%%%%%%%%%%%%%%%%%%%%%%%%%%%%%%%%%%%%%%%%%%%%%%%%%%%%%%%
%%%%%
% Kirchhoff Migration Begins Here
%%%%%%%%%%%%%%%%%%%%%%%%%%%%%%%%%%%%%%%%%%%%%%%%%%%%%%%%%%%%%%%%%%%%%%%%%%%%%%%%
%%%%%

%first, take time derivative of the data
w = 2*pi*f;
omega = repmat(w,M,1)';

S = (j*omega).*S;

%create the full version of S (upper and Lower frequencies)
Sfull = [S; flipud(conj(S))];
Stime = ifft(Sfull);

xMax = c*1/df/2;
tMax = 1/df;
x = linspace(0,xMax,length(Sfull(:,1)));
dx = abs(x(2)-x(1));
% x = fliplr(x);
t= linspace(0,tMax,length(Sfull(:,1)));


lowDepth = find(x>xmin-dx/2 & x<=xmin+dx/2);
highDepth = find(x>xmax-dx/2 & x<=xmax+dx/2);
if xmax > max(x);
    [Eraseme highDepth] = max(x);
end


figure
imagesc(u,x(lowDepth:highDepth),abs(Stime(lowDepth:highDepth,:)));
colormap(flipud(gray));
colorbar;
getframe;

figure
contour(u,x(lowDepth:highDepth),abs(Stime(lowDepth:highDepth,:)));
colormap(flipud(gray));
getframe;

%diffraction summation
for yIndex = 1:length(u);
    yIndex
    for zIndex = lowDepth:highDepth;
        %the point to be migrated is now
        yPoint = u(yIndex);
        zPoint = x(zIndex);
        Sum = 0;
        for j = 1:length(u);
            measuredPoint = u(j);
            Rj = sqrt((yPoint-measuredPoint)^2+zPoint^2);
```

```
            %tHype = 2*Rj/c;
            if Rj<=max(x) & Rj ~= 0
               %now find the closest point on which to sum over
               costheta = zPoint/Rj;
                B_Xj_time = interp1(x,Stime(:,j),Rj,'nearest');
                B_Xj_time = B_Xj_time*costheta/Rj;
                Sum = Sum+B_Xj_time;
            end

        end
        Migrated_Image(zIndex,yIndex) = Sum;


    end
end


figure
imagesc(u,x(lowDepth:highDepth),abs((Migrated_Image(lowDepth:highDepth,:))));
colormap(flipud(gray));
toc
Migrated_Image = Migrated_Image(lowDepth:highDepth,:);
X = x(lowDepth:highDepth);
save KIRCHOFF_IMAGE Migrated_Image;
save KRICHOFF_RANGE X
save KIRCHOFF_CROSS_RANGE u;
```

b.2 Source Code for Part II

b.2.1 FDTD Source Code for PEC 20cm Wire

```
**************
* Input File For Joe's GPR
************************
.Problem Size
0 60 0 61 0 30
.Number
1000 1
.Space
1
0 60 0.01
1
0 61 0.01
1
0 30 0.01
.Test
20 30 15 1 T1ShortWireLoss
.Test
20 30 15 2 T1ShortWireLoss
.Test
20 30 15 3 T1ShortWireLoss
.Test
30 30 15 1 T2ShortWireLoss
.Test
30 30 15 2 T2ShortWireLoss
.Test
```

```
30 30 15 3 T2ShortWireLoss
.Test
25 7 15 1 bombShortWireLoss
.Test
25 7 15 2 bombShortWireLoss
.Test
25 7 15 3 bombShortWireLoss
.Directory
/home/ee/cgilmore/joe/final/PECShortWire/
.Boundary
aaaaaa
.Mur
2
.Object Ground
0 60 0 20 0 30 4 1 0.01
.Object A1
10 15 25 27 15 15 1 1 999
.Object A2
11 15 27 29 15 15 1 1 999
.Object A3
12 15 29 31 15 15 1 1 999
.Object A4
13 15 31 33 15 15 1 1 999
.Object A5
14 15 33 34 15 15 1 1 999
.Object A6
15 15 34 35 15 15 1 1 999
.Object A7
15 16 36 36 15 15 1 1 999
.Object A8
16 17 36 37 15 15 1 1 999
.Object A9
17 19 36 38 15 15 1 1 999
.Object A10
19 21 36 39 15 15 1 1 999
.Object A11
23 25 36 41 15 15 1 1 999
.Object A12
23 25 36 41 15 15 1 1 999
.Object Bomb
20 39 15 15 17 17 1 1 999
.Isource dipole
3 15 16 25 26 15 16 1 1 0 0
dgaussian
1.0 2e-9 5e-10
.End
```

b.2.2 Matlab Source Code for the Matrix Pencil Method

```
%Colin Gilmore
%Sept 2004
%Utilize the matrix pencil method to find the poles from the generated fdtd
%data.
clear all;
close all;
clc;
%first load the test data
[ExTotal,t] = readfdtddata('T1ShortWireLossEx.wave');
```

```
[ExIncident,t2] = readfdtddata('E:\Colin\FDTD Results\final\basic-
Ground\T1groundLossEx.wave');


%perform subtraction of the data
fulldata =ExTotal - ExIncident;

dt = t(2)-t(1);

figure
plot(t/1e-9,fulldata);
title('Ex Data for 20cm Wire in Lossy Ground');
xlabel('Time [ns]');
ylabel('Amlitude(V/m)');
pause

%%%%%%%%%%%%%%%%%%%%%%%%%%%%%%%%%%%%%%%%%%%%%%%%%%%%%%%%%%%%
% From the above graph, I have select the late time starting point.
% For now, I will read it in from the user
%%%%%%%%%%%%%%%%%%%%%%%%%%%%%%%%%%%%%%%%%%%%%%%%%%%%%%%%%%%%

lateTime = str2num(char(inputdlg('Beginning of Late Time','User
Input',1,{'0'})));
%always go to the end of the time domain response
stopTime = 1;

%create the late-time signal
    lateTimeData = fulldata(t >= lateTime & t<=stopTime)';
    lateTimeTime = t(t >= lateTime & t<=stopTime)';

    figure
    plot(lateTimeTime,lateTimeData)
    title('Late Time Data Selected to Perform the Matrix Pencil On');
    xlabel('Time');
    ylabel('Magnitude');
    pause

    %%%%%%%%%%%%%%%%%%%%%%%%%%%%%%%%%%%%%%%%%%%%%%%%%%%%%%%%%%%%
    % Here we begin the matrix pencil method. See Interaciton note 580 for a
    % cookbook method.
    % First, we must find the hankel matrix
    %%%%%%%%%%%%%%%%%%%%%%%%%%%%%%%%%%%%%%%%%%%%%%%%%%%%%%%%%%%%
    N = length(lateTimeData);

    %Select the pencil parameter
    L = ceil(N/3);
    if N-L<=L+1
        'L is Too High (Y matrix will be incorrectly sized for SVD)'
        break
    end
    %Create the data matrix Y
    Y=[];
    for aa = 1:N-L;
        ytemp = lateTimeData(aa:aa+L);
        Y = [Y; ytemp];
    end
    'data matrix found'
    beep
    %Next, find the singular value decomosition of the data matrix Y
```

```
    [U,S,V] = svd(Y,0);
    'svd finished'
    beep
    %now, we must plot the SVD of the data matrix in order to choose an number
    %of poles that we wish to calculate. The selection of the number of poles
    %is a critical step in the matrix pencil method
    % figure

    for a = 1:length(S(:,1));
        s(a) = S(a,a);
    end
    figure
    stem(20*log(s/max(s)));
    title('Magnitude of Singular Values');
    xlabel('Pole Order');
    ylabel('Magnitude (dB)');

    pause
    %let the user enter the number of poles to model the signal with
   M =str2num(char(inputdlg('Number of Poles to Select','User Input',1,{'0'})));

    Vnew = V(:,1:M);
    Snew = S(:,1:M);

    V1 = Vnew(1:end-1,:);
    V2 = Vnew(2:end,:);

    %now poles of the signals are given by the eigenvalues of ([v1]')(moore-pen-
rose inverse)*V2'.

    %now perform the moore-penrose psuedo inverse on V1Trans
    %start with a SVD of V1Trans
    V1TransPinv = pinv(V1);

    Zm = eig(pinv(V1)*V2);
    LogPoles = log(Zm);
    matrixPencilPoles = LogPoles/dt;
    matrixPencilPoles = real(matrixPencilPoles)+ (j/2/pi)*imag(matrixPencil-
Poles);

    %plot the poles
    figure
    scatter(real(matrixPencilPoles),imag(matrixPencilPoles)/1e6,'o');
    title('Poles for 20 cm Wire Buried in Lossy Medium');
    xlabel('Damping Factor (radHz)');
    ylabel('Frequency (MHz)')
    hold on

    %load in the pre-calculated free space poles
    load freeSpacePoles;
    %now perform Baum's transformation on the free space poles
    sig = 0.01;
    EpR = 4;
    Eps = EpR*8.854e-12;
    modifiedPoles = -(sig/2/Eps)+((sig/2/Eps)^2 + (1/EpR)*(freeSpace-
Poles.^2)).^0.5;
    %need to switch the phase of the poles after the sqrt in the above
    %formula
    modifiedPoles = -modifiedPoles;
```

```
%plot calculated poles and free space poles
scatter(real(modifiedPoles),imag(modifiedPoles)/1e6,'rx');
scatter(real(freeSpacePoles),imag(freeSpacePoles)/1e6,'g+');
```

References

[1] www.minesactioncanada.com

[2] Tenth Annual Conference on GPR, June 21-24, 2004, Delft, The Netherlands.

[3] Harrington, Roger, F. *Time-Harmonic Electromagnetic Fields,* IEEE Press, reprinted in 2001.

[4] Chew, W.C., *Waves and Fields in Inhomogenous Media*, IEEE Press, 1990

[5] Zhdanov, M.S., *Geophysical Inverse Theory and Regularization Problems,* Elseiver, 2002.

[6] Soumekh, *Synthetic Aperture Radar Processing,* John Wiley and Sons, United States, 2002

[7] Oristaglio, M., Blok,H. Wavefield Imaging and Inversion in Electromagnetics and Acoustics, Course Notes, Centre for Technical Geoscience course tg 101; ASEE course et 01-82; Electrical Engineering course et 01-38.

[8] Gilmore, C., Su. H, Jeffrey, I., Phelan, M. and LoVetri, J. 'Comparison of Seismic Migration and Stripmap SAR Imaging Methods for GPR for Landmine Detection'. Presented at EUROEM 2004, July 12-16th, 2004, Magdeburg, Germany. To be published in *Ultra-Wideband Short-Pulse Electromagnetics 7,* Editors: F. Sabath, E. Mokole, U. Schenk & D. Nitsch. Kluwer Academic/Plenum Publishers.(Publication pending review)

[9] Stratton, J.A. *Electromagnetic Theory*, McGraw-Hill Book Company, United States,1941.

[10] Phillips C.L., and Parr J.M., *Signals, Systems and Transforms,* Prentice-Hall, New Jersey, 1999.

[11] Proakis J.G., and Manolakis D.G., *Digital Signal Processing*, Prentice-Hall, New Jersey, 1996.

[12] Adomain, G. (1983) "Stochastic Systems." Mathematics in Science and Engineering Vol. 169, Academic Press.

[13] Morse and Feshbach, *Methods of Theoretical Physics Vol 1,* Section 7.3, McGraw-Hill, 1953).

[14] Jones, D.S. *The Theory of Electromagnetism*, Pergamon Press, 1964.

[15] Gunawardenda A., and Longstaff, D. 'Wave Equation Formulation of Synthetic Aperture Radar Algorithms in the Time-Space Domain', IEEE Trans. on Geoscience and Remote Sensing, Vol. 36, No. 6, November 1998.

[16] Papoulis, A. *The Fourier Integral and its Applications*, McGraw-Hill, United States, 1962, Reprinted 1987.

[17] Matlab 6.5 Release 13, The Mathworks Corporation, 2002.

[18] Scheers, B. *Ultra-Wideband Ground Penetrating Radar, with Application to the Detection of Anti Personnel Landmines*, Doctoral Thesis, Universite Catholique de Louvain Laboratoire D'Hyperfrequences Louvain-la-Neuve Belgium, 2001.

[19] Berkhout, A.J. 'Wave field extrapolation techniques in seismic migration, a tutorial', Geophysics, Vol. 46, No. 12, December 1981, pp 1638-1656.

[20] Claerbout J.F., *Imaging the Earths Interior*, Blackwell Scientific Publications, 1985.

[21] Yilmaz, O. *Seismic Data Processing*. Tulsa, USA: Society of Exploration Geophysicists, 1987, ch.4.

[22] Stolt, R.H., 'Migration by Fourier Transform', Geophysics, Vol. 43, Issue 1, pp. 23-48, Feb. 1978.

[23] Milisavljevic, N. and Yarovoy, A.G.; 'An effective algorithm for subsurface SAR imaging' Antennas and Propagation Society International Symposium, 2002. IEEE , Volume: 4 , 16-21 June 2002 Pages:314 - 317 vol.4

[24] Baum, Carl. 'On the Singularity Expansion Method for the Solution of Electromagnetic Interaction Problems' Interaction Note 88, 1971.

[25] Baum, C.E.; Rothwell, E.J.; Chen, K.-M.; Nyquist, D.P.;'The Singularity Expansion Method and its Application to Target Identification' Proceedings of the IEEE , Volume: 79 , Issue: 10 , Oct. 1991 Pages:1481 - 1492.

[26] Stiles, J.M. et. al.,'A Group Theoretic Analysis of Symmetric Target Scattering With Application to Landmine Detection', IEEE Transactions on Geoscience and REmote Sensing, Vol. 40, No. 8, 2002.

[27] Phelan, M; 'A Group Theoretical Symmetry Filter for Improved Subsurface Imaging', Masters Thesis, University of Manitoba, 2003.

[28] Gilmore, C; Peters, S; LoVetri, J; and McNeil, D. 'GPR Target Detection Using a Neural Network Classifier of Image Moments as Invariant Features', ANTEM 2004 Conference Proceedings, Ottawa, 2004.

[29] Baum, Carl. 'Discriminiation of Buried Targets via the Singularity Expansion' Inverse Problems, 13, 1997. pp 557-570.

[30] Baum, Carl. 'The SEM Representation of Scattering From Perfectly Conducting Targets in Simple Lossy Media'. Interaction Note 492, 1993.

[31] Baum, Carl. 'Concerning the Identififcation of Buried Dielectric Targets'. Interaction Note 504, 1994.

[32] Hanson, George W., and Baum, Carl. 'Perturbation Formula for the Internal Resonances of a Dielectric Object Embedded in a Low-Impedance Medium' . Interaction Note 520, 1996.

[33] Hanson, George W., 'Perturbation Formula for the Natural Frequencies of an Object in the Presence of a Layered Medium' Interaction Note 532, 1997.

[34] Worthy, Mark, and Baum, Carl. 'A Comparison of Exact Versus Perturbed Pole Locations of Dielectric Objects in Dielectric Medium', Interaction Note 529, 1997.

[35] Worthy, Mark, and Baum, Carl. ‘A Library of the Natural Frequency Responses for Cylindrical Shaped Buried Plastic Mines’. Interaction Note 530, 1997.

[36] Worthy, Mark, and Baum, Carl. ‘A Library of the Natural Frequency Responses for Rectangular Shaped Buried Plastic Mines’. Interaction Note 531, 1997.

[37] Chen, Chi-Chih and Peters, Leon, ; Buried Unexploded Ordnance Identification via Complex Natural Resonances’, IEEE Transactions on Antennas and Propagation, Vol. 45, No. 11, November 1997.

[38] Jain, Vijay K., Sarkar, Tapan K., and Weiner, Donald D.’Rational Modeling by Pencil-of-Functions Method’. IEEE Transactions on Acoustics, Speech and Signal Processing, Vol. ASSP-31, No. 3, June 1983.

[39] Hua, Yingbo and Sarkar, Tapan, K. ‘Generalized Pencil-of-Function Method for Extracting Poles of an EM System from Its Transient Response’, IEEE Transactions on Antennas and Propagation, Vol. 37, No. 2, February 1989.

[40] Hua, Yingbo and Sarkar, Tapan, K. ‘Matrix Pencil Method for Estimating Parameters of Exponenetially Damped/Undamped Sinusoids in Noise’ IEEE Transactions on Acoustics, Speech and Signal Processing, Vol. 38, No 5., May 1990.

[41] Hildebrand, F.B. *Introduction to Numerical Analysis*, Dover Publications, Inc. 1956.

[42] Jang, Seongman, Wonsuk, Choi and Sarkar, Tapan. “A Quantitative Comparison between the Matrix Pencil Method and the Sate Space Based Harmonic Retrieval Methods’, Interaction Note 579, February 2003.

[43] Selli, Giuseppe, Drewniak, James, and Pommerenke, David. ‘An Extrapolation Procedure to Shorten Time Domain Simulations’. Electromagnetic Compatibility, 2004. EMC 2004. 2004 InternationalSymposium on , Volume: 2 , 9-13 Aug. 2004

[44] Peters, Leon Jr.; Daniels, Jeffrey and Young, Jonathan. ‘Ground Penetrating Radar as a Subsurface Environmental Sensing Tool’. Proceedings of the IEEE Vol. 82, No 12. 1994.

[45] Carin, Lawrence, Sichina, Jeffrey and Harvey, James. ‘ Microwave Underground Propagation and Detection’, IEEE Transactions on Microwave Theory and Techniques, Vol. 50, No. 3, 2002.

[46] Geng, Norbert and Carin, Lawrence. ‘Wide-Band Electromagnetic Scattering from a Dielectric BOR Buried in a Layered Lossy Dispersive Medium’. IEEE Transactions on Antennas and Propagation, Vol. 47., No 4, 1999.

[47] Geng, Norbert; Jackson, David and Carin, Lawrence. ‘ On the Resonances of a Dielectric BOR Buried in a Dispersive Layered Medium’. IEEE Transactions on Antennas and Propagation. Vol 47, No.8, 1999.

[48] Geng, Norbert; Sullivan, Anders and Carin, Lawrence. ‘Multilevel Fast-Multipole Algorithm for Scattering from Conducting Targets Above or Embedded in a Lossy Half Space’. IEEE Transactions on Geoscience and Remote Sensing, Vol. 38, No 4. 2000.

[49] Sullivan, Anders; Damarla, Raju; Geng, Norbert; Dong, Yanting; and Carin, Lawrence. ‘Ultrawide-Band Synthetic Aperture Radar for Detection of Unexploded Ordnance: Modeling and Measurements’. IEEE Transactions on Antennas and Propagation, Vol. 48, NO. 9, 2000.

[50] Geng, Norbert; Sullivan, Anders and Carin, Lawrence. ‘Fast Multipole Method for Scattering from and Arbitrary PEC Target Above or Buried in a Lossy Half Space’. IEEE Transactions on Antennas and Propagation, Vol. 49, No 5. 2001.

[51] Wang, Yong; Longstaff, Dennis; Leat, Christopher; and Shuley, Nicholas. ‘Complex Natural Resonances of Conducting Planar Objects Buried in a Dielectric Half-Space’. IEEE Transactions on Geoscience and Remote Sensing, Vol. 39, No. 6, 2001.

[52] Vitebskiy, Stanislav and Carin, Lawrence. ‘Moment-Method Modeling of Short-Pulse Scattering from and the Resonances of a Wire Buried Inside a Lossy, Dispersive Half-Space’. IEEE Transactions on Antennas and Propagation, Vol. 43, No. 11, 1995.

[53] Vitebskiy, Stanislav and Carin, Lawrence. ‘Short-Pulse Plane-Wave Scattering from Buried Perfectly Conducting Bodies of Revolution’. IEEE Transactions on Antennas and Propagation, Vol. 44, No. 2, 1996.

[54] Vitebskiy, Stanislav and Carin, Lawrence. ‘Resonances of Perfectly Conducting Wires and Bodies of Revolution Buried in a Lossy Dispersive Half-Space’. IEEE Transactions on Antennas and Propagation, Vol. 44, No. 12, 1996.

[55] Mardare, Doru; Siushansian, Riaz and LoVetri, Joe. 3-D Dispersive EMFDTD Version 1.3, 1995. Internal Report, Dept. of Electrical Engineering University of Western Ontario.

[56] Bourgeois, J. and Smith, Glenn. ‘A Fully Three-Dimensional Simulation of a Ground-Penetrating Radar: FDTD Theory Compared with Experiment’. IEEE Transactions on Geoscience and Remote Sensing, Vol. 34, No. 1, 1996.

[57] Miller, E.K., and Sarkar, T.K., "An Introduction to the use of Model-Based Parameter Estimation in Electromagnetics," in Review of Radio Science 1996-1999, edited by W. R. Stone, Oxford University Press, pp. 139-174, Aug. 1999.

[58] Adve, R.S., Sarkar, T.K., Periera-Filho, O.M. and Rao, S.M., "Extrapolation of Time Domain Responses from Three-Dimensional Conducting Objects Utilizing the Matrix Pencil Technique," IEEE Trans. on Antennas & Propagation, Vol. 45, No. 1, pp. 147-156, Jan. 1997.